AMERICAN UNIVERSITY OF BEIRUT

LABEL-FREE ACOUSTIC CELL PHONE-ENABLED PLATFORM FOR RAPID POINT-OF-CARE DETECTION OF SARS-COV-2

by
KAREN ANTOINE ANTAR

A thesis
submitted in partial fulfillment of the requirements
for the degree of Master of Science
to the Biomedical Engineering Program
of the Maroun Semaan Faculty of Engineering and Architecture and
the Faculty of Medicine
at the American University of Beirut

Beirut, Lebanon
July 2023

AMERICAN UNIVERSITY OF BEIRUT

LABEL-FREE PIEZOELECTRIC PLATFORM FOR RAPID POINT-OF-CARE DETECTION OF SARS-COV-2

by

KAREN ANTOINE ANTAR

Approved by:

Dr. Massoud Khraiche, Assistant Professor Department of Biomedical Engineering, AUB	Advisor
Dr. Hassan Zaraket, Assistant Professor Department of Experimental Pathology, Immunology, and Microbiology, AUB	Co-Advisor
Dr. Pierre Karam, Associate Professor Department of Chemistry, AUB	Member of Committee
Dr. Jitdendran Muthuswamy, Associate Professor School of Biological and Health System's Engineering Arizona State University, ASU	Member of Committee
Dr. Jason Amatoury, Assistant Professor Department of Biomedical Engineering, AUB	Member of Committee

Date of thesis defense: July 4, 2023

AMERICAN UNIVERSITY OF BEIRUT

THESIS RELEASE FORM

Student Name: Antar (Last) Karen (First) Antoine (Middle)

I authorize the American University of Beirut, to: (a) reproduce hard or electronic copies of my thesis; (b) include such copies in the archives and digital repositories of the University; and (c) make freely available such copies to third parties for research or educational purposes:

- ☐ As of the date of submission
- ☑ One year from the date of submission of my thesis.
- ☐ Two years from the date of submission of my thesis.
- ☐ Three years from the date of submission of my thesis.

Karen Antar — Signature

August 11, 2023 — Date

ACKNOWLEDGEMENTS

I would like to extend my heartfelt appreciation to my family for their unwavering love, encouragement, and support throughout my academic journey.

I am also deeply grateful to all the individuals who played a significant role in the completion of this thesis. I would like to express my sincere gratitude to my advisor, Professor Massoud Khraiche, and my co-advisor, Professor Hassan Zaraket, for their invaluable guidance and support throughout the research process. I am also thankful to Professor Pierre Karam for his insightful input and assistance.

I would like to acknowledge the contributions of Habib Al Kalamouni and Joe Rahme, whose help and contributions have been instrumental in this work. Furthermore, I am grateful to Professor Michel Kazan for his guidance and assistance during the Raman spectroscopy experiments.

I would also like to extend my gratitude to all the members of my thesis committee for their valuable feedback and constructive comments, which have greatly enhanced the quality of this work.

Lastly, I would like to express my deep appreciation to the American University of Beirut for providing the platform and resources necessary for the completion of this thesis. I am truly grateful for the enriching experiences and opportunities I have had during my time on campus.

ABSTRACT

OF THE THESIS OF

Karen Antoine Antar for Master of Science
Major: Biomedical Engineering

Title: Label-Free Acoustic Cell Phone-Enabled Platform For Rapid Point-of-Care Detection of SARS-CoV-2

The COVID-19 pandemic persists, with spreading mutations causing severe illness. Point-of-care detection for COVID-19 remains crucial as it enables swift on-site testing and immediate results, facilitating timely diagnosis and decision-making in patient management. Enabling early identification of infected individuals, point-of-care COVID-19 detection supports effective containment measures, reduces transmission rates, and plays a vital role in outbreak prevention. In this work, we present a cell-enabled and handheld, cost-effective, label-free, acoustic platform and related sample preparation workflow for detecting SARS-CoV-2. The core technology utilizes Thickness shear mode (TSM) resonators with a sensitivity of 4.4 ng/(cm²·Hz) for biosensing applications in fluid. Our approach involves the development of stable poly(ethylene glycol) (PEG) on gold, a highly selective, chemistry specific to SARS-CoV-2. We conducted cross-reactivity testing, comparing the platform's response to Influenza-type A, a structurally similar virus to SARS-CoV-2, which showed minimal to no reactivity. The specificity and sensitivity of our assay platform were evaluated using dilutions of Bovine Serum Albumin (BSA) protein and lysed viral heat-inactivated SARS-CoV-2 virus samples at various sample concentrations. All in all, our research demonstrates a highly specific and sensitive point-of-care platform for rapid detection of the SARS-CoV-2 virus, targeting the viral nucleocapsid protein at clinically relevant concentrations. The platform has the potential to play a vital role in ongoing surveillance efforts and enables healthcare systems to respond swiftly to emerging cases, ensuring timely intervention and disease control.

TABLE OF CONTENTS

ILLUSTRATIONS

Figure

TABLES

Table

ABBREVIATIONS

Ab	Antibody
Ag	Antigen
Ag-RDT	Antigen-Rapid Detection Test
Ag-RAT	Antigen-Rapid Antigen Test
Au	Gold
BME	Beta-Mercaptoethanol
BSA	Bovine Serum Albumin
CI	Confidence Interval
COVID-19	Corona Virus-19
CT	Cycle Threshold
DIW	Deionized Water-Distilled Water
Edx	Energy Dispersive X-ray
ETA	Ethanolamine
HIV	Human Immunodeficiency Virus
mAb	Monoclonal Antibody
N	Nucleocapsid
NAAT	Nucleic Acid Amplification Technique
N mAb	Nucleocapsid monoclonal Antibody
NP	Nasopharyngeal
PBS	Phosphate Buffer Saline Solution
PFU	Plaque-Forming Units
RT-PCR	Reverse Transcription-Polymerase Chain Reaction
SEM	Scanning Electron Microscopy
Severe Acute Respiratory Syndrome Coronavirus 2	SARS-CoV-2
ssRNA	Single-stranded RNA
TSM	Thickness Shear Mode
$TCID_{50}$	Tissue Culture Infectious Dose 50
WHO	World Health Organization

CHAPTER 1

INTRODUCTION

The novel coronavirus disease, known as 2019-nCoV or COVID-19, emerged from the Severe Acute Respiratory Syndrome Coronavirus 2 (SARS-CoV-2) in late 2019 in Wuhan, a city located in the Hubei Province of China. Since its initial outbreak, COVID-19 has rapidly spread across the globe, leading to its declaration as a global pandemic on March 11, 2020 (WHO-2019-NCoV-Sci_Brief-POC_immunodiagnostics-2020.1-Eng.Pdf, n.d.). Notably, COVID-19 marks the third major spillover event of a coronavirus from animals to humans in the past two decades, following the Middle East Respiratory Syndrome Coronavirus (MERS-CoV) and the Severe Acute Respiratory Syndrome Coronavirus (SARS-CoV). All these viruses belong to the same family, known as Coronaviruses. However, COVID-19 has had a more profound impact compared to its predecessors due to its highly transmissible nature. It can be transmitted through various modes such as contact, fomite, bloodborne, droplet, and fecal-oral routes (WHO-2019-NCoV-Sci_Brief-Transmission_modes-2020.3-Eng.Pdf, n.d.).

The manifestation of COVID-19 in infected individuals can vary, with symptoms ranging from mild to severe. Some common symptoms include cough, shortness of breath, loss of taste or smell, fever, and headaches (Symptoms of COVID-19 | CDC, n.d.). Currently, the gold standard test for diagnosing SARS-CoV-2 infection is the reverse transcription-polymerase chain reaction (RT-PCR) test, which detects the presence of viral RNA. However, this technique is labor-intensive and time-consuming, leading to

delays in identifying infected individuals and implementing necessary measures to contain the pandemic.

The global impact of COVID-19 extends beyond public health, as countries have been compelled to implement complete shutdowns, resulting in a collapse of the worldwide economy. The recovery from this financial crisis is anticipated to require several years. To mitigate the risk of a resurgence in cases, it is crucial to enhance testing capacity and accessibility to enable rapid identification, isolation, and containment of COVID-19 cases and new clusters. This necessity has highlighted the urgent need to develop a highly sensitive, rapid, cost-effective, and accurate detection method for SARS-CoV-2, in addition to the existing RT-PCR technique.

Currently, there are two primary types of tests available for COVID-19. The first is serological testing, also known as antibody testing, which is used for monitoring public health and epidemiology. The second is viral testing, known as diagnostic testing, which can be performed using nucleic acid amplification techniques (NAAT) like RT-PCR, which detects the viral RNA. Alternatively, antigen testing can be employed to detect specific viral antigen proteins, such as the spike protein (S) or nucleocapsid (N) protein of SARS-CoV-2, or sometimes both (WHO-2019-NCoV-Antigen-Detection-2021.1-Eng.Pdf, n.d.).

However, the currently available rapid antigen screening techniques have not yet attained the desired level of sensitivity comparable to RT-PCR, rendering them less effective for COVID-19 diagnosis. RT-PCR remains the most reliable and widely used

tool for diagnosing SARS-CoV-2 infections. Antigen testing measures the viral antigen load in the testing specimen, while RT-PCR detects the viral RNA. It is important to note that detectable amounts of viral proteins can be identified within a window of approximately 15 minutes using antigen tests, whereas RT-PCR tests require several hours to complete (Labs, 2020).

In our work, we aim to present a low-cost, high-throughput, and highly sensitive point-of-care diagnostic platform for the rapid detection of COVID-19. Our approach utilizes a thickness shear mode (TSM) transducer as the base transducer, employing mass sensing for detection. Initially, we focused on developing a robust surface chemistry that enhances the capture of viral nucleocapsid antigen protein using immobilized SARS-CoV-2 antibodies on a polyethylene glycol (PEG)-modified surface of a 10 MHz gold quartz crystal sensor. PEG has been used in a majority of related applications: nanotechnology, immobilization, drug delivery, cell culture, material, and science. In addition, the carboxylic group of thiol-PEG-carboxymethyl (COOH-PEG-SH) is commonly used in surface chemistry coating due to its versatile and functional properties. It offers several advantages that make it suitable for various coating applications (Po-Chiao et al., 2006). This system is then characterized using various techniques such as digital holographic microscopy (DHM), Fluorescence microscopy, Raman spectroscopy, and scanning electron microscopy with energy-dispersive X-ray spectroscopy (SEM-EDX). Furthermore, we conducted a series of experiments using bovine serum albumin (BSA) protein dilutions in phosphate-buffered saline (PBS) on a bare quartz crystal microbalance (QCM) to determine the sensitivity of our assay. In addition, RT-PCR was conducted on our SARS-CoV-2 diluted aliquots to obtain their Cycle Threshold (CT) values. We also explored the limit of detection (LOD) of our

assay platform by performing PBS dilutions on a lysed heat-inactivated SARS-CoV-2 virus sample over SARS-CoV-2 nucleocapsid monoclonal antibody (N mAb). To validate the reliability and specificity of our COVID-19 sensor, we performed a cross-reactivity test using an inactivated lysed viral sample of Influenza type A.

Through our work, we aim to contribute to the development of an efficient and accessible diagnostic tool that can aid in the rapid detection and containment of COVID-19 cases, ultimately helping to combat the ongoing pandemic.

CHAPTER 2

LITERATURE REVIEW

2.1. SARS-CoV-2 Viral Structure and Genetic Composition

Understanding the viral structure and genetic composition of SARS-CoV-2 is crucial for developing effective diagnostic tests, vaccines, and antiviral treatments. Scientists and researchers worldwide have extensively studied the genome of SARS-CoV-2 to identify potential drug targets, track viral variants, and develop strategies to control the spread of the virus. (Q. Wang et al., 2020) (Habli et al., 2019)

SARS-CoV-2 is a spherical-shaped virus enveloping a positive single stranded RNA (ssRNA) genome of a size ~30 kilobases. Structurally, SARS-CoV-2 is an enveloped virus, meaning it is surrounded by a lipid membrane envelope derived from the host cell. It is distinguished from other *beta-coronavirus* family by its irregular crown-like spike glycoproteins projections on the viral surface. SARS-CoV-2 genome comprises 14 open reading frames (ORFs), which encode 27 proteins (Shoaib et al., 2021) (Figure 1):

- 4 structural proteins, which are the nucleocapsid protein (N), spike protein (S), membrane (M), and envelope protein (E),
- 15 nonstructural proteins and are crucial for the replication of the virus,
- The rest are accessory proteins.

Spike protein give the virus its distinctive crown-like appearance under electron microscopy, hence the name "coronavirus." Spike protein consists of 2 functional subunits, which are (Q. Wang et al., 2020) (Habli et al., 2019):

- S1, which recognizes and allow binding the receptor of the host cell, known as angiotensin-converting enzyme 2 (ACE2).

- S2 is involved in membrane fusion.

Membrane protein is the protein which determines the viral shape and is the most present within the virus. Nucleocapsid protein is the most frequent protein found during infection. Envelope protein is the smallest structural protein. It plays a role in pathogenesis and viral assembly (Shoaib et al., 2021)) (Habli et al., 2019).

One of the key features of SARS-CoV-2 is the presence of a unique polybasic cleavage site in its spike protein. This cleavage site is believed to enhance the virus's ability to infect host cells and contribute to its higher transmissibility compared to other coronaviruses. Additionally, SARS-CoV-2 has a relatively high mutation rate, which has led to the emergence of different variants or strains with distinct genetic signatures.

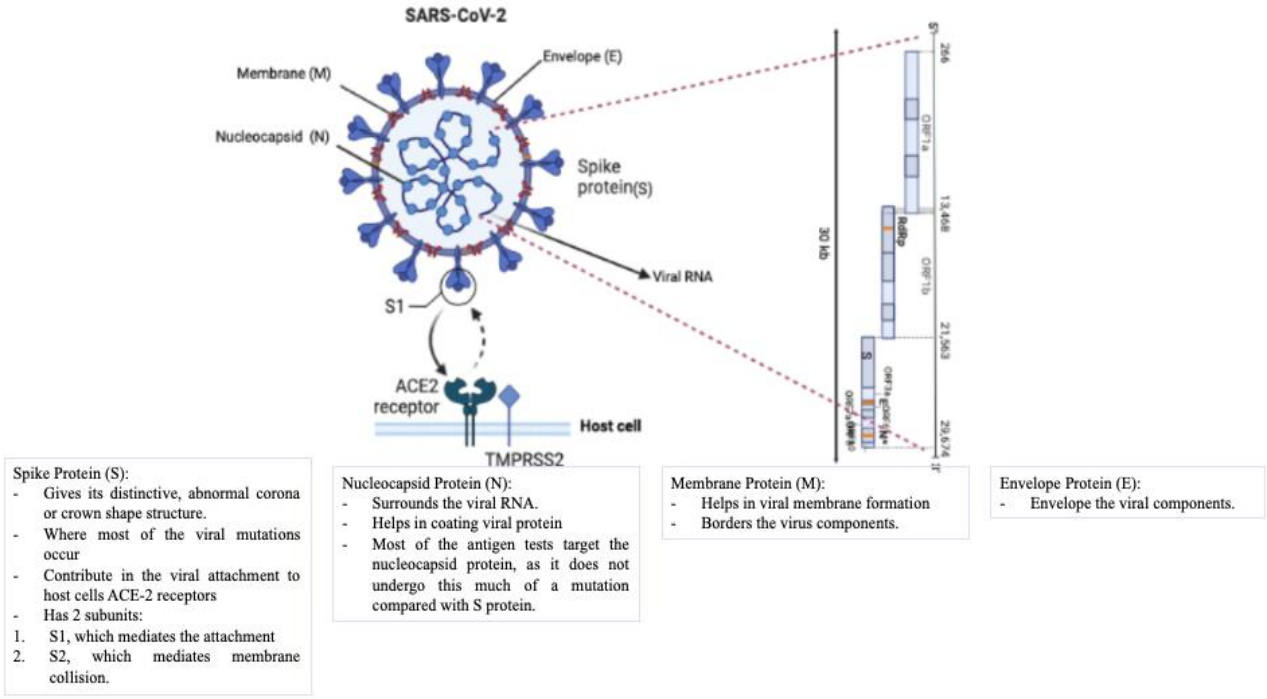

Figure 1 SARS-CoV-2 virus structure and genome organization (developed using https://biorender.com).

2.2. Reverse Transcription-Polymer Chain Reaction (RT-PCR) and COVID-19

Reverse Transcription-Polymerase Chain Reaction (RT-PCR) is a widely used molecular technique for detecting COVID-19. It has been the gold standard diagnostic method for identifying SARS-CoV-2, the virus that causes COVID-19. RT-PCR detects the presence of viral genetic material, specifically the viral RNA, in a patient's sample (Torretta et al., 2021).

The process of RT-PCR involves several key steps (*Polymerase-Chain-Reaction-Protocol.Pdf*, n.d.) (refer to Figure 2):

1. Sample Collection: A respiratory sample, such as a nasopharyngeal or oropharyngeal swab, is collected from the patient. Other samples, such as saliva or sputum, can also be used.

2. RNA Extraction: The viral RNA is extracted from the collected sample using specialized laboratory techniques. This step aims to isolate and purify the viral RNA from other components of the sample.

3. Reverse Transcription: The extracted RNA is then subjected to reverse transcription, where an enzyme called reverse transcriptase converts the viral RNA into complementary DNA (cDNA). This step is crucial as it enables amplification of the viral genetic material.

4. PCR Amplification: The cDNA obtained from the reverse transcription step serves as a template for the PCR amplification. PCR is a process that exponentially amplifies specific regions of the viral genetic material. It involves cycles of heating and cooling, which facilitate the binding of primers (short DNA sequences) specific to the SARS-CoV-2 genetic sequence. These primers flank the target region, allowing DNA polymerase to replicate the viral genetic material.

5. Fluorescent Detection: To monitor the amplification process, fluorescent probes or dyes are often used. These probes bind to the amplified viral DNA during PCR and emit fluorescence signals when the specific SARS-CoV-2 genetic sequence is present.

6. Data Analysis: The fluorescence signals generated during PCR amplification are measured and analyzed using specialized equipment. The presence of a significant increase in fluorescence within a certain number of cycles indicates a positive result, suggesting the presence of SARS-CoV-2 in the patient's sample.

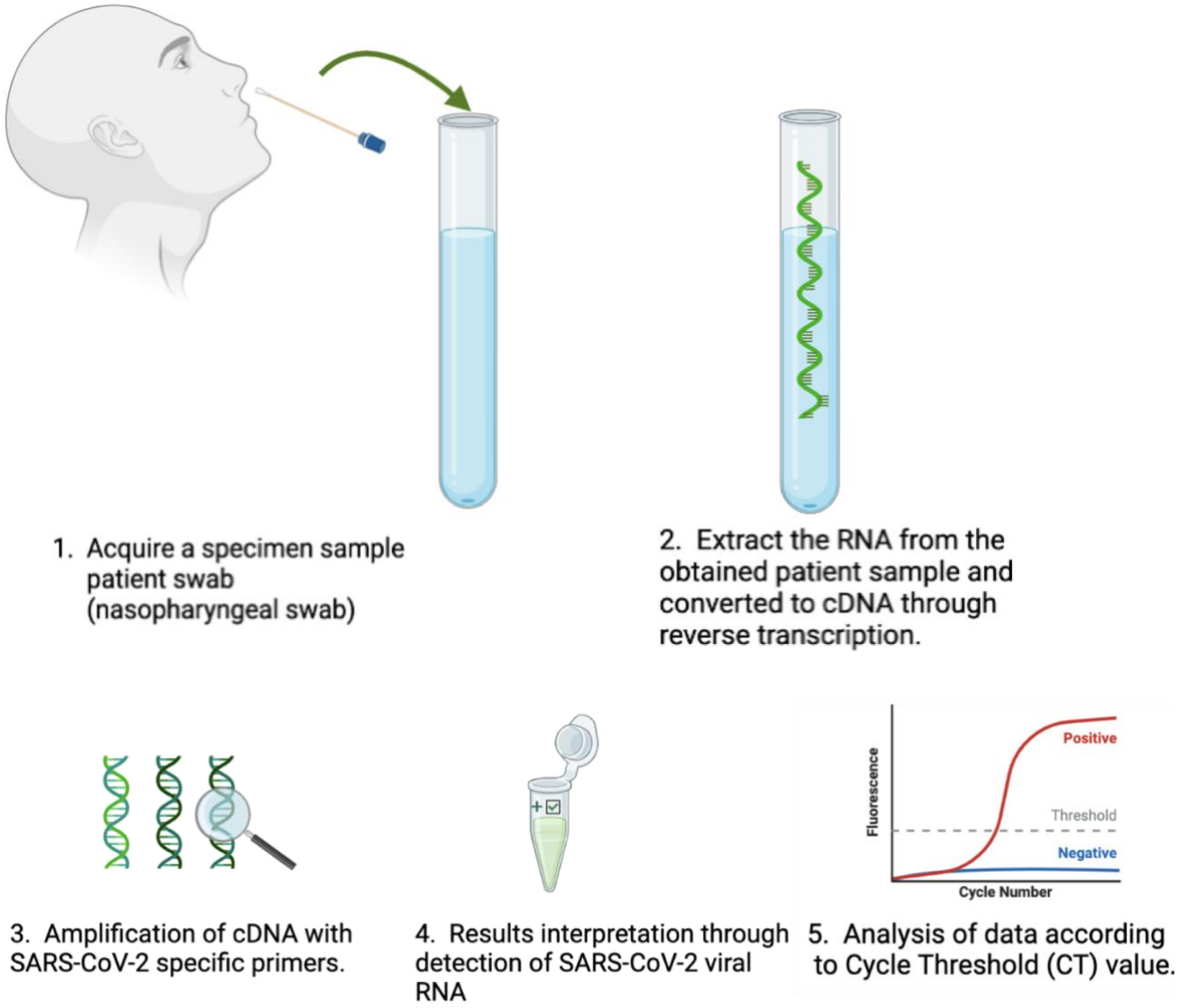

Figure 2 RT-PCR test components (developed using Biorender.com) (*COVID-19 Testing FAQs*, n.d.)

RT-PCR offers several advantages in COVID-19 detection (Shafie et al., 2023): Sensitivity: RT-PCR is highly sensitive and can detect even low levels of viral RNA in a sample. This allows for the detection of early-stage infections and the identification of asymptomatic carriers.

Specificity: The primers used in RT-PCR are designed to target specific regions of the SARS-CoV-2 genetic sequence. This ensures high specificity in identifying the presence of the virus.

Diagnostic Accuracy: RT-PCR has been validated and extensively used as the reference standard for COVID-19 diagnosis. It provides reliable results when performed correctly by trained laboratory personnel.

However, there are some limitations to consider (Manjate et al., 2023):

Laboratory Requirements: RT-PCR requires specialized laboratory equipment and trained personnel to perform the test accurately. This can limit its accessibility in resource-limited settings or areas without adequate laboratory infrastructure.

Turnaround Time: The entire RT-PCR process, including sample collection, RNA extraction, reverse transcription, PCR amplification, and data analysis, can take several hours to days. The turnaround time depends on laboratory capacity and the number of samples being processed.

False Negatives: False-negative results can occur due to various factors, including sampling errors, low viral loads in the sample, improper sample storage, or issues with the testing process. Multiple samples may be required over several days to increase the chances of detection.

Despite these limitations, RT-PCR remains the most reliable method for diagnosing active COVID-19 infections. It has played a crucial role in early detection, patient management, contact tracing, and epidemiological surveillance during the COVID-19 pandemic.

In addition to its role in diagnosing COVID-19, RT-PCR has proven to be a valuable tool in monitoring the progression of the disease, assessing viral load, and determining

the effectiveness of treatment interventions. It has also been instrumental in tracking the transmission dynamics of SARS-CoV-2 and identifying new variants of concern. (Peterson et al., 2022) (Verna et al., 2021)

One of the advantages of RT-PCR is its ability to provide quantitative data. By measuring the cycle threshold (CT) value, which represents the number of PCR cycles required to detect the virus, RT-PCR can estimate the viral load in a patient's sample. This information can help healthcare professionals gauge the severity of the infection and monitor the progression of the disease over time. (Al Bayat et al., 2021) (Hodoroaba, 2020)

Moreover, RT-PCR is not limited to diagnosing individual cases. It has played a crucial role in epidemiological surveillance and outbreak investigations. By analyzing the genetic material of SARS-CoV-2, researchers can track the transmission chains of the virus, identify clusters of cases, and understand the patterns of viral spread within communities. This information is vital for implementing targeted control measures and mitigating the impact of the pandemic.

As the field of COVID-19 research advances, RT-PCR has also been utilized for various applications beyond diagnostic testing. It has been used for viral genome sequencing, which helps in studying the genetic diversity of SARS-CoV-2 strains and identifying mutations that may affect its transmissibility or virulence. This genomic surveillance plays a critical role in detecting emerging variants and guiding vaccine development efforts.

In recent times, efforts have been made to optimize and streamline the RT-PCR process to increase testing capacity and reduce turnaround time. This includes the development of rapid RT-PCR assays and point-of-care testing platforms, which aim to deliver

results in a shorter period, enabling faster decision-making and control of viral transmission. (GOV UK, 2023; Panpradist et al., 2021)

Despite its wide usage and effectiveness, RT-PCR has some limitations. False-negative results can occur due to several factors, such as sampling errors, improper storage or transport of samples, or limitations in the sensitivity of the test. It is important to consider these limitations and ensure proper sampling techniques and quality control measures are in place to minimize false results (Benevides Lima et al., n.d.).

In conclusion, RT-PCR has emerged as a cornerstone of COVID-19 testing due to its high sensitivity, specificity, and ability to provide quantitative data. It has played a vital role in diagnosing cases, monitoring disease progression, tracking viral transmission, and guiding public health interventions. Continuous research and innovation in the field of RT-PCR will further enhance its capabilities and contribute to effective control and management of the ongoing COVID-19 pandemic.

2.2. Rapid Antigen Test in COVID-19 Diagnosis

As SARS-CoV-2 virus still prevails with an ongoing increase of COVID-19 cases in some countries, the urge for performing easy rapid mass testing for country citizens to decipher positive from negative COVID-19 cases has limited the capability of the gold standard RT-PCR to do the task as it takes one to two days for results to come out of the laboratory. Based on that, patients will therefore have to take proper measures, as recommended by the World Health Organization (WHO), such as isolating themselves if they are marked positive (*Labs*, 2020).

Given the aforementioned considerations, the U.S. Food and Drug Administration (FDA) has granted emergency use authorization (EUA) for antigen (Ag)

tests that can rapidly identify SARS-CoV-2 patients. Antigen tests are inexpensive immunoassays that can detect specific viral antigen proteins, which could be the viral nucleocapsid (N) and/or spike (S) protein(s). EUA has authorized antigen tests use in home-based, point-of-care, and laboratory-based, for people of any age, thus giving flexibility and easiness to users using Ag tests. In addition, the results of most Ag tests appear in approximately 15-30 minutes, faster than RT-PCR, which is known to be time-consuming, relatively expensive, and labor-intensive (Al-Alawi et al., 2021).

Unlike the PCR tests, which depend on the cycle threshold value to determine if a patient is tested positive or negative for COVID-19, rapid antigen test performance is estimated by calculating the sensitivity and specificity, and by taking into consideration the Positive Predictive Value, PPV and the Negative Predictive Value, NPP in a certain population of interest.

$$(1)\ Specificity = \frac{True\ Negative\ Cases}{(True\ Negative\ Cases + False\ Positive\ Cases)} \times 100\ (\%)$$

$$(2)\ Positive\ Predicitive\ Value = PPV = \frac{True\ Positive\ Cases}{(True\ Positive\ Cases + False\ Positive\ Cases)} \times 100\ (\%)$$

$$(3)\ Negative\ Predicitive\ Value = NPV = \frac{True\ Negative\ Cases}{(True\ Negative\ Cases + False\ Negative\ Cases)} \times 100\ (\%)$$

WHO has recommended in its interim guidance that for a rapid antigen diagnostic test to be used, it must meet the minimum performance requirements: having a sensitivity of greater or equal to 80% and a specificity of greater or equal to 97% in comparison with RT-PCR, the gold standard testing method. To date, there are commercially a total of 45 EUA-FDA certified antigen tests (Annex 1). It is worth mentioning that for an antigen test to be used in a laboratory or point-of-care setting to

report a patient test for COVID-19, it must be CLIA certified (*WHO-2019-NCoV-Antigen-Detection-2021.1-Eng.Pdf*, n.d.).

In addition, one of the current recommendations for achieving high coverage of testing in an antigen test is to ideally test symptomatic patients that show matching symptoms description provided by WHO within 7 days of illness when viral load is high, with a confirmatory result, if possible, from nucleic acid amplification test (NAAT), such as RT-PCR test. Recent studies have shown that Ag test had particularly stronger performance in terms of sensitivity with symptomatic adults than symptomatic children for less or equal a week of illness, while both have high specificity [1, 5]. In fact, Center for Disease Control and Prevention (CDC) found antigen testing to have a critical role in screen testing in high-risk congregate housing settings (nursing homes), which helps rapidly identify COVID-19 positive cases by repeat testing, even though having lower sensitivity when compared to the gold standard RT-PCR cycle threshold (CT) values (*Labs*, 2020).

There are two types of antigen tests, which are lateral flow assays, and immunoassay mechanisms. Both mechanisms use SARS-CoV-2 viral proteins to bind with specific human proteins only, and this binding can be read either by a change in light or color. Immunoassays are used to identify viral infection through patient specimen incubation with test proteins in a 96-well plate or similar assay. Lateral flow assays are used to identify viral infection through directional lateral flow of a patient specimen over proteins that are placed on a cassette or on a flat card. Antigen test results can be either read visually at a point-of care facility (POC) or at home (either over the counter or under supervision) or can be read by an instrument in a POC setting (*Antigen Tests | COVID-19 Testing Toolkit*, n.d.).

2.3. Challenges Facing Rapid COVID-19 Antigen Tests

Rapid COVID-19 antigen tests, also known as rapid antigen tests or rapid diagnostic tests (RDTs), have been widely used for quick detection of SARS-CoV-2 infections. While these tests offer several advantages such as faster results and easier implementation, they also face several challenges. Antigen testing may not be as effective as nucleic acid amplification test, like RT-PCR test, since when using NAAT technique, the RNA segment is amplified; however, this is not the case in antigen tests. The viral antigen proteins are only detectable if present in sufficient amount in the test sample, as the test runs only for 15 minutes, while RT-PCR test runs for hours (*WHO-2019-NCoV-Antigen-Detection-2021.1-Eng.Pdf*, n.d.). Thus, the lower sensitivity of antigen tests, as they cannot detect low levels of viral antigens, leading to false-negative results. This is particularly true during the early stages of infection when viral loads are lower (refer to Figure 3).

Antigen tests are often less effective in detecting asymptomatic cases compared to symptomatic cases. Asymptomatic individuals may have lower viral loads, making it more difficult for the antigen test to detect the infection. This limitation may hinder the effectiveness of rapid antigen tests in identifying and containing asymptomatic spread.

False negative might show up in Ag testing as viral load might not be detected, and in asymptomatic cases. Patients showing more than five to seven days post symptoms onset are more likely to have a low viral amount, thus the possibility of having false negative results with antigen rapid diagnostic testing specially (Brümmer et al., 2021) (*WHO-2019-NCoV-Antigen-Detection-2021.1-Eng.Pdf*, n.d.). In fact, Al-Alawi et al. stated that the low sensitivity of RATs drawback is overrated because the

missed cases are most probable to have low infection level and low viral loads (Al-Alawi et al., 2021). In addition, it may occur due to various reasons, including the quality of the test kit, the collection and handling of the specimen, and the timing of the test. False negatives can lead to infected individuals being erroneously classified as negative and potentially contribute to the further spread of the virus.

False positive might occur especially in low SARS-CoV-2 prevalence communities. Checking the test result before or after the time specified by the test manufacturer might lead to false positive or negative result. Thus, the importance to follow the test manufacturer guidance in order to not obtain a false result. It is important to report and notify health authorities about data recordings to monitor the data integrity, which are lacking for most test assays. In addition, it is best to have health care staff monitor RAT performance for better data acquisition (*Labs*, 2020). Cross-reactivity with other viral antigens or non-specific binding can also lead to false positives, requiring confirmatory testing.

Rapid antigen tests are designed to be user-friendly and accessible. However, proper training is still necessary to ensure accurate sample collection, handling, and interpretation of results. Lack of training and adherence to test protocols can affect the reliability and accuracy of the tests.

In fact, WHO recommends using RT-PCR test as a reference for a negative Ag test result for confirmation purpose. It is worth noting that Ag RDT results depend highly on SARS-CoV-2 prevalence in the studied community and also on how well the test performs (sensitivity, specificity). Improper sample handling collection may result in a false negative result (*Labs*, 2020) (*WHO-2019-NCoV-Antigen-Detection-2021.1-Eng.Pdf*, n.d.).

RT-PCR has a high sensitivity, and can locate more than two target regions of the virus (Ji et al., 2020) thus preventing false negative results, in case of major changes in one of the regions of targets of SARS-CoV-2, especially in variant of concern (VOC) cases (Ferré et al., 2022). In fact, according to FIND, the overall sensitivity of molecular testing assays (PCRs) is not expected to be affected when the virus is mutating into different VOCs, like Omicron, as these tests have multiple gene targets. The Omicron variant has deletions in the viral spike antigen protein gene, resulting in "S gene target failure". Viral mutations are less likely to target the N gene's C-terminus, which is not a hotspot for mutations (Boehm et al., 2021). Mutations in the virus may affect the Ag-RDT performance, according to WHO, there are reports of nucleocapsid gene (N) mutations that has resulted in false negative results, despite the high viral amounts detected by NAAT (*WHO-2019-NCoV-Antigen-Detection-2021.1-Eng.Pdf*, n.d.). Thus, the emergence of new variants of SARS-CoV-2, such as the Delta variant, has also raised concerns about the effectiveness of rapid antigen tests. Some variants may have mutations in the target antigen region, potentially reducing the sensitivity of the tests and increasing the risk of false-negative results.

Implementing rapid antigen testing at a population or community level poses challenges in terms of logistics, distribution, and coordination. Ensuring access to tests, organizing testing centers, and establishing a robust testing strategy require careful planning and resource allocation.

Rapid antigen tests need also to meet regulatory standards for accuracy and performance. However, ensuring consistent quality across different test manufacturers and complying with regulatory requirements can be challenging

Further studies must be conducted to estimate various possibilities to enhance RAT diagnosis, such as conducting clinical questionnaires to choose higher risk-contributors, the validation of negative test with RT-PCR or by consecutively repeating the RAT (Fernandez-Montero et al., 2021). Efforts are ongoing to address these challenges through technological advancements, improving test sensitivity, optimizing protocols, and conducting further research to evaluate the performance of rapid antigen tests, especially in different populations and settings. Regular evaluation and validation of these tests are crucial to ensure their accuracy and effectiveness in the ongoing fight against COVID-19.

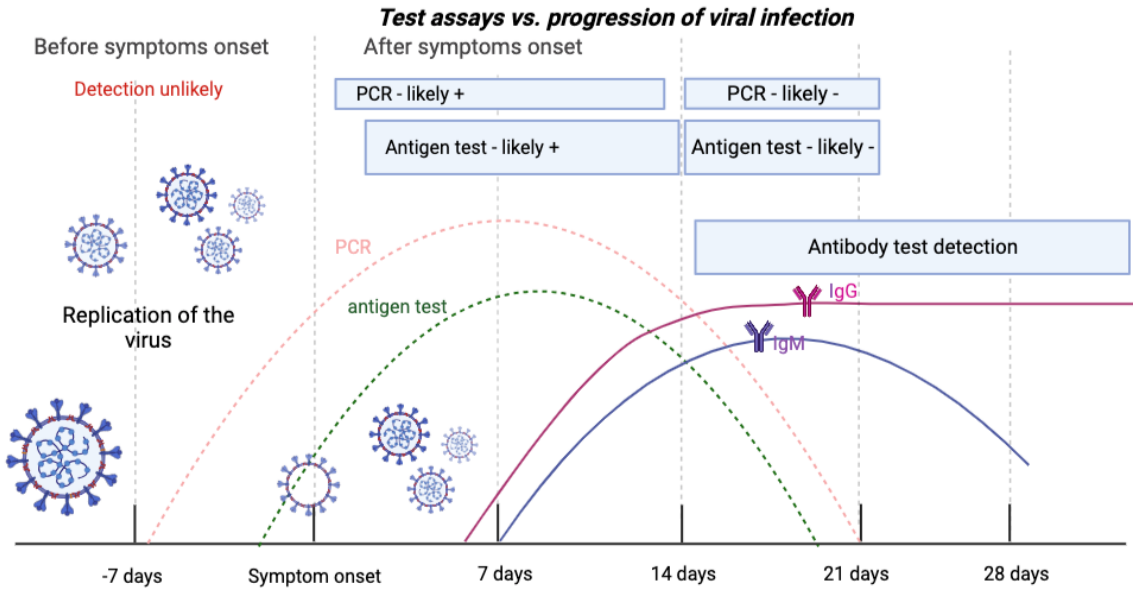

Figure 3 - The Operative Windows of Each of the COVID-19 Tests: Antigen Test, PCR, and Antibody Test (developed via Biorender.com) (Sethuraman et al., 2020).

2.4. Piezoelectric Biosensors

The ongoing COVID-19 pandemic has urged the need to incorporate rapid diagnostic testing platforms and this stirred up the sector of developing biosensors, as they are known to be easy to use, handy, cheap, and fast. A typical biosensor has three compartments: a bio-element, and a sensor element (transducer, amplifier, and signal processing). Biosensing platforms are evaluated according to their sensitivity and specificity. There exist four classes of biosensors based on its bio-element: antibody/antigen-based (labelled/non-labelled), enzymatic, cell-based, nucleic acid, or aptamer based. In addition, a biosensor is classified according to its type based on its transducer system, which can be either: piezoelectric, electrochemical, optical, magnetic, or micromechanical (Antiochia, 2021) (M. L. Khraiche et al., 2019).

In this work, we use a commercial 10 MHz AT-cut gold coated electrode quartz crystals from Novatech OpenQCM based on thickness shear mode (TSM) to establish our immunosensing performance. It has a nominal sensitivity of $4.42 \times 10^{-9} g\ Hz^{-1} cm^{-2}$at 10 MHz frequency operation range (refer to Table 1). Piezoelectric biosensors are based on the principle that a certain mass change, as a response of binding affinity event interaction, is sensed by a change in frequency of a piezoelectric quartz crystal resonator (Figure 4) (M. Khraiche & Muthuswamy, 2012). A piezoelectric immunosensor can be constructed by immobilizing a receptor, in our case SARS-CoV-2 nucleocapsid antibody onto the surface of a piezoelectric quartz crystal, and the binding of the nucleocapsid antigen can be demonstrated through a change in frequency due to binding of the ligand on the immobilized antibody (Figures 4 and 5).

An increase in mass can be read through our piezoelectric sensor by a decrease in the frequency oscillation (Antiochia, 2021).

Sauerbrey was first to develop a relation between the change in mass and the quartz crystal oscillation frequency in TSM, and he describes it as follows (Günter, 1959)

$$(4)\Delta f = -\frac{2f_0^2}{A\sqrt{\rho\mu}}\Delta m$$

Where $f_0$is the fundamental resonance frequency, A is the piezoelectric sensor active area. The QCM performance is based on mass sensitivity that describes the frequency shift f_0 due to viral antigen protein adsorption (M. L. Khraiche et al., 2003) (Günter, 1959).

The mechanical quality factor (Q) determines the resonance peak sharpness, and its formula is as follows (Narita et al., 2021):

$$(5)\ Q\ =\ \frac{f_0}{\Delta s}$$

Where Δs is the signal spread at a distance from the baseline equivalent to the magnitude divided by $\sqrt{2}$. The higher the Q value, the sharper the resonance peak, thus the more accurate it is in determining the resonance frequency (Narita et al., 2021) (M. Khraiche & Muthuswamy, 2012).

TECH SPECS	
One side contact	Yes
Quartz Frequency	10 MHZ
Nominal Sensitivity	4.42 x 10 -9 g Hz-1 cm-2

Frequency vs Temp stability	< +/- 5 ppm (0 to + 50 degC)
Frequency Tolerance	± 20 KHz @ 23°C
Capacitance	typ. 8 pF (C0)
Quartz Density	0.0026497 Kg/m3 @ 25°C
Stiffness	8.749 N/m2
Cut	AT
Cut Angle	35° 15'± 3'
Quartz Thickness	~ 160 um
Blank Diameter	14mm
Front electrode diameter	11.5 mm
Back electrode diameter	6.0 mm
Electrode material	Gold (Au)
Electrode Coating	Au -Ti substrate
Electrode Thickness	~ 200 nm Au (on ~10 nm Ti substrate)
Electrical Connection	Pogo-pins of HC-48/U
Surface appearance	Transparent
Cleaning	A new sensor might be contaminated. Pre-cleaning the surface will give more reproducible results

Table 1 Technical specifications of a 10 MHZ quartz sensors for liquid biosensing from Novatech OpenQCM used in our study (*10 MHZ QUARTZ SENSORS BOX FOR LIQUID BIOSENSING- 10 PIECES*, n.d.)

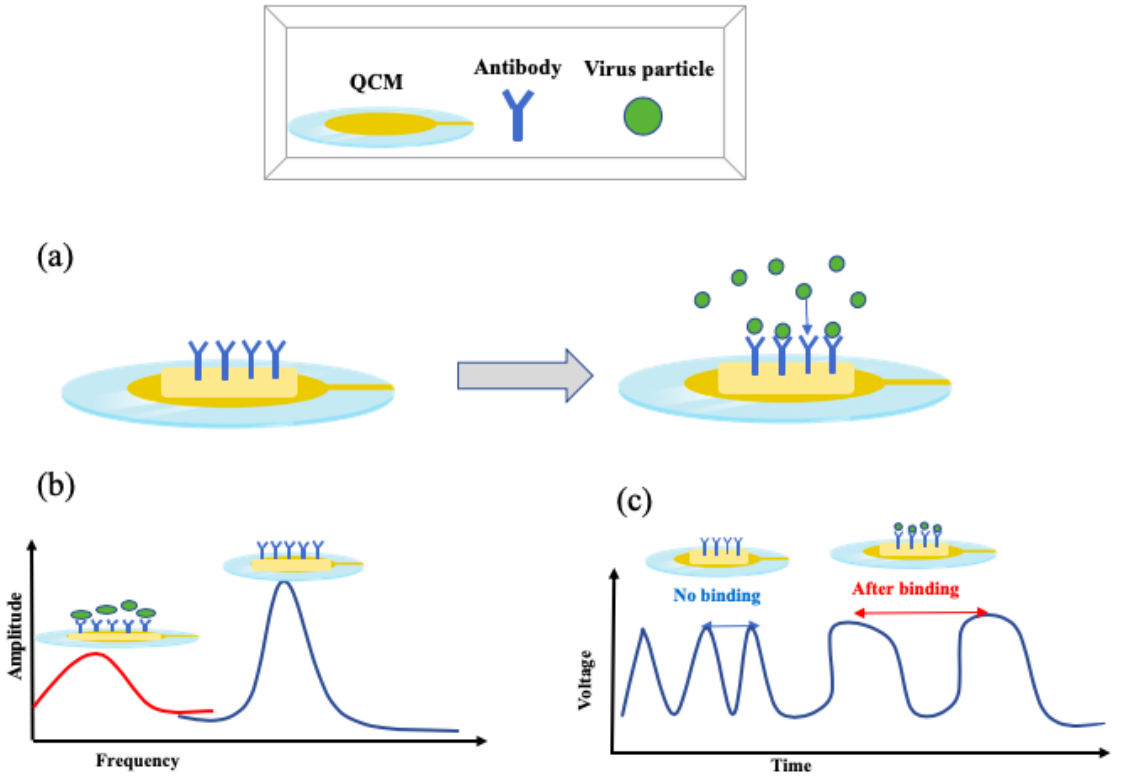

Figure 4 Viral detection using piezoelectric sensor: a) Concept of a piezoelectric QCM operation, b) voltage to time graph, c) amplitude to frequency graph.

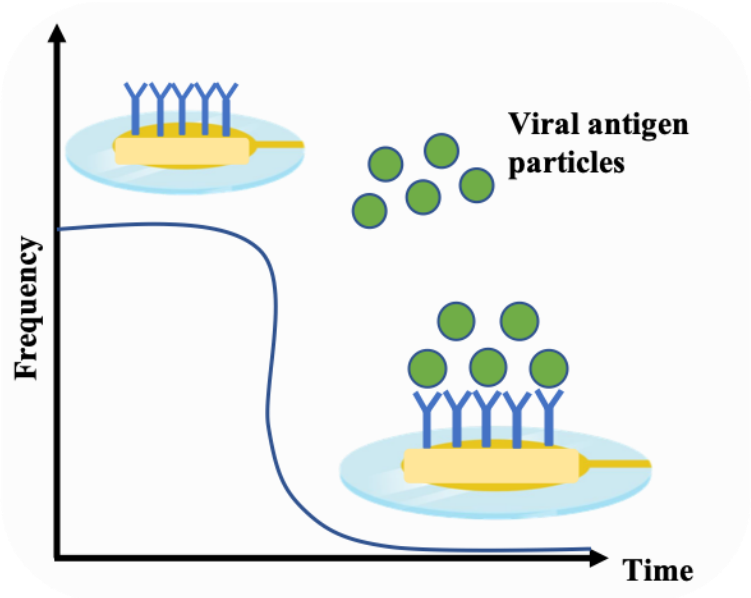

Figure 5 Frequency over time graph during a viral detection.

2.5. OpenQCM Q^{-1} with Dissipation Monitoring

Novatech S.r.l developed the OpenQCM Q1 device (Figure 6). It is based on the quartz crystal microbalance (QCM) concept, allowing for the simultaneous observation of frequency and dissipation changes over time. This one-of-a-kind capability enables the analysis of both viscoelastic characteristics and mass changes in thin films and coatings on the surface of a quartz crystal. The OpenQCM Q1 allows for more precise and extensive study of material interactions and surface phenomena. With a nominal frequency detection range of up to 72 MHz, this device measures with remarkable sensitivity and precision. (*OPENQCM Q-1 USER MANUAL Pdf Download | ManualsLib*, n.d.).

The OpenQCM Q1 can calibrate and measure quartz crystals at fundamental frequencies of 5 MHz and 10 MHz. It has two modes of operation: (*OPENQCM Q-1 WITH DISSIPATION MODULE*, n.d.):

- Open-O-Ring Window: permits mass variations on the quartz crystal surface to be measured in typical, open-air settings. It allows you to pipette different quantities of samples onto the crystal and measure the corresponding frequency changes. This mode is appropriate for experimentation in air or gas conditions.
- Fluidic Module Window (optional): allows the OpenQCM Wi1 to function in a closed fluidic system. This mode enables for the regulated flow of liquid samples across the surface of the quartz crystal. The fluidic module has an input and an outlet for sample admission and removal. It provides a sealed environment for studying molecular interactions and surface phenomena in liquid media.

These operation modes accommodate a wide range of materials and experimental needs, providing versatility in analyzing mass changes and molecular interactions on the quartz crystal surface.

As a result, Novatech OpenQCM Q1 can be used in various research areas, that includes surface chemistry, material science, biochemistry, and environmental monitoring.

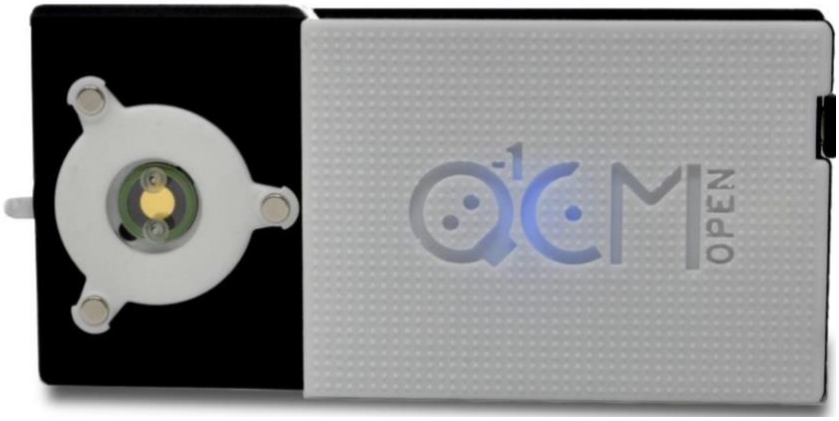

Figure 6 OpenQCM Q1 with Dissipation created by Novatech S.r.l.

2.6. OpenQCM Wi2

The OpenQCM Wi2, created by Novatech S.r.l. (Figure 7), is a sophisticated and adaptable machine based on the quartz crystal microbalance (QCM) concept. This portable, low-cost, open-source testing device allows for real-time monitoring and analysis of surface mass changes. OpenQCM Wi2 operates on the QCM concept, utilizing an electrical board with a crystal excitation circuit to create an output signal that is communicated to a computer through a USB connection. OpenQCM Wi2 can measure quartz crystals at fundamental frequencies of 6 MHz and 10 MHz. It precisely detects frequency changes and temperature variations over time, making it perfect for identifying and measuring biological molecules in point-of-care diagnostic equipment and portable applications. It has a nominal frequency detection range of up to 65 MHz.

One of the most important feature of OpenQCM Wi2 is its wireless connectivity, that enables scientists and researchers to remotely monitor and control experiments using computers or mobile devices. Compatible with a wide range of lysis buffers and chemicals used in surface chemistry and molecular interaction studies, the OpenQCM Wi2 provides a convenient and effective solution for surface analysis and studying molecular interactions.

The OpenQCM Wi2 is supported by the OpenQCM software platform, which offers a user-friendly interface for data visualization, analysis, and storage. Researchers can easily access and interpret their experimental data using this intuitive software.

Novatech OpenQCM Wi2 offers two modes of operation (*OpenQCM_Wi2-Userguide-v2.0.Pdf*, n.d.):

- Open-O-ring window, various volumes can be pipetted in and out under normal, open-air conditions. The maximum mass sensitivity in air medium is 10 pg/mm^2.
- PMMA Fluidic Module window, an inlet-outlet volume pumping system is employed. The maximum mass sensitivity in liquid medium is 5 pg/mm^2.

In conclusion, the OpenQCM Wi2 Novatech machine is a cutting-edge QCM instrument that brings together wireless connectivity, advanced functionality, and an easy-to-use software to offer a powerful tool for surface analysis and molecular interaction studies. Its versatility and precise measurement capabilities make it a vital tool for scientists working in many disciplines, including surface chemistry, biosensors, material science, and nanotechnology.

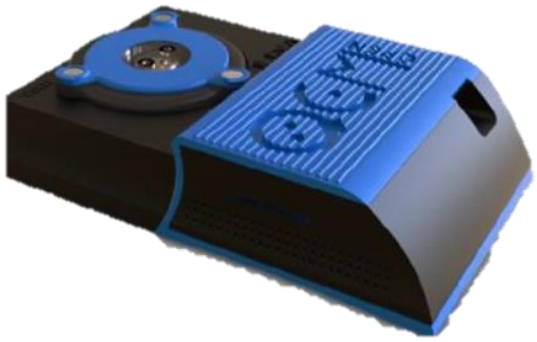

Figure 7 OpenQCM Wi2 created by Novatech S.r.l.

2.7. Clinical Performance of Five Top EUA-FDA Rapid Antigen Test for COVID-19 Diagnosis

Several studies have been conducted to show the importance of incorporating rapid antigen tests (RATs) in diagnosing high viral community by comparing their performance with the gold standard, RT-PCR, through the RATs precision in determining a person infectiousness with SARS-CoV-2.

Based on the clinical performance of EUA-FDA Ag tests reported by independent validation studies along with the test manufacturer study for each of the EUA Ag test, it was found based on a search results up until 30 April 2021, that the LumiraDx Ag test scored the highest sensitivity in clinical studies with a pooled sensitivity of 88.2% [95% CI 59.0% to 97.5%], and for rapid antigen test kits for COVID-19, it was found that the Standard Q nasal COVID-19 Ag kit of SD Biosensor, as of instrument-free Ag-RDTs, scored best with a 74.9% sensitivity [95% CI 69.3% to 79.7%] (Brümmer et al., 2021) (Khalid et al., 2022).

LumiraDx SARS-CoV-2 Ag is a rapid immunofluorescence Ag assay that qualitatively detects within 12 minutes the N antigen protein of SARS-CoV-2 virus. The test result is determined from the fluorescent amount that the LumiraDx Instrument

detects within the zone of measurement of the Test Strip. The fluorescent signal readout improves the sensitivity and is read by digital analyzers, making the technique more expensive compared to other Ag tests that do not use fluorescent signaling [8]. Standard Q nasal COVID-19 test by SD Biosensor scored the highest with a pooled sensitivity of 83% in terms of instruq1

Sofia SARS Antigen FIA test, is also a technique that uses fluorescent signal readout, which makes it more expensive than other Ag tests in order to detect N protein from SARS-CoV-2. In a recent review paper, it was found that SOFIA SARS-CoV-2 Ag FIA test showed a sensitivity of 66.0% [95% CI 51.73-78.48] for a PCR Ct value of less or equal to 35, and a sensitivity of 100% [95% CI 89.11-100] for a PCR Ct value of less or equal to 20, and a specificity of 100% (Al-Alawi et al., 2021). Smith et al. found that SOFIA SARS-CoV-2 Ag FIA has a 100% sensitivity for CT values of less or equal to 17.9, a value of 96.8%-97.2% sensitivity for CT values between 18 and 25.9, and a sensitivity of 71% for CT values of 26-29.9. The sensitivity was found to lower as the CT value becomes higher, reaching a value of 22.2% for CT value greater than 34 (Smith et al., 2021).

Abbott BinaxNOW Antigen Test has shown in one study that the sensitivity is of 87% for symptomatic cases and 71% for non-symptomatic in a high-volume self-referred testing site, the median CT value was found to be 25 (27 for non-symptomatic and 24.5 for symptomatic patients). For a CT values less than 25, the sensitivity is of 97%, while it is of 61% for CT values greater or equal to 25 (Siddiqui et al., 2021).

In another study carried by Pollock et al. in a high-throughput testing community site in Massachusetts, BinaxNOW showed a sensitivity for symptomatic adults of 96.5% (95% confidence interval [CI], 90.0 to 99.3), while a value of 84.6%

(95% CI, 65.1 to 95.6) for symptomatic children, and for both a specificity 100%. For asymptomatic cases, it was found that for children the sensitivity is of 65.4% (95% CI, 55.6 to 74.4) and for adults to be 70.2% (95% CI, 56.6 to 81.6). Specificity was also affected in asymptomatic cases for both adults and children, they were respectively 99.6% (95% CI, 98.9 to 99.9) and 99.0% (95% CI, 98.0 to 99.6). These data support the importance of using Ag test in symptomatic patients for better result. Also, in this study, it was shown that for CT values less or equal to 25 and CT values of less or equal to 30, the sensitivities were 99.3% and 95.8 respectively while it lowered for greater CT values (81.2% for CT values less or equal to 35). The paper highlighted also the importance to stick to the temperature recommended by the manufacturer as it will affect the performance of the Ag test assay. In fact, with temperature out of the temperature range scope provided by the manufacturer (46 to 58.5°F), the sensitivity dropped to 66.7% and specificity of 95.2% (Pollock et al., 2021).

Abbott Panbio COVID-19 Ag test kit has ranked second as an instrument-free Ag test. It has shown a pooled sensitivity of 75.9% in a recent meta-analysis conducted in 2021 by Khalid, M. F., et al. [16]. Panbio is an FDA Ag self-test is a read rapid immunoassay that qualitatively detects the N protein of SARS-CoV-2. It is a lateral flow assay that detects a probable infection within 15 minutes.

A comparative table is available in Appendix Table 2, whereby all of the tests are illustrated and compared in terms of sensitivity and specificity, and limit of detection of each of these five tests, along the other forty antigen tests that are EUA-FDA approved.

In a recent meta-analysis comprehensive review on RATs performance for diagnosing COVID-19 done in 2021, the various sampling swabs locations that are used

in COVID-19 testing were compared (Table 2). Nasal swabs scored the highest (83%, 95% CI: 80–86) followed by NP swabs (71%, 95% CI: 70–72), throat swabs (69%, 95% CI: 63–75) and saliva (68%, 95% CI: 59–77) in terms of sensitivity (Table 2). Saliva scored the lowest sensitivity among them, since the virus infects respiratory organs. To date, NP swabs are considered the COVID-19 gold standard specimen for laboratory diagnosis. The drawn conclusion on nasal swabs in this review by Khalid et al. might suggest that nasal swabs could replace NP swabs. Yet, it is important to conduct more studies evaluating the performance of nasal swabs samples to be able to have a more accurate comparative platform between nasal and NP swabs and draw a stronger conclusion on this basis (Khalid et al., 2022).

Subgroups	**Number of Studies**	**Total Number of Patients**	**Sensitivity [95% CI]**	**Specificity [95% CI]**
All studies	94	74445	0.70 [0.69-0.71]	0.98 [0.98-0.98]
Specimens				
Nasopharyngeal swabs	58	38548	0.71 [0.70-0.72]	0.98 [0.98-0.99]
Nasal swabs	4	4258	0.83 [0.80-0.86]	0.98 [0.98-0.99]
Throat swabs	2	3623	0.69 [0.63-0.75]	0.99 [0.99-1.00]
Saliva	2	432	0.68 [0.59-0.77]	0.97 [0.95-0.99]
Symptoms				
Symptomatic	30	24726	0.82 [0.82-0.82]	0.98 [0.98-0.98]
Asymptomatic	14	14926	0.68 [0.67-0.71]	0.99 [0.99-0.99]
CT values				
CT value ≤ 25	13	5378	0.96 [0.95-0.97]	0.99 [0.99-0.99]
CT value ≥ 25	12	6139	0.69 [0.67-0.71]	0.97 [0.96-0.97]
Countries				
Germany	14	14179	0.58 [0.56-0.60]	0.98 [0.98-0.98]

Spain	11	9391	0.71 [0.68-0.73]	0.99 [0.99-1.00]
Italy	10	11752	0.81 [0.79-0.83]	0.96 [0.96-0.97]
United States	8	10605	0.77 [0.75-0.79]	0.97 [0.97-0.97]
Japan	7	5192	0.72 [0.70-0.75]	0.99 [0.99-1.00]
Netherlands	7	8073	0.72 [0.70-0.75]	1.00 [0.99-1.00]
France	6	1858	0.58 [0.54-0.62]	1.00 [0.99-1.00]
Belgium	5	1634	0.73 [0.70-0.76]	0.84 [0.81-0.86]
Switzerland	3	2399	0.65 [0.61-0.70]	1.00 [1.00-1.00]
Chile	3	906	0.77 [0.69-0.85]	1.00 [0.99-1.00]
China	3	332	0.87 [0.77-0.97]	0.99 [0.97-1.00]
India	2	838	0.58 [0.52-0.63]	0.99 [0.98-1.00]

Table 2 The sensitivity and specificity of SARS-CoV-2 rapid antigen tests, in terms of specimens, symptoms, Ct values, and countries (Khalid et al., 2022).

2.8. Point-of-Care Diagnosis for COVID-19

The need for a point-of-care COVID sensor arises from the urgency to detect and control the spread of the virus quickly and effectively. Traditional laboratory-based testing methods often involve time-consuming processes, logistical challenges, and delays in obtaining results (Coarsey et al., 2017). In contrast, a point-of-care COVID sensor provides on-the-spot testing at the location where it is needed, without the need for samples to be sent to a centralized lab (Figure 8).

One of the primary advantages of a point-of-care COVID sensor is the rapid turnaround time for test results. With this technology, healthcare professionals can obtain results within minutes or hours, enabling immediate decision-making and appropriate actions (Etienne et al., 2021). This is particularly crucial in situations where quick identification of COVID-19 cases is vital for containment measures, contact tracing, and isolation protocols.

Another significant advantage is the convenience and accessibility it offers. Point-of-care COVID sensors can be deployed in various settings, including hospitals, clinics, airports, schools, workplaces, and community centers (Harpaldas et al., 2021). This accessibility allows for widespread testing and early detection of cases, even in remote or underserved areas where access to centralized laboratories may be limited. It can help in identifying asymptomatic or pre-symptomatic individuals, who can unknowingly spread the virus, and enable timely interventions to prevent further transmission.

Additionally, point-of-care COVID sensors can potentially reduce the burden on healthcare systems and alleviate pressure on laboratory capacities (Parupudi et al., n.d.)

.By decentralizing testing, these sensors enable healthcare professionals to efficiently screen and triage patients, ensuring that those in need of immediate care receive prompt attention, while also conserving resources for severe cases (Ding et al., 2021).

Furthermore, the portability and simplicity of point-of-care COVID sensors make them user-friendly and suitable for non-specialized healthcare settings (Parupudi et al., n.d.). Some sensors are designed to be handheld devices, while others can be integrated into existing diagnostic equipment or platforms. This versatility allows for ease of use and scalability, facilitating widespread adoption and deployment across different healthcare settings (Rasmi et al., 2021).

The need for point-of-care COVID sensors becomes even more critical during times of surges, outbreaks, or emergencies when timely detection and containment measures are crucial. By providing rapid, accessible, and accurate testing at the point of care, these sensors contribute to controlling the spread of the virus, minimizing the impact on public health, and saving lives (Ye et al., 2022).

It is important to note that while point-of-care COVID sensors offer valuable benefits, they should be used in conjunction with other public health strategies, including vaccination, mask-wearing, social distancing, and hygiene practices, to effectively combat the pandemic.

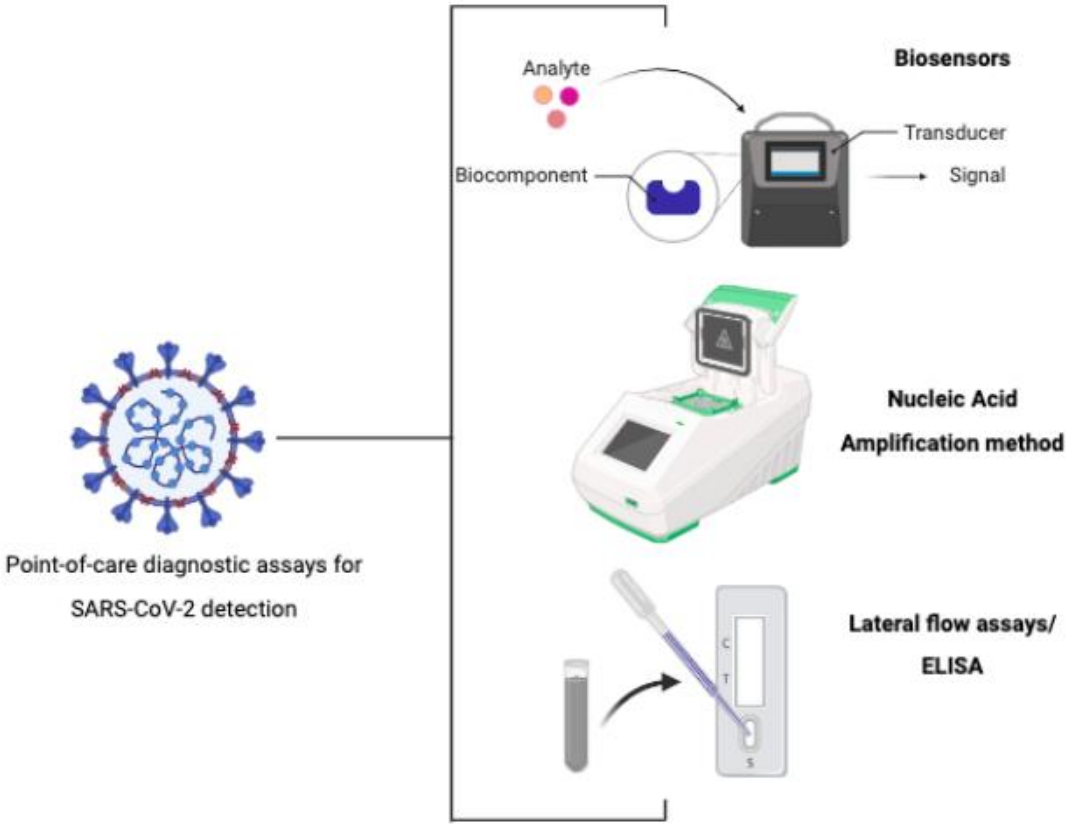

Figure 8 Point-of-care testing detection methods for COVID-19 (developed via Biorender.com) (Song et al., 2021)

CHAPTER 3

SPECIFIC AIMS

In this study, our primary objectives revolved around the development and characterization of a label-free surface functional immunoassay for the SARS-CoV-2 nucleocapsid antigen biomarker. We set out to achieve the following aims:

Firstly, to develop and characterize a label-free surface functional immunoassay specifically designed for detecting the SARS-CoV-2 nucleocapsid antigen biomarker. To accomplish this, we had a hypothesis that thiol-PEG-carboxyl (SH-PEG-COOH) could serve as a valuable crosslinker with a PEG spacer. Additionally, we believed that the EDC/NHS activation step played a crucial role in preparing amine-reactive esters for the COOH terminal, facilitating antibody coupling and immobilization on the gold QCM surface. To gain a comprehensive understanding of the surface chemistry, we employed various characterization techniques such as Digital Holographic Microscope (DHM), Fluorescence Microscopy, Scanning Electron Microscopy (SEM) with edx, and Raman Spectroscopy. The ultimate impact of achieving this aim was the development of a robust immunosensor surface chemistry that would yield high sensitivity and a low limit of detection (LoD) for detecting the viral antigen protein.

Our second aim involved determining the sensitivity and limit of detection (LoD) of the piezoelectric immunosensor we developed. We hypothesized that our piezoelectric sensor would exhibit high sensitivity due to its inherent nature as a piezoelectric device. To evaluate the sensitivity, we conducted a BSA protein experiment, enabling us to ascertain the sensor's performance in detecting minute amounts of the target biomarker. Furthermore, we determined the LoD as the lowest amount detected by our sensor. The significant impact of achieving this aim was the

creation of a low-cost, high-performance Quartz Crystal Microbalance (QCM) sensor (M. L. Khraiche et al., 2005).

Finally, we focused on developing a cross-reactivity test for the piezoelectric immunosensor we had developed. To ensure the specificity of our immunosensor, we conducted a pilot experiment using Influenza type A lysed inactivated virus. This experiment allowed us to verify that our immunosensor responds selectively to the target biomarker and does not produce false-positive results due to cross-reactivity. The impact of this aim was that the developed immunosensor could be utilized as an effective tool for the detection of clinical sample results.

To recap, the aims, approaches and impacts are as follow:

Aim 1: Developing and characterizing a label-free surface functional immunoassay for SARS-CoV-2 nucleocapsid antigen biomarker.

Hypothesis: We hypothesis that thiol-PEG-carboxyl (SH-PEG-COOH) is a useful crosslinker with PEG spacer, and that the EDC/NHS activation step is an important activation step that prepare amine-reactive ester for the COOH terminal useful for the antibody coupling and immobilization on gold QCM surface.

Approach: Characterizing the surface chemistry through various techniques: Digital Holographic Microscope (DHM), Fluorescence Microscopy, Scanning Electron Microscopy (SEM) - edx, Raman Spectroscopy.

Impact: Development of a strong immunosensor surface chemistry that yields high sensitivity and LoD for detection of viral antigen protein.

Aim 2: Determining the sensitivity and limit of detection (LoD) of our developed piezoelectric immunosensor.

Hypothesis: We hypothesis to have high sensitivity as we are dealing with a piezoelectric sensor.

Approach: Running a BSA protein experiment to determine the sensitivity of our sensor. The LoD was determined as the lowest amount detected by our sensor.

Impact: Low-cost, high performance QCM sensor.

Aim 3: Develop a cross-reactivity test to the specificity for our developed piezoelectric immunosensor.

Approach: Running a pilot experiment using Influenza type A lysed inactivated virus to ensure the specificity of our immunosensor.

Impact: The developed immunosensor can be used as an effective tool for clinical sample result detection.

CHAPTER 4

METHODOLOGY

4.1. Surface Chemistry

The gold electrode quartz crystal resonator chips were acquired from Novatech S.r.l OpenQCM. They have a resonating frequency of 10 MHz and a diameter of 14 mm. As mentioned earlier, the manufacturer specifies a nominal sensitivity of 4.42 x 10-9 g Hz-1 cm-2. To remove any organic material deposited on the gold electrodes, a strong acid piranha solution with a volume/volume ratio of 3:1 (H2O2+H2SO4) is used. The electrodes are immersed in the solution for 5 minutes, then rinsed with de-ionized water and dried in air for 15 minutes. (Geddes et al., 1995). The crystals were then treated with a 1M sodium hydroxide solution (NaOH) for a duration of 20 minutes, then rinsed with de-ionized water (DIW) (Michel et al., 2005).

In this study, we used Thiol-PEG-carboxyl as a layer that serves for the functionalization and immobilization of antibody to capture the target nucleocapsid protein obtained post-lysing of a heat SARS-CoV-2 inactivated virus.

Thiol-PEG-carboxyl was chosen for this work, since it is known to be a useful crosslinking agent with PEG spacer as it has both thiol and carboxyl groups attached on it, as well as a good surface functionalizing agent. It is also highly hydrophilic, which makes it convenient for water environment. Polyethylene glycol, PEG, significantly reduces nonspecific binding (Prime & Whitesides, 1991) (Bentzen et al., 2005) (Po-Chiao et al., 2006) (Zheng et al., 2003) (Verma & Rotello, 2005) (Srivatsan Kidambi et al., 2004).

Firstly, the carboxylic group provides a reactive site for covalent bonding with various substrates. By activating the carboxylic group using appropriate coupling agents, such as EDC and NHS, it becomes capable of forming stable amide or ester bonds with amino or hydroxyl groups on the surface of different materials (Po-Chiao et al., 2006) (Zheng et al., 2003) (Bala et al., 2007)

Secondly, the thiol group in thiol-PEG-carboxymethyl interacts with the gold surface of our QCM, enabling a process called chemisorption forming strong gold-thiolate (Au-S) covalent bonds with gold. These interactions are known as formation of a self-assembled monolayer (SAM) on gold or thiol-gold chemistry. (Xue et al., 2014) (W. Wang et al., 2013). The chemisorption process takes place because of the affinity of gold (Au) for sulfur (S) atoms, thus forming Au-S interactions. Sulfur atom in -SH group displaces an Au atom, causing the formation of Au-S strong covalent. The PEG spacer provides flexibility and sterically hinders the adsorption of other molecules, preventing nonspecific binding and enhancing stability. (Xue et al., 2014)

Furthermore, thiol-PEG-carboxymethyl coatings can be tailored to specific requirements by adjusting the length or composition of the PEG linker, varying the density of carboxylic acid groups, or incorporating other functional moieties. This versatility enables the customization of coatings to achieve desired surface characteristics, such as enhanced biocompatibility, reduced fouling, improved stability, or specific targeting capabilities. . (Xue et al., 2014) (W. Wang et al., 2013)

The activation of the carboxylic group of thiol-PEG-carboxymethyl is a crucial step in bioconjugation processes (AlChamaa & Khraiche, 2022) (Alawieh et al., 2019) (Habli et al., 2022), enabling the subsequent binding of specific molecules. In this

particular case, the activation reaction involves the use of 1-Ethyl-3-[3-dimethylaminopropyl] carbodiimide (EDC) and N-Hydroxysuccinimide (NHS) (*MAN0011309_NHS_SulfoNHS_UG.Pdf*, n.d.). This activation process is commonly employed in bioconjugation techniques to facilitate the covalent attachment of biomolecules. During the activation reaction, the EDC molecule reacts with the carboxylic group of thiol-PEG-carboxymethyl, resulting in the formation of an O-acylisourea intermediate. This intermediate is susceptible to hydrolysis and can react nonspecifically with nucleophiles present in the reaction mixture. To prevent unwanted side reactions and enhance selectivity, NHS is added to the reaction mixture. NHS reacts with the O-acylisourea intermediate to form a stable NHS ester (*MAN0011309_NHS_SulfoNHS_UG.Pdf*, n.d.).

In the subsequent step, the amine-reactive NHS ester is ready to react with the amine groups present on the SARS-CoV-2 IgG monoclonal antibody (mAb). The amine groups on the mAb readily attack the activated ester, resulting in the formation of a stable amide bond. This covalent attachment allows for specific binding and immobilization of the SARS-CoV-2 IgG mAb.

The reaction is typically performed in the presence of a buffer substance to maintain the desired pH and promote efficient reaction kinetics. In this case, 2-(N-morpholino) ethane sulfonic acid (MES) is mentioned as the buffer substance, which is known to be a good buffering agent within the pH range of 5.5-6, slightly acidic, to optimize the reaction kinetics and stability. MES helps maintain the appropriate pH for the activation reaction as a buffer (Ishii et al., 2005).

Additionally, sodium chloride (NaCl) is included in the reaction mixture to prevent nonspecific binding of proteins. NaCl is often used in bioconjugation reactions

to minimize unwanted interactions between biomolecules and surfaces, preventing nonspecific binding and improving the specificity of the reaction. In other words, NaCl helps minimize electrostatic interactions and reduce the potential for undesired protein adsorption or binding, thereby improving the specificity of the conjugation reaction (Dahal & Schmit, 2018).

In summary, the activation reaction utilizing EDC and NHS in the presence of MES and NaCl at pH 5.5-6 facilitates the formation of amine-reactive esters. These esters enable the specific binding and immobilization of the SARS-CoV-2 IgG2a monoclonal antibody through the formation of stable amide bonds. In the presence of the amine groups on the SARS-CoV-2 IgG2a mAb, the NHS ester reacts with the amine groups, leading to the formation of stable amide bonds. The resulting covalent attachment between the activated thiol-PEG-carboxymethyl and the SARS-CoV-2 IgG2a mAb allows for specific binding and immobilization. The antibody will permit the viral nucleocapsid antigen to attach to it, after lysing the inactivated SARS-CoV-2 virus.

The protocol steps are then as followed and it is illustrated in Figure 9:

1. Washing with distilled water (DIW) after cleaning the sensors with piranha and sodium hydroxide to create a humid environment for PEG.
2. Addition of 1 mg/mL solution of thiol-PEG-carboxyl prepared (HS-PEG-COOH, MW 5K), purchased from Laysan Bio Inc. (Alabama, USA), in DIW, and incubate for 2 hours at room temperature.
3. Washing with distilled water, the best approach is to pipette in and out several time, for our PEG to be always hydrated.

4. Activate the COOH- group of the COOH-PEG-SH using the two-step reaction with the activation prepared out of 0.4 mg EDC, 0.6 mg NHS, 0.1 M of MES, and 0.5 M of NaCl at pH 5.5-6.0, and incubate for 15 minutes at room temperature.
5. Addition of 1.4 μL of 20 mM of beta-mercaptoethanol to quench 1-Ethyl-3-[3-dimethylaminopropyl] carbodiimide.
6. Washing several times with phosphate buffer solution (PBS) prepared out of 0.1M sodium phosphate, 0.15 M NaCl, and adjusted at pH 7.2-7.5. The best approach is to pipette in and out, to keep our PEG hydrated.
7. Addition of 20 μL of SARS-CoV-2 Nucleocapsid Protein (E8R1L) Mouse monoclonal Antibody mAb, purchased from Cell Signaling Technology Inc. (Massachusetts, USA), and diluted with PBS.
8. Incubation is done for 2 hours at room temperature.
9. Addition of ethanolamine (ETA) to inactivate NHS, the amine conjugation reaction.
10. Washing with PBS is performed several times, by pipetting in and out.
11. After preparing the best lysis buffer for lysing SARS-CoV-2 heat inactivated virus sample (NR-52286, bei resources), 20 μL of lysed heat-inactivated SARS-CoV-2 virus containing the nucleocapsid antigen is added to the surface.

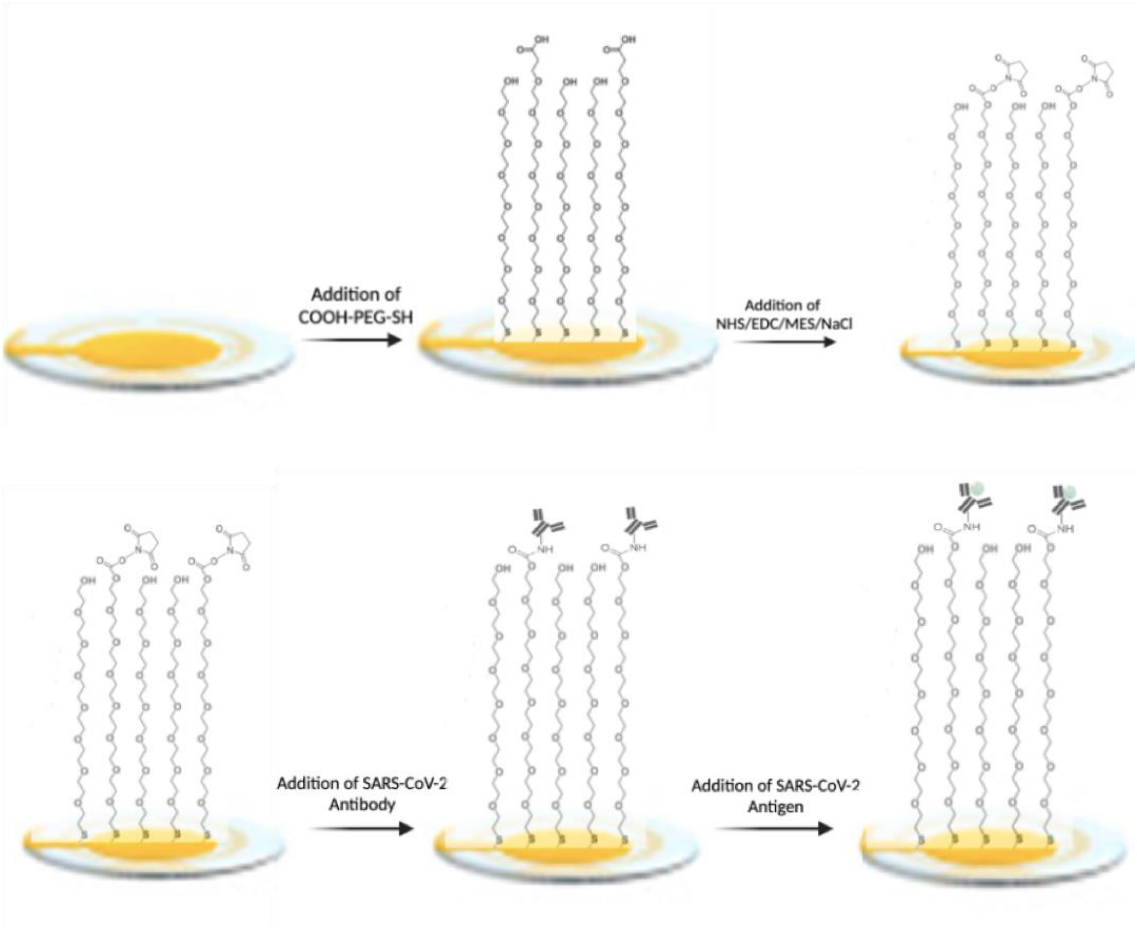

Figure 9 Surface functionalization procedure for SARS-CoV-2 nucleocapsid antigen detection.

The process of lysing an inactivated virus involves breaking down the viral envelope and releasing the genetic material contained within for downstream analysis. In order to achieve this, a lysis buffer is typically used.

The selection of a lysis buffer for lysing an inactivated virus depends on several factors to ensure efficient and effective disruption of viral particles. Some key considerations for properly choosing a lysis buffer are as follows (Elveborg et al., 2022):

1. Viral characteristics: Viruses may have different sensitivities to lysis conditions depending on the virus composition and structure. Enveloped

viruses for instance may require detergents to disrupt their lipid membrane, while non-enveloped viruses may require more aggressive means to release the viral components.

2. pH: It is important to consider the optimal pH range for enzyme function and viral stability. Viruses may be sensitive to pH variations, choosing a lysis buffer with a suitable pH may help retaining the viral integrity and promoting effective lysis.
3. Detergents: Triton X-100, SDS, or NP-40 are frequently used detergents to break lipid membranes and solubilize viral proteins. The choice and concentration of detergents depend on the specific virus and the type of viral particle to be lysed.
4. Chelating agents: Some lysis buffers include chelating agents like EDTA to sequester divalent cations, which can impair enzymatic activity or enhance viral aggregation. EDTA contributes to the viral components' stability during lysis.
5. Buffer components: the inclusion of buffering agents such as Tris-HCl or phosphate can stabilize the pH and maintain the selected lysis buffer.
6. Enzymes: Enzymes such as proteinase K or RNase may be introduced in the lysis solution depending on the downstream applications to destroy undesired proteins or nucleic acids, respectively.

In this study, a series of characterization techniques were conducted to determine the most suitable lysis buffer performance that would effectively break down SARS-CoV-2 and Influenza type A inactivated viruses while preserving the surface chemistry coated on our sensor gold surface.

The first studied lysis buffer, Lysis Buffer # 1 (final pH of 7.2), consists of (Raziq et al., 2021):

- 1.5 % Triton X-100. Nonionic detergent Triton X-100 is often used in lysis buffers to rupture the viral envelope and liberate viral components. It aids in the solubilization of viral membrane lipids and proteins.
- 27.5 mM Tris-HCl. Tris-HCl is a buffering agent that keeps the lysis buffer's pH stable. The particular pH may differ based on the virus and the desired lysis conditions.
- 0.1% SDS. Sodium Dodecyl Sulfate (SDS) is an anionic detergent that breaks protein-protein connections and disintegrates proteins, allowing for easier solubilization and discharge during lysis.
- 12.5 mM EDTA. Ethylenediaminetetraacetic acid (EDTA) is a chelating agent that sequesters divalent cations, including magnesium and calcium, which can hinder enzymatic processes. During lysis, EDTA aids in stabilizing the viral components.

Lysis Buffer #2, the second examined lysis buffer, is made up of the following ingredients (Singh et al., 2022):

- 50 mM $NaH_2PO_4.H_2O$: Sodium dihydrogen phosphate monohydrate is a buffering reagent that contributes in maintaining a stable lysis buffer pH. It maintains the appropriate pH for the nucleocapsid detection assay.
- To establish an isotonic environment, 300 mM NaCl is added to the lysis buffer. This helps to maintain adequate osmotic balance and protects the virus particles throughout the lysis process.

- 10 mM Imidazole, pH 8.0: Imidazole is a buffering reagent that preserves a specific lysis buffer pH. The pH is set at 8.0, in this case. It was found that at this concentration and pH, Imidazole can effectively lyse SARS-CoV-2 viral particles, therefore releasing the nucleocapsid protein for subsequent detection.

After choosing the best lysis buffer, it is combined with SARS-CoV-2 inactivated virus sample, and a 1:3 (volume of the virus sample to the total mixture volume) dilution ratio is performed on the viral sample using the chosen lysis. The mixture is then incubated under specific conditions, such as temperature and duration, to promote lysis. In this study, the viral sample is heated at 56°C for 30 minutes.

Lysis buffer will then disrupt the viral envelope, which consists of a lipid bilayer, thereby allowing the release of the viral particles' contents, including the nucleocapsid viral protein. The incubation conditions set helps in achieving effective lysis while keeping functionality and integrity of the released components (Perumal et al., 2020).

A brief centrifugation is performed to attain the desired lysate separation, which contains the released viral components. The heavier components, such as cell debris or big particles, settle to the bottom of the tube when the lysate is spun, while the lighter supernatant contains the desirable viral components, including the nucleocapsid protein. The centrifugation step aids in getting a cleaner lysate for further downstream analysis, by limiting interference from undesirable components, resulting in a cleaner and more concentrated specimen for subsequent analysis (*SARS-CoV-2 Intact Virus Purification - LB*, n.d.).

CHAPTER 5

RESULTS & DISCUSSIONS

5.1. Surface Chemistry Characterization

Surface characterization techniques provide valuable insights into the composition, structure, and properties of surfaces, including surface chemistry, morphology, energy, functional groups, and molecular interactions. In our case, these techniques are applied to investigate the coverage and stability of our functionalized surface when separately applying each of lysis buffer #1 (contains a detergent called Triton X-100) and lysis buffer #2 (refer to the methodology section) onto the surface of two distinct gold quartz crystal sensors coated with the adopted surface chemistry. It is important to note that no inactivated viruses (SARS-CoV-2 and Influenza type A) have been added to the lysis buffer during these characterization tests. Thus, prior to introducing any of the inactivated viruses, it is crucial to select an effective lysis buffer that can successfully lyse SARS-CoV-2 and Influenza type A without compromising the integrity of the surface chemistry coated (COOH-PEG-SH) on our sensor surface. Consequently, a series of characterization tests were conducted to choose the appropriate lysis buffer that would fulfill these requirements:

5.1.1. Digital Holographic Microscope (DHM)

Reflection DHM is an instrument developed by Lyncée Tec (Figure 10), which studies the topography of a purely reflecting sample surface, allowing the measurement of the sample's reflected wavefront. This equipment allows the dynamic measurements

from sub-nano level to hundreds of microns vertical resolution (*Reflection DHM[r] - LyncéeTec*, n.d.).

Figure 10 DHM by Lyncée Tec

Digital Holographic Microscopy (DHM) is a label-free imaging technique that has been employed for surface chemistry characterization. It enables the quantitative visualization of surface topography, refractive index, and thickness of transparent samples without the need for staining or labeling. DHM allows the user to get the surface profile (topography profile) of the sample surface being observed on the DHM microscope, as well as studying the surface roughness, and a 3-D representation of the surface in question.

DHM has been utilized for studying the morphology of various materials, including micro- and nanoparticles, thin films, and nanowires. The technique enables the non-destructive imaging of samples, providing high-resolution images and quantitative information on surface topography and roughness.

In surface chemistry characterization, DHM has been applied to study the surface properties of sensors, and biomaterials, such as cell-substrate interactions and

surface modifications. It has been utilized to visualize the changes in surface morphology and topography caused by chemical treatments, providing valuable insights into the chemical mechanisms of surface modifications. (Marquet et al., 2005).

DHM has also been used for the analysis of micro- and nanoparticles, providing information on their size, shape, and surface properties. The technique enables the imaging of nanoparticles in a label-free manner, providing valuable insights into their physical and chemical properties. (Marquet et al., 2005).

In the context of the Digital Holographic Microscope developed by Lyncee Tech, an important parameter called "Sa" refers to the surface roughness parameter known as "arithmetic mean roughness" or "average roughness." It is measured in nanometers (nm). It provides information about the average roughness of a surface being analyzed. Surface roughness is a characteristic of the surface texture and is defined as the deviations of the surface profile from the mean line within a specified evaluation length. The Sa parameter quantifies the average deviation of the surface from its mean position over the evaluation length.

By monitoring Sa, one can observe and evaluate the binding events occurring on the gold surface. As molecules or analytes bind to the surface, they may alter the surface roughness, leading to changes in the Sa value. These changes can indicate the presence and extent of binding between the target molecules and the gold surface.

Sa (nm) helps in assessing the surface quality, and studying the impact of surface roughness on various applications. The Digital Holographic Microscope captures holographic images and uses advanced algorithms to calculate parameters such as Sa to provide detailed surface analysis and characterization.

Figure 11 shows DHM images of a clean new sensor, washed with acid piranha, NaOH, then distilled water and dried, showing an average roughness of 2.22 nm. As we added 1 mg/mL COOH-PEG-SH, then washed with DIW and dried, we noticed that the roughness went up to reach a mean Sa value of around 4.84 nm. Then, as we continued by adding SARS-CoV-2 N mAb, then washing, quenching, and drying, we noticed that the mean roughness increased to 48.18 nm. It is worth noting, that the average Sa (nm) is calculated by performing three replicates of each of the sensors states in Figure 11 and Figure 12.

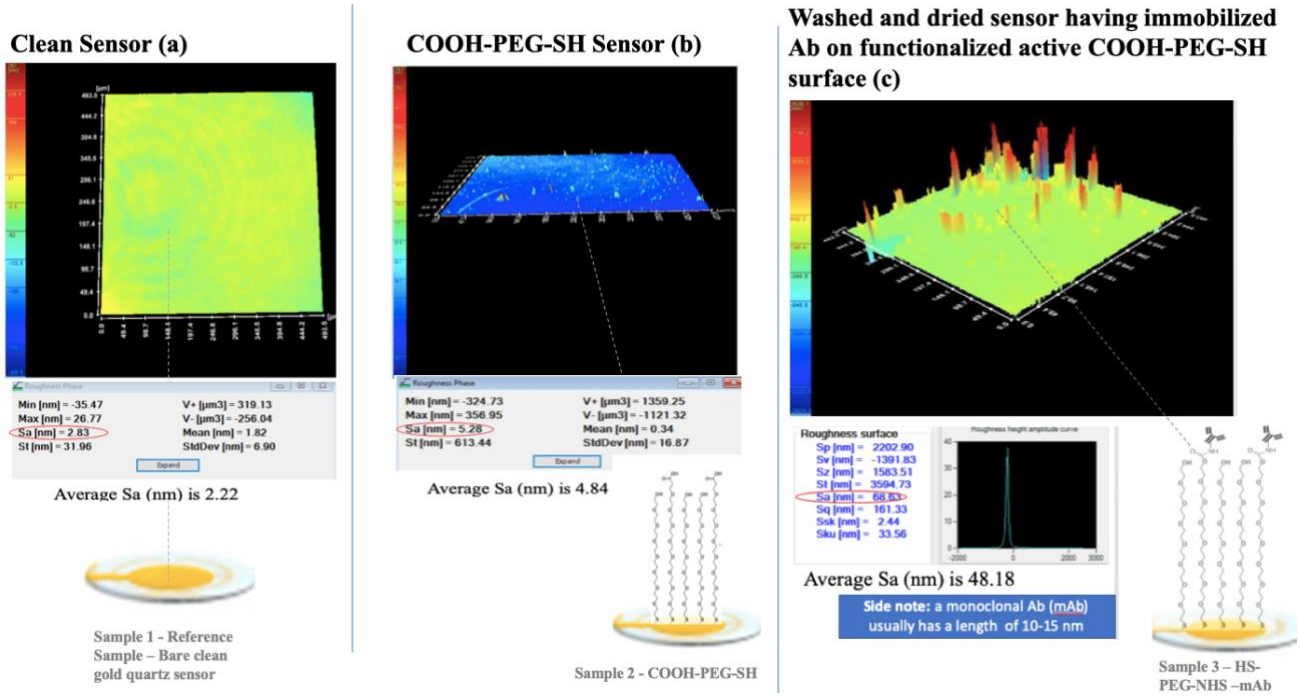

Figure 11 DHM Images of a clean sensor (a), a sensor with COOH-PEG-SH (b), and a sensor with Ab immobilized on activated form of COOH-PEG-SH layer (c).

Buffer # 1 is added to adhered SARS-CoV-2 N mAb on the functionalized surface, then washing excess buffer #1 and drying. The average surface roughness was

noticed to be 50.28 nm (Figure 12). Same protocol as buffer #1 was done for buffer #2, the average surface roughness was noticed to be 36.64 nm (Figure 12).

Figure 12 also shows secondary antibody binding on primary antibody over our functionalized surface, and showing an average Sa of 54.08 nm.

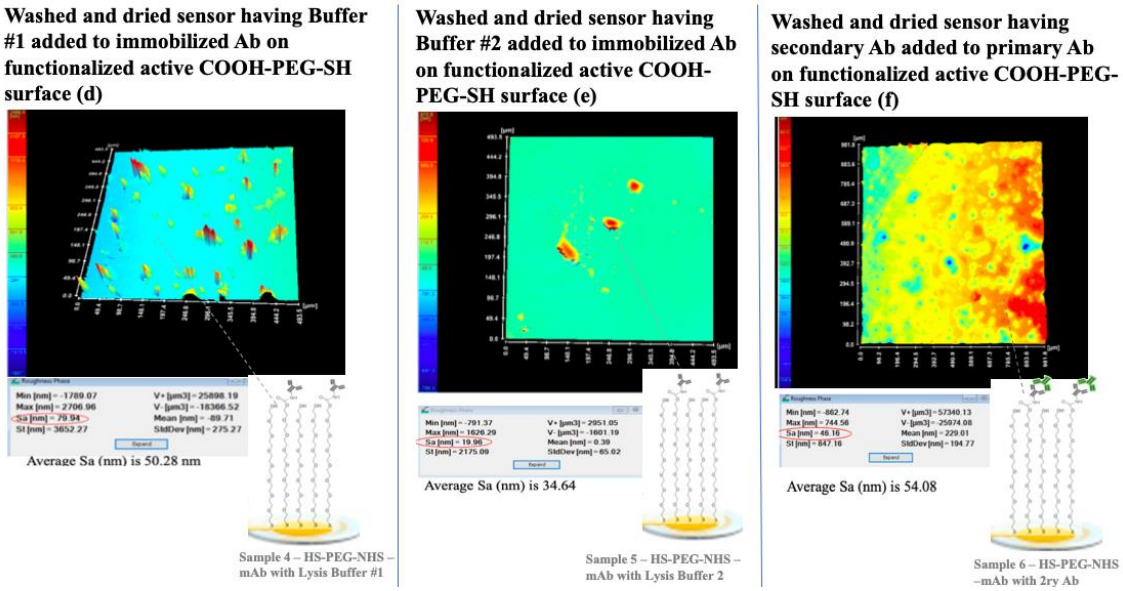

Figure 12 DHM Images from left to right: of a sensor having activated form of COOH-PEG-SH with antibodies, followed by the addition of buffer 1 (d); a sensor having activated form of COOH-PEG-SH with antibodies, followed by the addition of buffer 2 (e); and the third sensor is having activated form of COOH-PEG-SH with primary antibody, followed by addition of secondary antibody (f).

After washing and drying the BSA protein added over a bare cleaned gold quartz crystal surface, the average Sa was shown to be 17.65 nm (Figure 13).

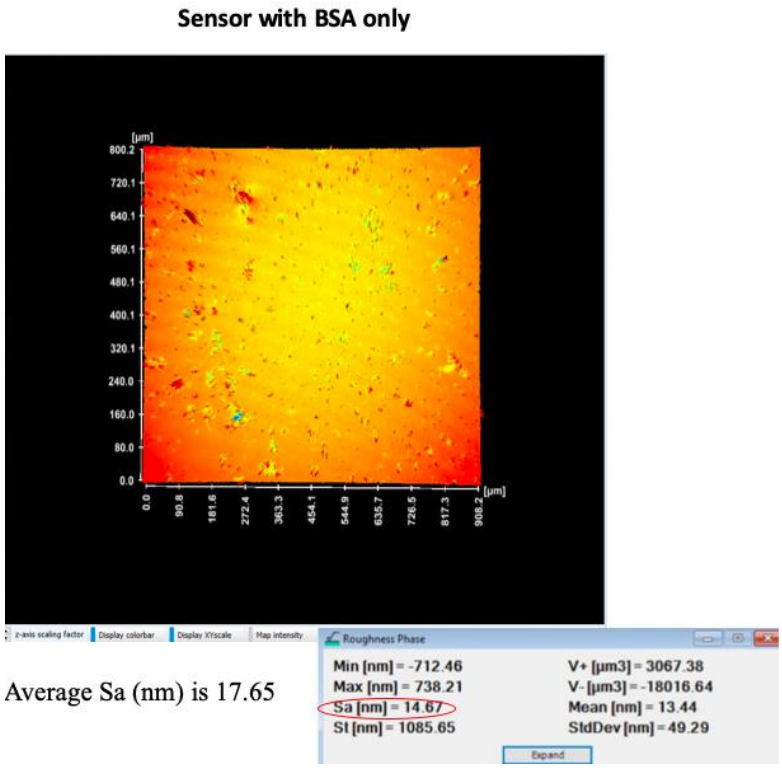

Figure 13 Bare sensor with BSA protein only

5.1.2. Fluorescence Microscopy - Immunofluorescence

Fluorescence microscopy is a powerful imaging technique employed to visualize and study fluorescently labeled samples. It utilizes the principle of fluorescence, where certain molecules, known as fluorophores, absorb light at a specific wavelength and emit light at a longer wavelength. This emitted light is detected and captured by the microscope, allowing for the visualization of specific molecules or structures within a sample (Lichtman & Conchello, 2005).

In this study, an antibody Goat anti-Mouse IgG (H+L) Cross-Adsorbed Secondary Antibody, Thermofisher, Alexa Fluor 488 with our primary antibody. This is a common technique used in fluorescence microscopy, known as immunofluorescence staining. The primary antibody is designed to specifically bind to the target antigen or protein of interest within the sample, acting as a molecular probe, recognizing and

binding to the target molecule. However, the primary antibody itself is not directly visible under a fluorescence microscope. (Du et al., 2017)

To visualize the location and distribution of the primary antibody, a secondary antibody is used. The secondary antibody is labeled with a fluorophore, typically a fluorescent dye, that emits light at a specific wavelength when excited by the appropriate light source. The secondary antibody specifically recognizes and binds to the primary antibody, forming a fluorescent complex. This allows the specific target molecule labeled with the primary antibody to be visualized as a fluorescent signal under the fluorescence microscope. (Sebestyén et al., 2002)

The fluorescence microscopy technique provides several advantages. It offers high sensitivity, allowing for the detection of low-abundance molecules or structures within a sample. It also enables multiplexing, where multiple target molecules can be labeled with different fluorophores simultaneously, allowing for the visualization of multiple targets in the same sample (Lewis et al., 2021). Fluorescence microscopy is widely used in various fields, including cell biology, immunology, neuroscience, and molecular biology, for studying cellular processes, protein localization, and interactions (Choi et al., 2015).

Figures 14 and 15 show that by utilizing the fluorescence microscopy technique, the fluorescence signal visualized indicates the successful binding of the secondary antibody to the primary antibody, and thus the immobilization of the antibody complex on the activated COOH-PEG-SH layer.

The detection of fluorescence provides evidence that the desired interaction and immobilization have occurred, confirming the successful development of the immunoassay. This information is crucial for assessing the effectiveness of the surface

chemistry and for later determining the sensitivity and limit of detection of the developed immunosensor.

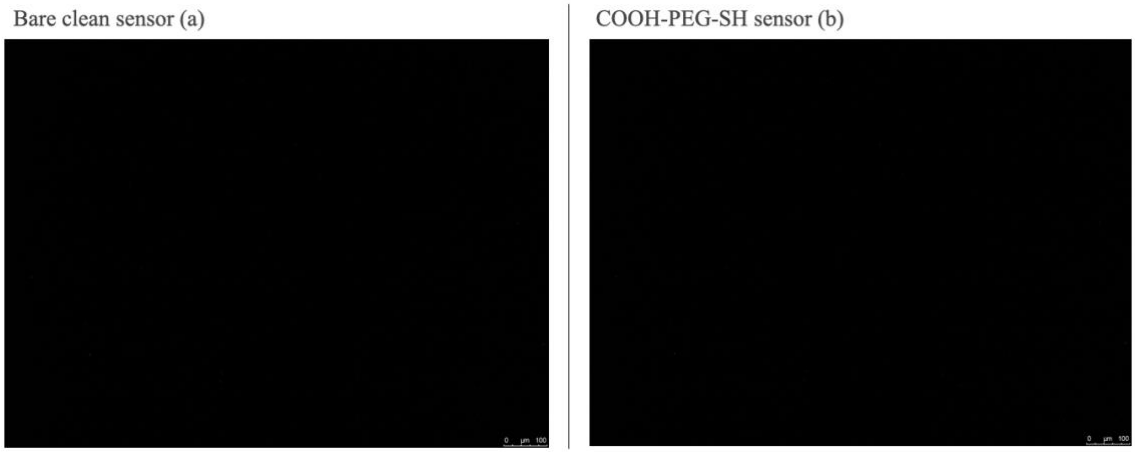

Figure 15 Up-Right Microscope Images of a bare clean sensor (a) and a washed and dried sensor having a layer of COOH-PEG-SH (b) showing no traces of fluorescence.

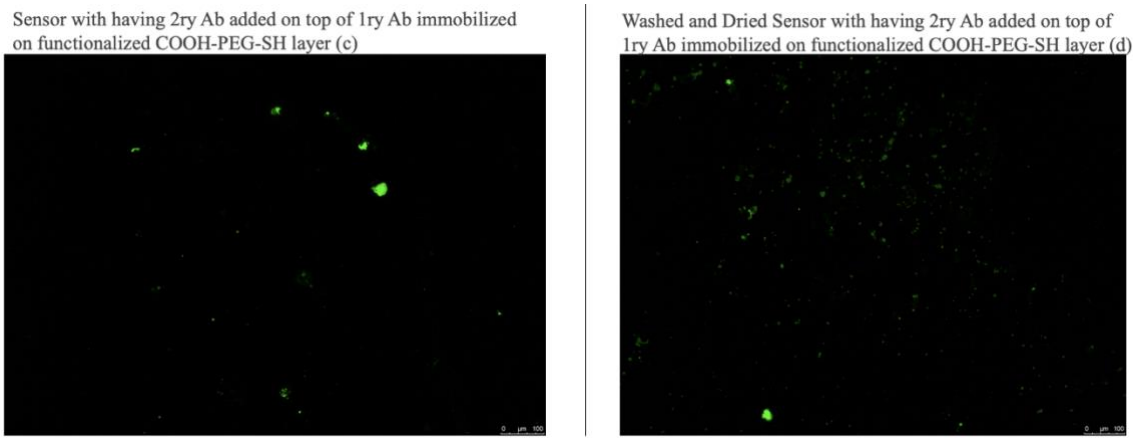

Figure 14 Up-Right Microscope Images of a sensor having aggregates of 2ry Ab on top of 1ry Ab immobilized on a layer of activated thiol-polyethylene glycol-carboxyl (c) and a washed and dried sensor having aggregates 2ry Ab on top of 1ry Ab immobilized on a layer of activated thiol-polyethylene glycol-carboxyl (d) showing fluorescence.

5.1.3. SEM and Edx

SEM with Energy Dispersive X-ray spectroscopy (EDX) is a strong surface analysis approach utilized in materials research and surface chemical characterization. It enables comprehensive imaging of a sample's surface topography and offers information on the elemental composition of the sample's surface (Tarhini et al., 2022) (Joshi et al., 2008).

The SEM scans the sample's surface with a focused stream of electrons. When an electron beam interacts with a material, it produces a variety of signals, including secondary electrons, backscattered electrons, and distinctive X-rays. These signals are recognized and processed to generate a surface picture of the sample. (Kannan, 2018)

The Energy Dispersive X-ray spectroscopy (EDX) method is used in conjunction with the SEM to study the elemental composition of the sample. EDX makes use of the X-rays generated by the sample when it is blasted with an electron beam. These X-rays are element-specific and have distinct energy signatures. (Titus et al., 2019).

The system analyzes the energy and intensity of the X-rays collected by the EDX detector to identify the elements present on the surface. This data is then utilized to generate an elemental map or spectrum, which provides both qualitative and quantitative information about the sample's makeup.(Guzman-Santiago et al., 2021).

SEM-EDX is widely used to evaluate the surface morphology and elemental distribution of samples in a variety of domains, including materials science, metallurgy, geology, and biological sciences. It can detect atoms as low as 0.1 to 0.01 weight

percent, depending on the sample and experimental circumstances, and can detect elements as high as atomic number 5 (boron).(Luitjohan, 2018).

The SEM-EDX technology is extremely useful for surface chemistry characterization because it allows researchers to see and study the elemental composition of a sample's surface with great spatial resolution. It can offer information on the surface's chemical composition, contamination, and elemental distribution, assisting in the knowledge of surface reactions, material characteristics, and surface changes. (Patil et al., 2022)

In the context of monitoring the binding process on a gold surface, SEM and EDX can provide evidence of binding by analyzing the changes in surface morphology and elemental composition (Cañamares et al., 2005):

- By comparing SEM images before and after each addition, one can visually observe any changes in surface morphology that may indicate the presence of bound molecules or analytes. These changes could include the formation of aggregates, clusters, or a different distribution pattern on the surface.
- By analyzing the elemental composition, EDX can provide information about the presence of specific elements associated with the binding process. If a specific binding molecule contains a unique element, EDX can confirm its presence on the gold surface.

By combining SEM and EDX, visual and elemental information regarding the binding process on the gold surface are acquired. These techniques can provide valuable evidence and support the observation of binding events, helping to confirm the successful binding and assess the effectiveness of the adopted surface chemistry.

In this context, we are observing if buffer # 1 and buffer #2 could lead to any disruptions to our functionalized surface, as we are adding them on top of SARS-CoV-2 N mAb.

SEM images are found on the right side of each of figures: 16, 17 and 18, and in Figure 19. Edx Spectrum analysis images are shown on the left side of each of figures: 16, 17, 18.

Figure 16 SEM image (right side) shows patterns of adhered COOH-PEG-SH on our gold electrode surface of the quartz crystal sensor. On the left side, Edx image shows the following elements: Silicon (Si), Gold (Au), Oxygen (O), Carbon (O), and Sulfur (S). Si appeared as we are working on a quartz sensor, and quartz is a crystalline made of silicon dioxide (SiO_2), and Au is from the gold electrode surface of the quartz crystal. Carbon, Oxygen, and Sulfur are indications of the presence of thiol-PEG-carboxymethyl. It is worth mentioning that in energy-dispersive X-ray spectroscopy (EDX), hydrogen (H) is not typically detected or quantified as an element due to its low atomic number and weak X-ray emissions (Hodoroaba, 2020). EDX is a technology that detects and analyzes distinctive X-rays generated by elements in a sample when blasted with high-energy electrons or X-rays. However, because hydrogen has a low atomic number and weak X-ray emissions, it is difficult to detect with EDX. It is worth mentioning that Si and Au will be present most because of the gold quartz crystal we are using on our surface chemistry.

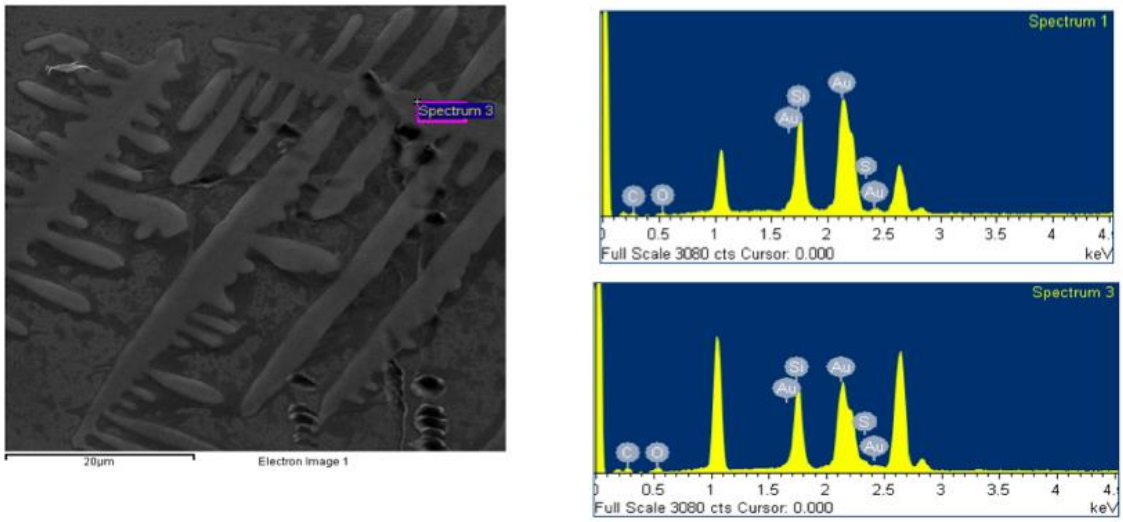

Figure 16 SEM and EDX analysis of a washed and dried sensor having a layer spread of COOH-PEG-SH.

Figure 17 depicts a macroscopic view of different patches of COOH-PEG-SH on our gold-functionalized surface. It is important to note that in this case, after adding the SARS-CoV-2 N monoclonal antibody (mAb) to our functionalized surface, buffer #1 was applied. However, the antibody itself is not visible in the scanning electron microscopy (SEM) image on the right side of the figure, which has a scale of 70 µm. This is because the height of the antibody is typically in the range of 10 to 15 nm, which is much smaller in comparison. Nonetheless, the analysis of the energy-dispersive X-ray spectroscopy (EDX) spectrum revealed the appearance of nitrogen (N) as a new element. This finding serves as evidence for the presence of the antibody adhered to our surface, indicating the formation of a stable amide bond between the antibody and the COOH-PEG-SH following activation through the EDC/NHS reaction. Therefore, it can be concluded that buffer #1 did not remove or disrupt the antibody or the COOH-PEG-

SH layer.

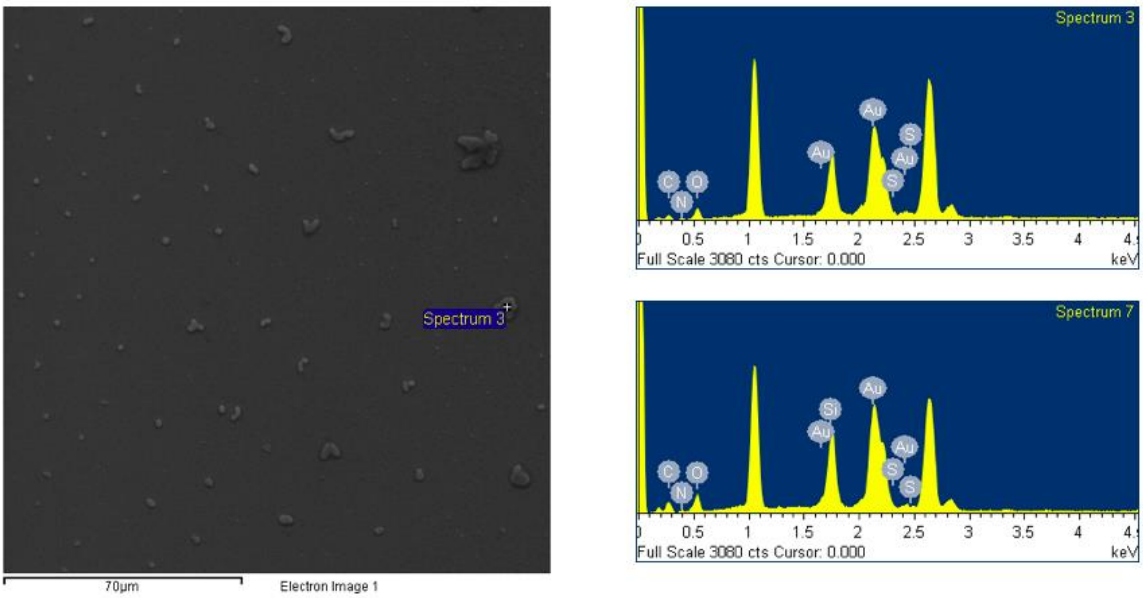

Figure 17 SEM and Edx analysis of a washed and dried sensor having buffer 1 added on top of immobilized mAb over crystals of activated functionalized COOH-PEG-SH.

Figure 18 also depicts scattered patches of COOH-PEG-SH at a scale of 70 µm on our functionalized gold quartz crystal surface. It is noteworthy that in this case, after the addition of the SARS-CoV-2 N monoclonal antibody (mAb) to our functionalized surface, buffer #2 was applied. However, as previously mentioned, the antibody itself is not visible in the micrometer-scale scanning electron microscopy (SEM) image shown on the right side of the figure due to its significantly smaller height, typically ranging from 10 to 15 nm. Additionally, the analysis of the energy-dispersive X-ray spectroscopy (EDX) spectrum revealed the presence of nitrogen (N), as well as titanium (Ti), sodium (Na), and chloride (Cl). It should be noted that titanium originates from the substrate added to the gold electrode surface of our quartz crystal from Novatech OpenQCM sensors, while sodium and chloride are constituents of the purchased SARS-

CoV-2 N (E8R1L) mAb antibody from Cell Signaling Technology. These findings provide conclusive evidence of the antibody's attachment to our surface, indicating the formation of a stable amide bond between the antibody and the COOH-PEG-SH layer following activation through the EDC/NHS reaction. Therefore, it can be inferred that buffer #2 also did not cause the removal or disruption of the antibody or the COOH-PEG-SH layer.

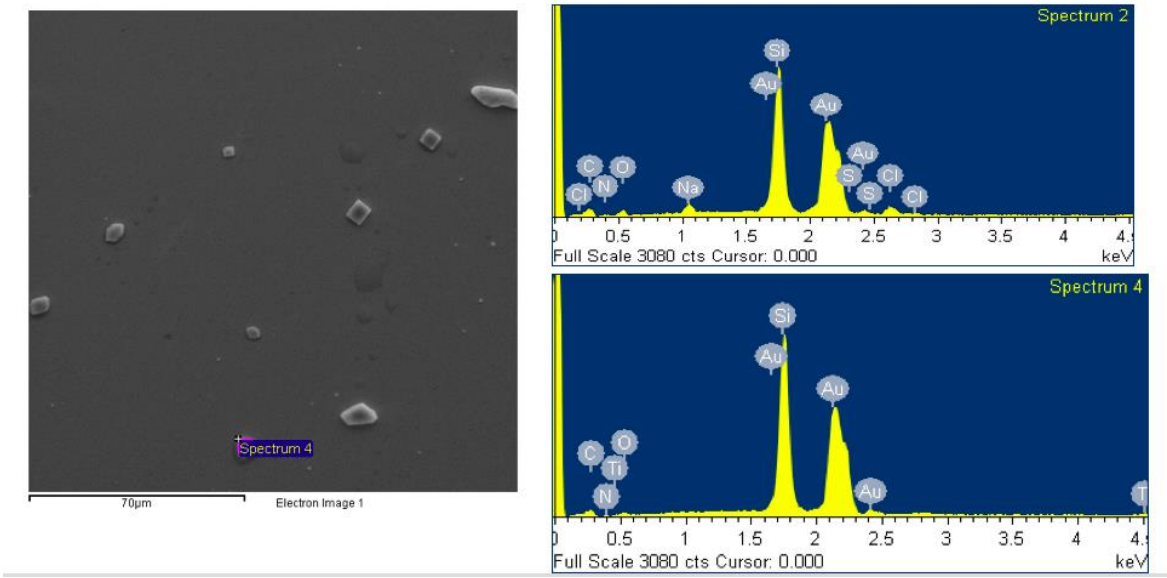

Figure 18 SEM and EDX analysis of a washed and dried sensor having buffer 2 added on top of immobilized mAb over crystals of activated functionalized COOH-PEG-SH.

Figure 19 shows SEM images from right to left of dispersed patches of: first COOH-PEG-SH activated using EDC/NHS followed by addition of SARS-CoV-2 N mAb (a), followed by addition of buffer #1 secondly (b), and lastly the addition of buffer # 2 instead of buffer #1 on the monoclonal antibody over our functionalized surface (c). Notably, even after the introduction of buffer #1 and buffer #2, patches of

COOH-PEG-SH are still visible, indicating that the COOH-PEG-SH remains intact on the surface.

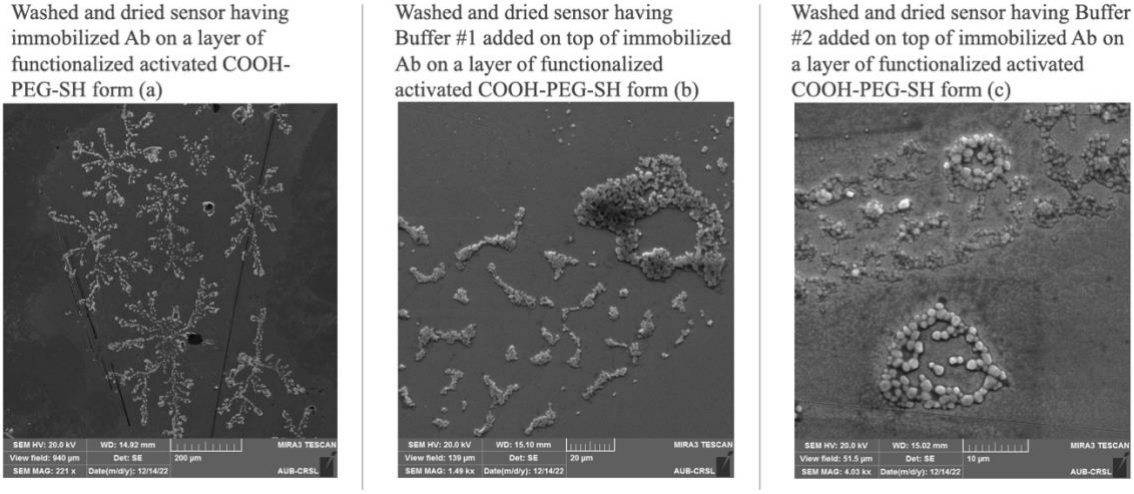

Figure 19 SEM Images of the different states: the sensor with Ab on top of activated layer of thiol-polyethylene glycol-carboxyl (a); (b) having a sensor with Buffer #1 added on Ab that is immobilized on an activated layer of thiol-polyethylene glycol-carboxyl, (c) having a sensor with Buffer #2 added on Ab that is immobilized on an activated layer of thiol-polyethylene glycol-carboxyl.

5.1.4. Raman Spectroscopy

Raman spectroscopy is a widely used technique for surface chemistry characterization. It provides valuable insights on a sample's chemical composition, molecular structure, and surface properties. Raman spectroscopy is based on the principle of inelastic scattering of photons, known as the Raman effect, which occurs when light interacts with the sample (Renate Petry Dr. & Popp, 2002) .

In Raman spectroscopy, a laser beam is focused onto the sample surface, and the scattered light is collected and analyzed. The majority of the scattered light has the same wavelength as the incident laser beam, known as the Rayleigh scattering, which does

not provide significant chemical information. However, a small fraction of the scattered light undergoes energy exchange with the sample, resulting in a shift in wavelength. These wavelength changes correlate to the sample molecules' vibrational modes, providing precise information on their chemical composition and bonding. (Rostron & Gerber, 2016).

Raman spectroscopy can be performed in two modes: confocal and non-confocal A pinhole is employed in the confocal mode to minimize scattered light from regions outside the focus point, resulting in better spatial resolution. This mode is beneficial for analyzing small areas or thin films with high precision. In the non-confocal mode, the scattered light is collected without spatial filtering, allowing for the analysis of larger sample areas (Webster et al., 1998).

The Raman spectrum obtained from the analysis contains a series of peaks corresponding to the sample molecules' vibrational modes. Each peak indicates a distinct group or molecular bond, allowing the identification and characterization of the chemical species present on the surface. The peak intensity and position provide information about the phase transitions, crystallinity, molecular structure, and chemical interactions.

Raman spectroscopy is a non-destructive and non-contact technique, making it suitable for analyzing delicate or sensitive samples. It can be applied to a wide range of materials, including metals, semiconductors, polymers, biological samples, and thin films. It is particularly helpful in studying interfaces, surfaces, and nanostructured materials, where properties can dramatically change from the bulk (Croudace & Rothwell, 2015).

This approach is very effective for analyzing functional groups with high Raman scattering, such as -OH, -NH, and -C=O. It may also be used to identify minerals and polymers, as well as detect impurities and faults in materials.

To summarize, Raman spectroscopy is a potent tool for surface chemistry characterization. It provides extensive molecular information regarding the composition, structure, and surface characteristics of a wide range of materials. Its non-destructive nature and high spatial resolution make it a valuable tool for studying materials surfaces and interfaces in various scientific and technological applications.
Raman Spectroscopy at 15 seconds acquisition:

1. Sensor with only COOH-PEG-SH on it (washed with DIW and dried)
2. Sensor with activated dry COOH-PEG-SH and SARS-CoV-2 mAb added to it, then quenched with ETA, washed with PBS, and dried.
3. Sensor with antibody added on top of our functionalized surface followed by buffer #1 addition, then washed with PBS and dried
4. Sensor with mAb dried step and added buffer 3, then washed with PBS and dried.

Drying is done in a vacuum chamber using negative pressure to dehydrate my samples for Raman Spectroscopy.

Two distinct ranges of Raman shift are displayed in figures 13, 14, and 15. The range on the right spans from 200 to 1400 rel.cm^{-1}, while the range on the left spans from 1000 to 2000 rel.cm^{-1}.

A total of three peaks were observed in Figure 20 for a sensor having dried thiol-polyethylene glycol-carboxymethyl added on top of the gold quartz crystal surface. The first peak located at approximately 383-670 rel.cm^{-1}, corresponds to the

presence of -C-S-O- presence (recall Figure 4) (Guzman-Santiago et al., 2021). Another peak was identified in the range of 800-950 rel.cm^{-1} which corresponds to -C-O-C- (Figure 4) (*Raman Correlations.Pdf*, n.d.). Finally, a distinct peak was observed at around 1610-1740 rel.cm-1, providing evidence for the presence of a carboxylic acid group (*Raman Correlations.Pdf*, n.d.).

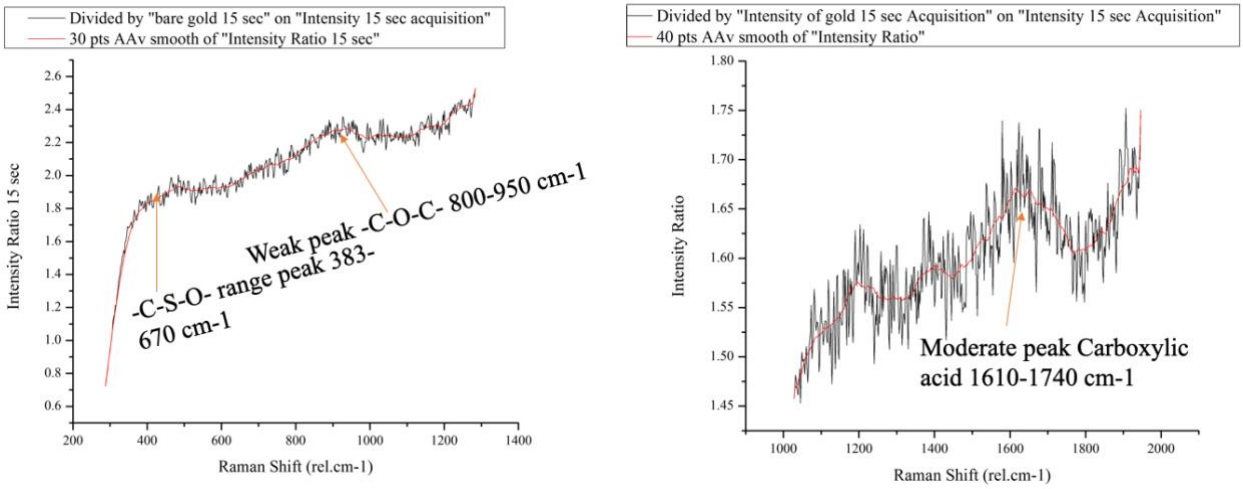

Figure 20 Raman Spectroscopy of a washed and dried having only a COOH-PEG-SH layer.

Figure 21 similarly showed three distant peaks for a dried sensor having COOH-PEG-SH activated using EDC/NHS and bond to SARS-CoV-2 N mAb. However, the difference was observed in the third peak, where instead of the carboxylic acid group, an amide group was detected at approximately 1653 rel.cm^{-1} (Maiti et al., 2004) (*Raman*

Correlations.Pdf, n.d.).

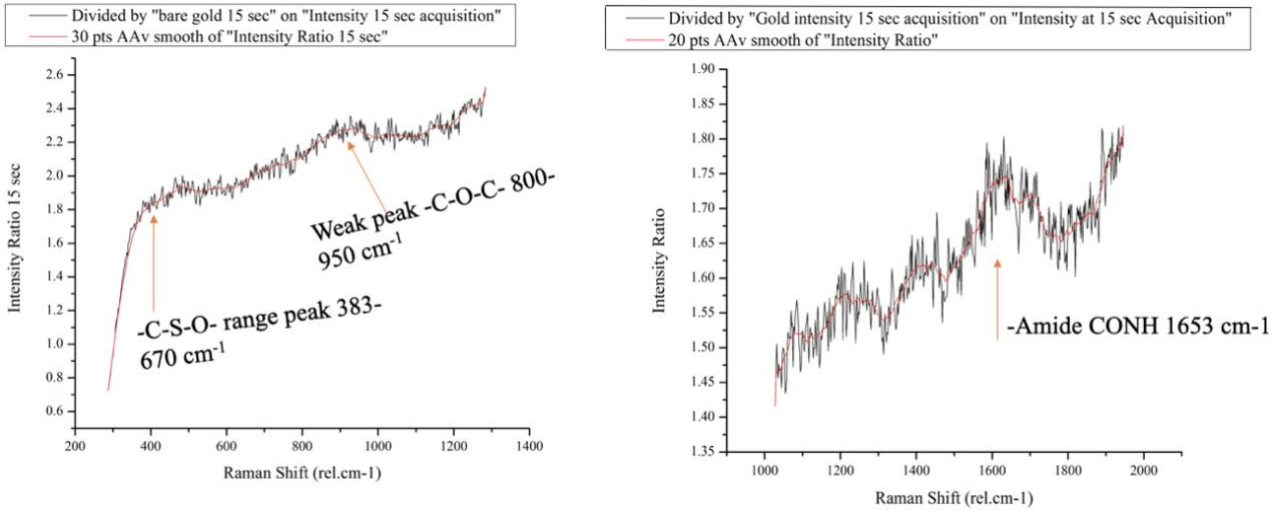

Figure 21 Raman Spectroscopy of a washed and Dried sensor having SARS-CoV-2 N mAb immobilized on a functionalized activated COOH-PEG-SH layer.

Figure 22 illustrates 3 distinct sensors :

- A dried sensor having COOH-PEG-SH activated using EDC/NHS and bond to SARS-CoV-2 N mAb (represented as f-mAb on the graph)
- A dried sensor having buffer #1 added on top of SARS-CoV-2 N mAb bonded to activated COOH-PEG-SH using EDC/NHS (represented as Buffer 1 on the graph)
- A dried sensor having buffer #2 added on top of SARS-CoV-2 N mAb bonded to activated COOH-PEG-SH using EDC/NHS (represented as Buffer 2 on the graph)

The three sensors exhibited identical peak locations as depicted in Figure 22, particularly with an overlap observed in the first two peaks within the Raman shift range of 200 to 1400 rel.cm^{-1}. However, in the Raman shift range of 1000 to 2000 rel.cm^{-1}, the f-mAb and buffer 1 displayed a similar curve shape for the amide bond at

1653 rel.cm^{-1}. On the other hand, buffer 2 exhibited a different curve shape at 1653 rel.cm^{-1}.

In summary, the analysis conducted using Raman spectroscopy has also proven that neither buffer #1 and buffer #2 disrupted the integrity of our functionalized surface (COOH-PEG-SH) or to the attachment of SARS-CoV-2 monoclonal antibody to our functionalized surface.

However, we decided to go for buffer #1 as the curve behavior was similar to that of f-mAb. In addition, buffer #1 has been used in many studies for lysing SARS-CoV-2, and has been found to be efficient (Raziq et al., 2021).

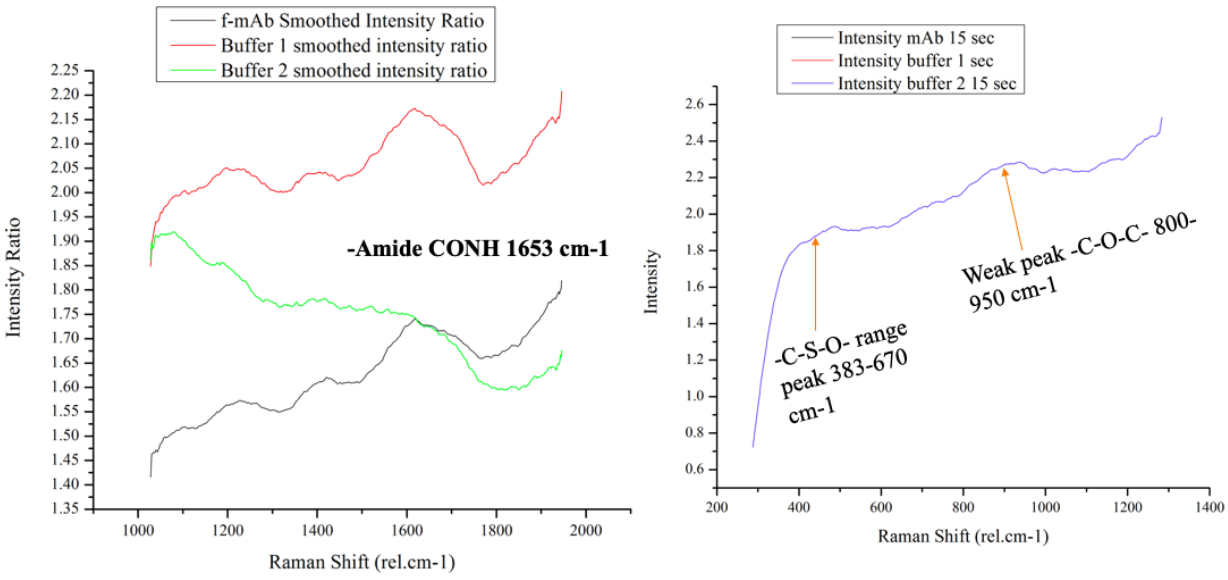

Figure 22 Comparing 3 different sensors Raman Spectroscopy results: First is a dried sensor having COOH-PEG-SH activated using EDC/NHS and bond to SARS-CoV-2 N mAb (represented as f-mAb on the graph); second is a dried sensor having buffer #1 added on top of SARS-CoV-2 N mAb bonded to activated COOH-PEG-SH using EDC/NHS (represented as Buffer 1 on the graph); third is a dried sensor having buffer #2 added on top of SARS-CoV-2 N mAb bonded to activated COOH-PEG-SH using EDC/NHS (represented as Buffer 2 on the graph).

5.2. TSM Assay Sensitivity

By conducting separate tests using varying concentrations of Bovine Serum Albumin (BSA) in phosphate buffer saline solution (PBS) and various concentrations of SARS-Related Coronavirus 2, Isolate USA-WA1/2020 in PBS, sensitivity can be estimated providing therefor insights into the performance of our developed immunosensor.

Sensitivity refers to the ability of the sensor to detect the target protein at a given concentration. To calculate the sensitivity of our immunosensor, we measured the frequency response of the sensor to different protein concentrations, and then plot a calibration curve relating the sensor's change in frequency response to the concentration of the target analyte.

Sensitivity in biosensors can be quantified by the slope of the calibration curve. The calibration curve is a plot of the sensor response (such as signal intensity or output voltage) against the concentration of the target analyte. By analyzing the slope of this curve, one can determine the sensitivity of the biosensor. The sensitivity of a biosensor is essentially the change in sensor response per unit change in analyte concentration. It provides a quantitative measure of how responsive the biosensor is to variations in analyte concentration. A steeper slope indicates higher sensitivity, meaning that even small changes in analyte concentration result in significant changes in the sensor response.

A calibration curve for a piezoelectric sensor is a graphical representation that illustrates the relationship between the sensor's frequency change response versus the concentration or amount of the analyte or target substance being detected. The calibration curve is constructed by measuring the sensor's response at different known concentrations or levels of the analyte and plotting these values graphically. The resulting curve allows for the determination of the analyte concentration in an unknown sample by comparing its sensor response to the calibration curve. The calibration curve serves as a reference or standard against which future measurements can be compared, providing a quantitative correlation between the sensor's output signal and the analyte concentration.

5.2.1. Device Sensitivity Testing using a series of BSA concentrations over a Bare Gold Quartz Sensor

A series of BSA concentrations are added incrementally on a bare gold electrode surface of the quartz crystal, that was initially wetted with phosphate buffer saline (PBS) solution (Table 3). Frequency reading of each BSA concentration is taken for a duration of 5 minutes and averaged. A calibration curve was thus constructed as we plotted the frequency in response to each corresponding concentration of BSA measured using Novatech OpenQCM Wi2. A linear regression was generated by taking the logarithmic values of the averaged change in frequencies vs logarithmic values of the various concentrations picked for the device sensitivity test (Figure 23). The coefficient of determination (R^2) was found to be 0.9479.

The relationship is illustrated in the below equation:

$$(6)\ \mathrm{Y} = 0.2044 \times \mathrm{X} + 0.6143, \text{with } \mathrm{X} = \mathrm{Log}(\mathrm{X}) \text{and } \mathrm{Y} = \mathrm{Log}(\mathrm{Y}).$$

Concentration (pg/mL)	Averaged Change in Frequency (Hz)	Standard Deviation
0	0	0
10	6.02	8.329718
100	12.58925	9.673221
1000	15.84893	50.00889
10000	29.40503	8.017609
50000	30.64	6.858936
100000	60.59847	33.72232

500000	46.62	14.75025
1000000	55.5	22.52842
10000000	140.0818	102.2092

Table 3 Averaged Frequency estimated for each of BSA concentration recorded through OpenQCM Wi2

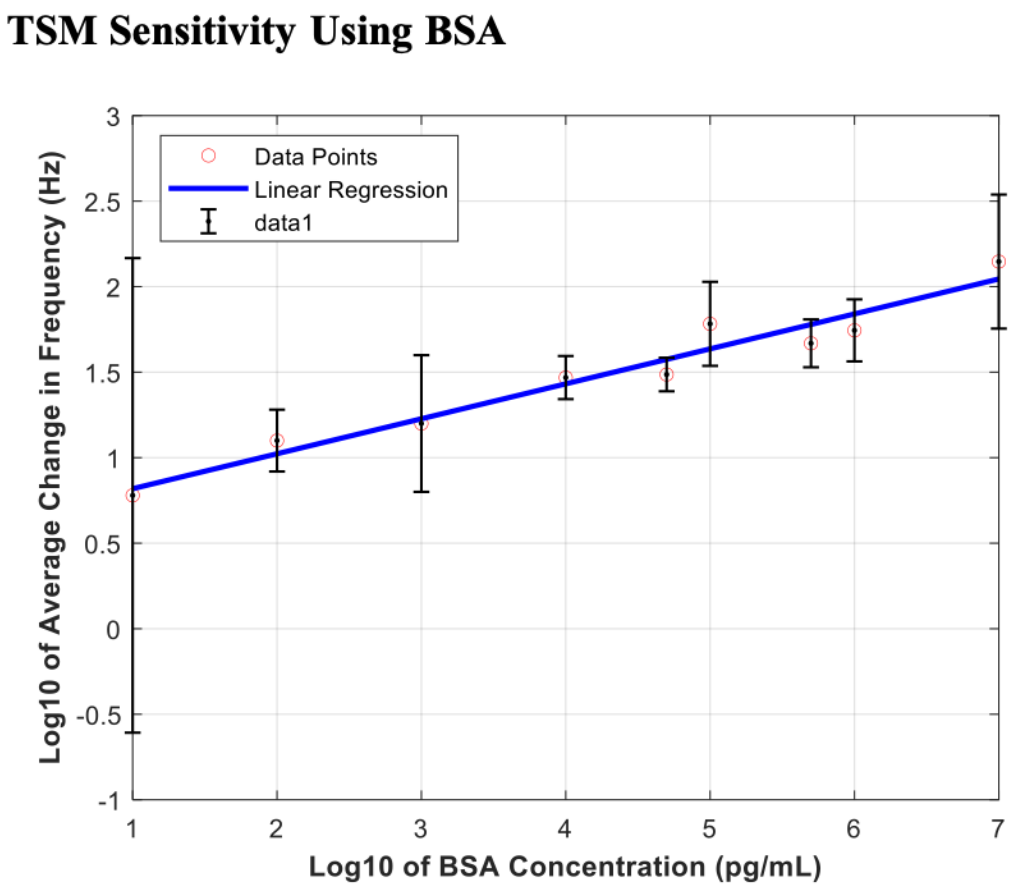

Figure 23 Linear regression generated by taking the logarithmic of averaged change in frequencies (Hz) vs logarithmic values of the various concentrations picked for the device sensitivity test

Based on the equation generated, we can now determine the sensitivity, which is the slope that is 0.2044.

5.2.3. Device Sensitivity Testing Using a Series of SARS-CoV-2 Concentrations over a Fully Functionalized Surface

Similarly, a sensitivity test was performed using a series of SARS-Related Coronavirus 2, Isolate USA-WA1/2020 concentrations over our functionalized surface, described in the methodology section. In this context of diagnosis, a series of dilutions were performed on our lysed heat-inactivated SARS-CoV-2, starting first with its concentration obtained after lysing the viral inactivated sample, which is 5.33×10^4 $TCID_{50}$/mL (Appendix 4). Then performing 10 folds of dilution on our lysed heat-inactivated SARS-CoV-2 samples. An additional concentration was added, which is 2.665×10^2 $TCID_{50}$/mL, which was a 2 folds dilution to the 5.33×10^2 $TCID_{50}$/mL (refer to Table 4).

The same chosen concentrations of SARS-CoV-2 studied for our QCM were ran on RT-PCR, and CT values were obtained accordingly to each of the chosen concentrations (Table 4).

In parallel, a vehicle control (negative control) is performed using distilled water (DIW) and PBS to simulate all the stages of our experiment and was repeated 3 times, to ensure the reliability and validity of the study (Appendix 3). The vehicle control experiment involves using an inert substance or a neutral medium, such as distilled water or PBS, that closely mimics the experimental conditions but lacks the presence of the virus itself. It provides a baseline or reference point against which the results obtained with the virus-infected samples can be compared. This control helps ensure

that any observed effects are indeed due to the presence of the virus and not a result of experimental artifacts or the medium used.

To note, $TCID_{50}$/mL stands for Tissue Culture Infectious Dose 50 per milliliter. It is a measurement used to quantify the infectivity or viral titer of a virus in a sample. $TCID_{50}$ value represents the dilution at which 50% of the tissue cultures or cells are infected by the virus. It is typically determined by conducting a series of dilutions of the sample and observing the cytopathic effects (CPE) or presence of viral growth in the tissue culture or cell lines. (Lei et al., 2021)

PFU/mL stands for Plaque-Forming Units per milliliter. It is another measurement used to quantify the infectivity or viral titer of a virus in a sample. The PFU/mL value indicates the number of viral particles with the ability to generate visible plaques, which are distinct regions of infected cells, on a layer of susceptible cells. The measurement of PFU/mL offers insights into the quantity of viable infectious particles contained within the sample. (Bhatt et al., 2022)

Both TCID50/mL and PFU/mL are units commonly used in virology and viral studies to evaluate the infectious viral particles' concentration in a sample. These units are effective in assessing the infectivity of a virus, estimating a viral test's efficiency (like in this case), and studying viral replication and pathogenesis.

Concentration of lysed heat-inactivated SARS-CoV-2 ($TCID_{50}$/mL)	Average Change in Frequency (Hz)	Standard Deviation	CT values obtained by RT-PCR
5.33×10^4 $TCID_{50}$/mL	1766.69748701385	122.929802928109	30.48
5.33×10^3 $TCID_{50}$/mL	1536.8641522713	107.116264474016	28.35

5.33×10^2 $TCID_{50}$/mL	158.278566666667	74.3616472268692	27.45
2.665×10^2 $TCID_{50}$/mL	136.205578890319	43.4799507224036	23.87
5.33×10^1 $TCID_{50}$/mL	80.2627666666667	12.6132968181731	20.86

Table 3 Average change in frequency (Hz) in terms of concentration of lysed heat-inactivated SARS-CoV-2 and CT values obtained by running RT-PCR test on our SARS-CoV-2 samples' concentrations.

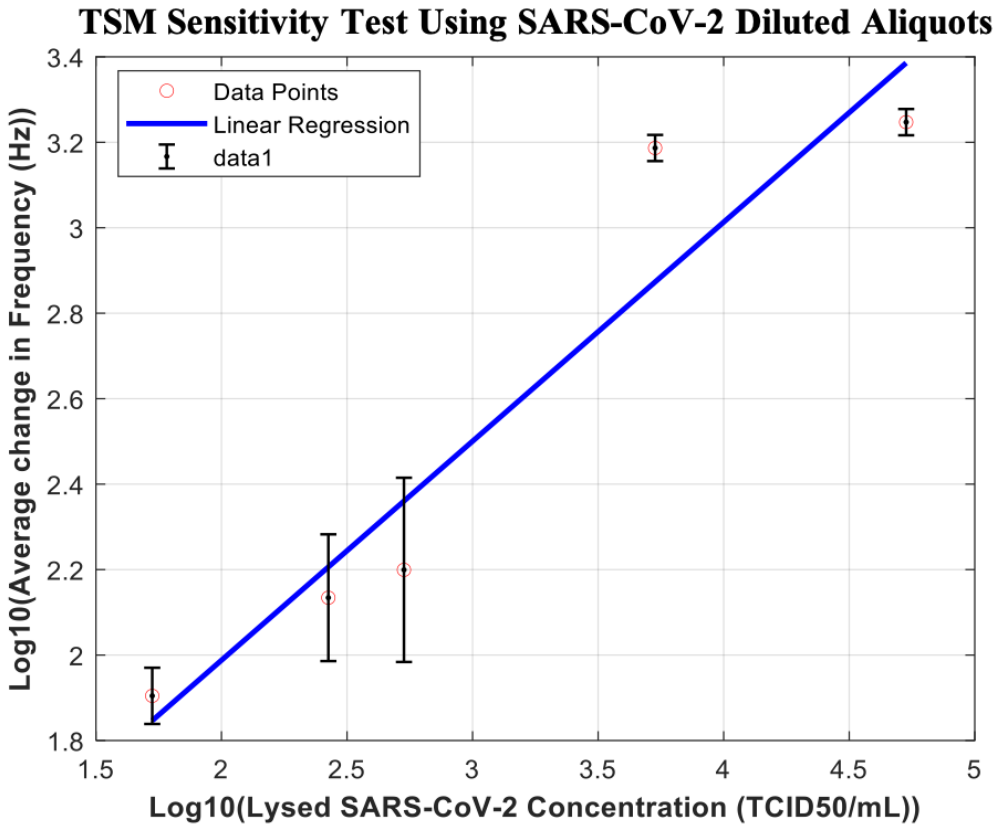

Figure 24 Calibration curve of Log10 of Average Δf (Hz) of all Replicates vs. Log10 of SARS-CoV-2 Inactivated Virus Concentrations.

A linear regression was also generated here by taking the logarithmic values of the averaged change in frequencies vs logarithmic values of the various concentrations

picked for the device sensitivity test (Figure 24). The coefficient of determination (R^2) was found to be 0.9053. The equation of the regression line of Figure 24:

$$(7)\ [\text{Log}(Y)] = 0.5130*[\text{Log}(X)] + 0.9614$$

$$R^2 = 0.9053$$

Sensitivity is as previously mentioned the slope of the linear regression, which is in this case, 0.5130. 1/slope is 1.949.

5.3. Limit of Detection (LoD)

The limit of detection (LoD) is a crucial parameter for antigen tests used in the detection of SARS-Related Coronavirus 2, Isolate USA-WA1/2020, the virus responsible for COVID-19. The LoD represents the lowest concentration or amount of the viral antigen that can be reliably detected by the test. It represents the threshold below which the presence of the antigen may not be reliably detected, leading to a false negative result. (*Understanding Cycle Threshold (Ct) in SARS-CoV-2 RT-PCR*, 2020)

Achieving a low LoD is essential to ensure the sensitivity and accuracy of the antigen test in identifying individuals who are infected with the virus, particularly in the early stages of infection when viral antigen levels may be lower. Efforts are continuously being made to improve the LoD of SARS-CoV-2 antigen tests through advancements in assay technology, sample collection methods, and reagent formulation. Lowering the LoD allows for the detection of even trace amounts of the viral antigen, aiding in the timely identification and control of COVID-19 cases to mitigate the spread of the disease.

A significance test was conducted and are shown in details in Appendix 4, and are illustrated in this figure as asteroid (*****) for significant, and it was found that 5.33 x

10^3 $TCID_{50}$/mL is the lowest concentration showing significance in comparison with the negative control (Figure 25). Therefore, our label-free functionalized gold sensor achieved a limit of detection (LoD) of 5.33 x 10^3 $TCID_{50}$/mL, which shows a limit of detection in the thousands range similar to a study done in 2021 by Forinová et al. on a piezoelectric immunosensor for SARS-CoV-2 N detection having a LoD of 9.1 × 10^3 TCID50/mL and Abnova test (refer to Table 5).

To further ensure the LoD of our assay, more concentrations can be studied and added, especially in the range between 5.33 x 10^2 and 5.33 x 10^3 $TCID_{50}$/mL.

Antigen Tests	LoD ($TCID_{50}$/mL)
Abnova SARS-CoV-2 Viral Antigen Rapid Test	8 x 10^3 (Abnova, n. d.)
La Roche SARS-CoV-2 Rapid Antigen Test	3.12 x $10^{2.2}$ (La Roche, n. d.)
Piezoelectric sensor (QCM) for SARS-CoV-2	1.3 × 10^4 PFU/mL=1.3 × 10^4 PFU/mL * 0.7 $TCID_{50}$/PFU = 9.1 × 10^3 TCID50/mL (Forinová et al., 2021). [1 PFU = 0.7 × $TCID_{50}$ (Furuya, 2020)]
Biomimetic label- free plasmonic sensor for SARS-CoV-2 Spike protein virus	630 and 200 for Delta and Omicron variants, respectively (Batool et al., 2023)

Table 4 Antigen tests and their LoDs.

Figure 25 presents a histogram that showcases the average change in frequency and the corresponding standard deviation for the vehicle control (DIW and PBS), as well as for each concentration of our lysed heat-inactivated SARS-CoV-2 virus sample. The histogram was generated by conducting a series of dilutions on the virus using PBS, as described in Table 4. To ensure the accuracy and reliability of the results, we

performed three replicates for both the vehicle control and each selected SARS-CoV-2 concentration. A significance test was conducted and are shown in details in Appendix 4, and are illustrated in this figure as asteroids for significant.

Figure 26 presents a histogram that represents the average change in frequency and the corresponding standard deviation for the vehicle control (DIW and PBS), as well as the CT (cycle threshold) value generated for each concentration of our studied lysed heat-inactivated SARS-CoV-2 virus sample.

It is worth noting that our system can be unstable and is prone to drift due to mechanical perturbations and noises, along with the change in temperature, and humidity. Ensuring a noise-free environment and controlled temperature can enhance the performance of our assay.

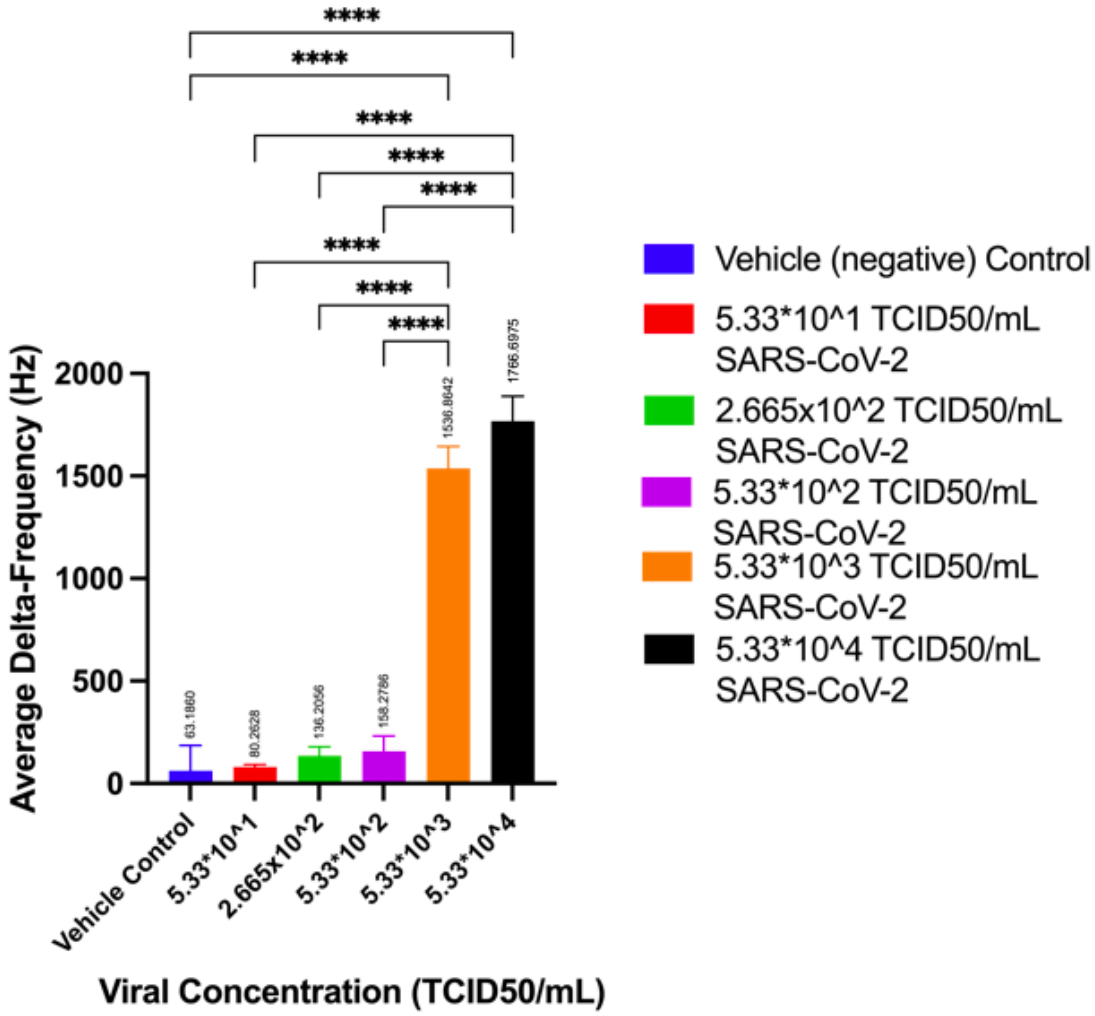

Figure 25 Summary of Average Change in Frequency (Hz) vs. the different concentrations of SARS-CoV-2 inactivated virus (TCID50/mL) and the vehicle control (PBS-DIW). Error bars are generated based on performing 3 replicates for each viral concentration and for the negative (vehicle control).

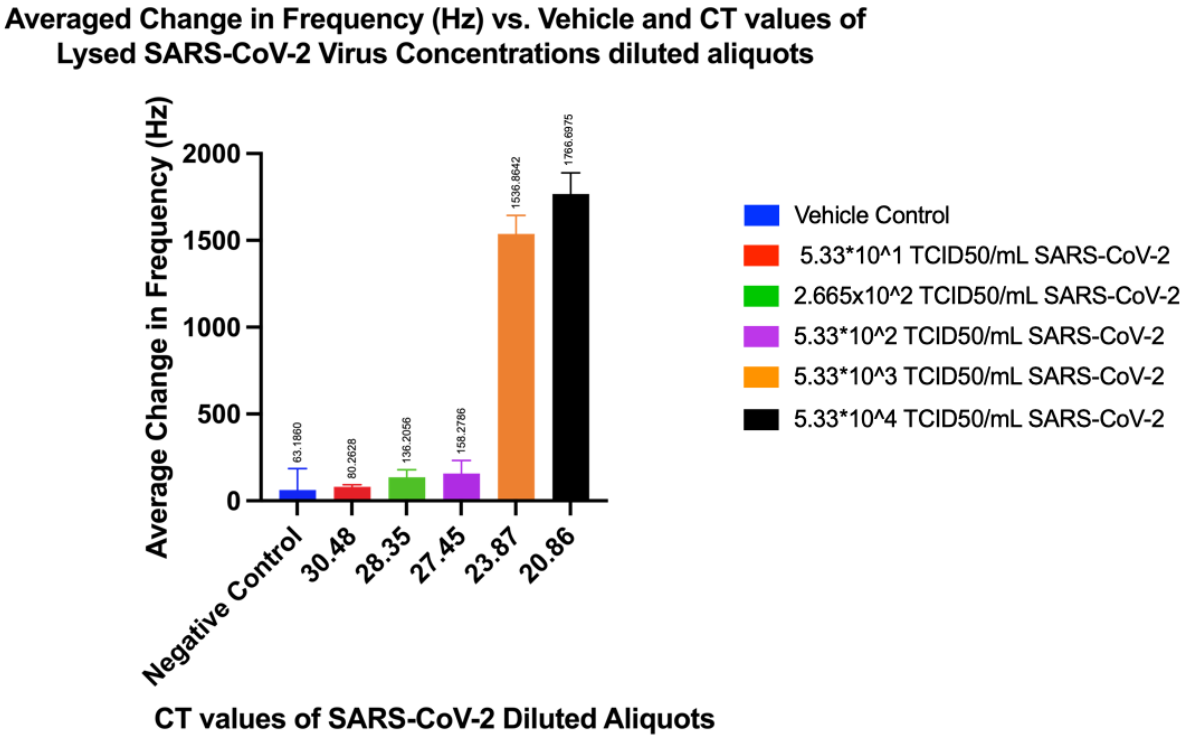

Figure 26 Summary of average change in frequency (Hz) vs. vehicle control and RT-PCR's CT values of the same diluted aliquots of SARS-CoV-2 heat-inactivated virus concentrations ran on QCM

5.4. Cross-Reactivity Test

The cross-reactivity test for rapid SARS-CoV-2 piezoelectric diagnosis consists of measuring the binding and frequency change of the sensor in response to potential cross-reacting pathogens or substances caused by the interaction with the diagnostic device's surface chemistry.

In the context of diagnostics, cross-reactivity testing helps determine if a test can distinguish between the target of interest and other similar pathogens. Binding is assessed by measuring the signal response of the sensor, while frequency change is measured by analyzing the change in resonance frequency of the quartz crystal in the sensor. It involves evaluating whether an antibody (SARS-CoV-2 N mAb) or other

specific binding agent can recognize and bind to related but distinct target molecules (Influenza A).

The results of cross-reactivity testing are essential for determining the specificity of a diagnostic test. Specificity refers to the ability of a test to accurately identify only the target of interest and not produce false-positive results due to cross-reactivity with unrelated substances. A highly specific test demonstrates minimal or no cross-reactivity, meaning it can reliably detect and distinguish the target from other substances. Conversely, a test with significant cross-reactivity may yield false-positive or indeterminate results, leading to reduced specificity.

Thus, this test aims to assess whether the piezoelectric-based diagnostic device for SARS-CoV-2 diagnosis exhibits cross-reactivity with similar viruses or common respiratory pathogens, in our case like Influenza type A, which could lead to inaccurate results.

A heat inactivated Influenza type-A viral sample NR-52286 (BEI RESOURCES) with an initial concentration of 62.5×10^6 PFU/mL is used for the cross-reactivity test for our developed SARS-CoV-2 immunosensor. 1 PFU is 0.7 $TCID_{50}$ (Furuya, 2020). Thus, multiplying by the conversion factor of 0.7, the initial concentration in $TCID_{50}$ would be 4.375×10^7 $TCID_{50}$/mL. The inactivated Influenza A is lysed using our chosen lysis buffer (final pH of 7.2), as previously mentioned, it is made of and stored at 4°C (Raziq et al., 2021):

- 1.5 % (v/v) Triton X-100
- 27.5 mM Tris-HCl
- 0.1% SDS
- 12.5 mM EDTA

After performing a 1:3 dilution on the inactivated virus using our lysis buffer, 2.97 x 10^7 TCID50/mL of lysed Influenza A inactivated virus was heated at 56°C for 30 minutes.

A comprehensive cross-reactivity testing is important to ensure the reliability and specificity of piezoelectric-based diagnostic devices for detecting SARS-CoV-2 nucleocapsid antigen.

Henceforth to perform the cross-reactivity test, we performed the surface functionalization steps depicted in Figure 27 with the Influenza antigen being added at the end instead of SARS-CoV-2 nucleocapsid antigen. Influenza antigen should not be binding on SARS-CoV-2 N mAb, as the antibody should only be selective to the nucleocapsid protein of SARS-CoV-2 antigen N. The test was conducted two additional times to further emphasize the result (Appendix 5).

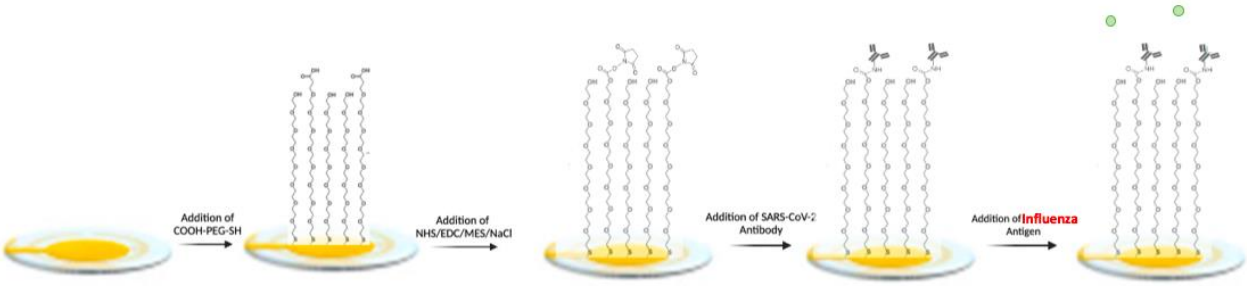

Figure 27 Influenza antigen addition over our functionalized surface

Figure 28 showed clearly that the change in frequency of the frequency after washing the Influenza antigen away on the surface compared to the frequency after washing the excess of Ab on the surface is negative. This means that the frequency after washing the Influenza antigen away on the surface went higher than the frequency level after washing the excess of SARS-CoV-2 antibody by 194.277333 in average. It is

worth nothing that the standard deviation for the cross-reactivity test for the three replicates experiments of Influenza A is of 107.448587.

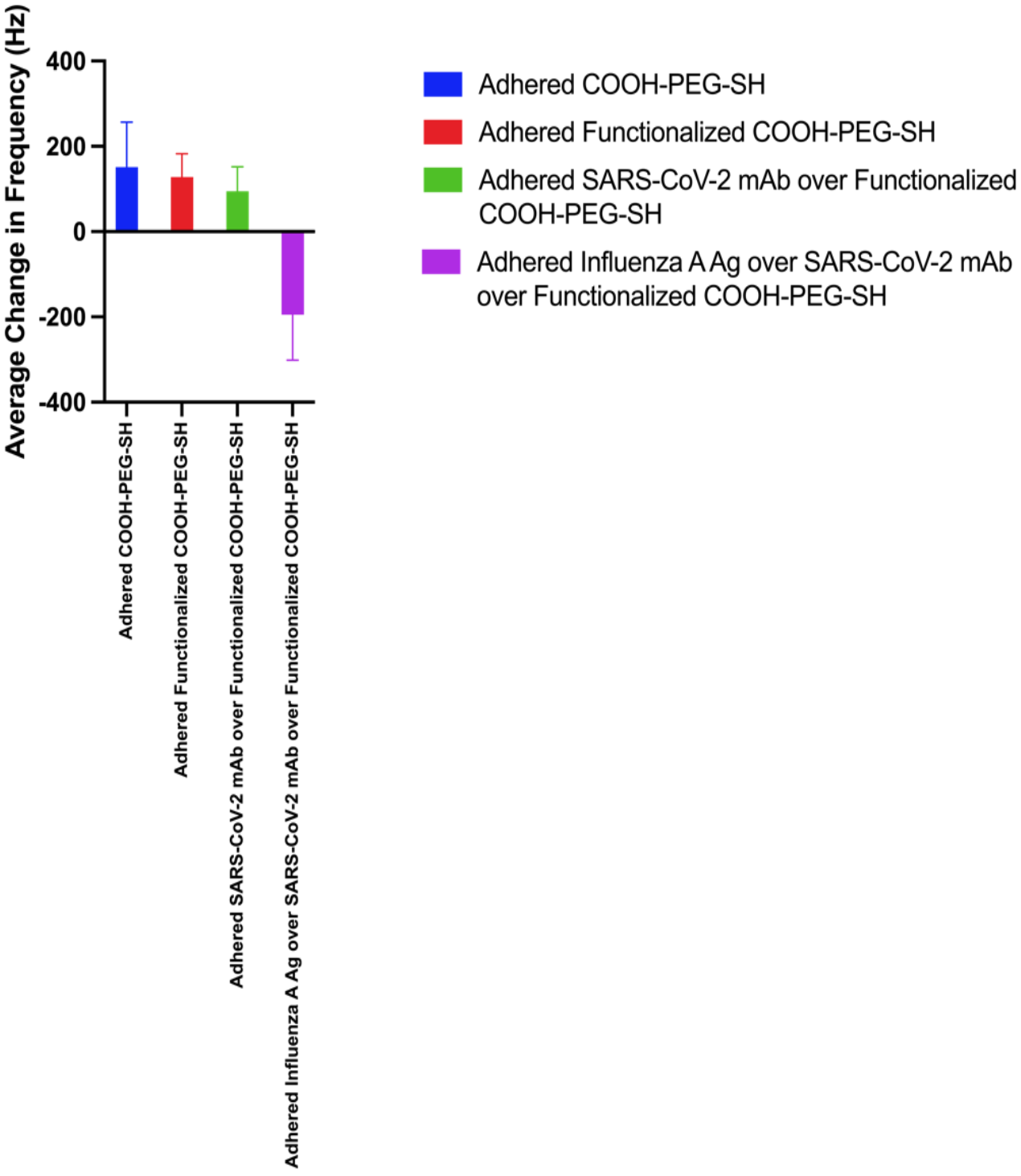
Average Change in Frequency (Hz)
400
200
0
-200
-400
Adhered COOH-PEG-SH
Adhered Functionalized COOH-PEG-SH
Adhered SARS-CoV-2 mAb over Functionalized COOH-PEG-SH
Adhered Influenza A Ag over SARS-CoV-2 mAb over Functionalized COOH-PEG-SH
Adhered COOH-PEG-SH
Adhered Functionalized COOH-PEG-SH
Adhered SARS-CoV-2 mAb over Functionalized COOH-PEG-SH
Adhered Influenza A Ag over SARS-CoV-2 mAb over Functionalized COOH-PEG-SH

Figure 28 Average Δf (Hz) for the case of 2.97 x 10^7 TCID50/mL lysed Influenza A inactivated virus

Figure 29 illustrates the frequency at the end of the three replicate experiments, after washing excess Influenza on the surface, no Influenza A antigen was seen to be bind on SARS-CoV-2 N mAb. The developed immunosensor is thus specific for SARS-CoV-2 nucleocapsid antigen. Each series in the plot represent a replicate of lysed Influenza A inactivated virus with a concentration of 2.97 x 10^7 $TCID_{50}$/mL.

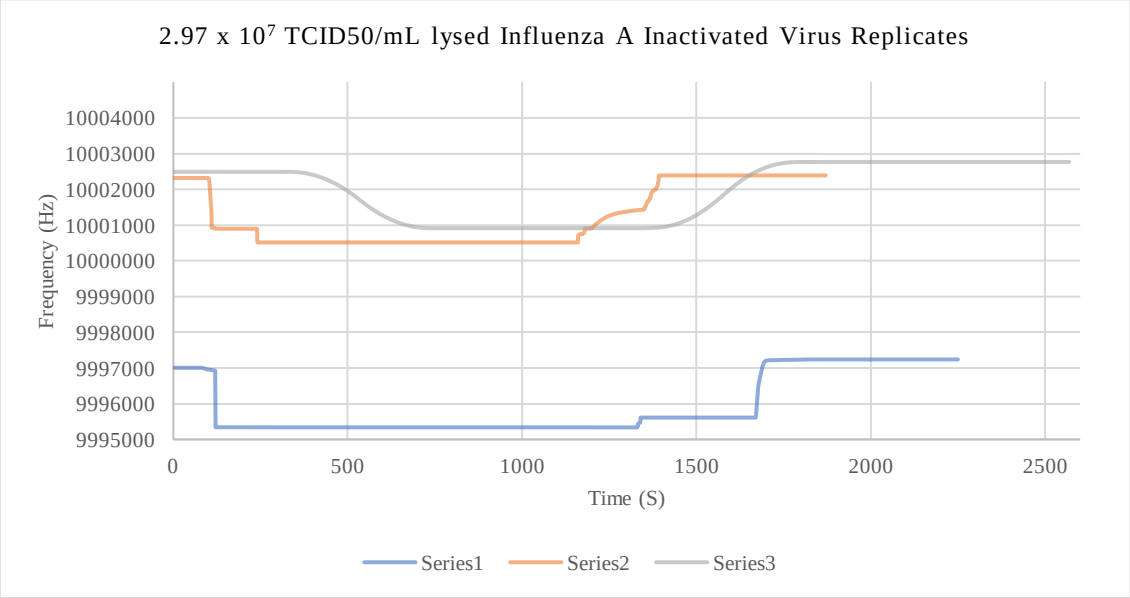

Figure 29 Normalized plot during the final stages of the experiment, including the addition of the lysed inactivated virus, subsequent washing step, and drying process. Each series in the plot represents a replicate of lysed Influenza A inactivated virus with a concentration of 2.97 x 10^7 $TCID_{50}$/mL.

Hence, our sensor demonstrated not only good sensitivity but also good specificity for SARS-CoV-2 as no cross-reaction or interference was detected with the potentially cross-reacting microorganism, Influenza A.

Testing cross-reactivity is important for COVID-19 detection for several reasons. Cross-reactivity testing helps evaluate the specificity of the COVID-19 detection assay or test. It ensures that the test accurately detects the presence of SARS-CoV-2, the virus causing COVID-19, without producing false-positive results due to cross-reactivity with other related or unrelated antigens. Also, cross-reactivity testing allows differentiation between SARS-CoV-2 and other pathogens that may have similar clinical manifestations or circulating antigens. It helps confirm that the test specifically detects SARS-CoV-2 and does not yield false-positive results from other viruses or common respiratory infections. (Peto et al., 2021)

In addition, minimizing False-Positive Results: False-positive results can lead to unnecessary anxiety, additional testing, and potential disruptions in public health management. By assessing cross-reactivity, the risk of false-positive results can be minimized, ensuring that individuals are accurately diagnosed and appropriately managed. Also, cross-reactivity testing contributes to the accuracy of epidemiological data related to COVID-19. Reliable data on the prevalence and spread of SARS-CoV-2 are essential for effective public health interventions, resource allocation, and decision-making. (Greenhawt et al., 2021)

Also, cross-reactivity testing is crucial for assessing the specificity of COVID-19 vaccines. It helps determine whether vaccine-induced antibodies produce false-positive results in diagnostic tests, potentially impacting the interpretation of test results in vaccinated individuals.

Finally, with the emergence of new SARS-CoV-2 variants, cross-reactivity testing is necessary to evaluate the performance of diagnostic tests against these variants. It helps ensure that the tests can accurately detect the new variants and

maintain their specificity. Overall, testing cross-reactivity is an important step in validating the accuracy and reliability of COVID-19 detection assays. It helps ensure that the tests specifically target SARS-CoV-2, reducing the chances of false-positive results and providing confidence in the test's performance for accurate diagnosis and surveillance of COVID-19.(Thomas et al., 2021)

CHAPTER 6

CONCLUSION

This research work introduces a promising method for the rapid and sensitive detection of the SARS-CoV-2 virus, responsible for the Coronavirus Disease (COVID-19), utilizing a low-cost piezoelectric sensor based on Quartz Crystal Microbalance (QCM) technology. This is done by developing and successfully characterizing an immunosensor having SARS-CoV-2 monoclonal nucleocapsid mouse IgG2a antibody immobilized on a functionalized spread of COOH-PEG-SH layer over the gold surface electrode of the quartz crystal surface (Muthuswamy et al., 2022) (M. L. Khraiche et al., 2005).

Sensitivity and LoD of our assay were determined through a series of separate experiments of PBS dilutions of BSA and lysed SARS-CoV-2 virus using lysis buffer # 1 (the best buffer). RT-PCR was performed on the diluted SARS-CoV-2 aliquots ran by QCM to obtain their CT values. Finally, a cross-reactivity test was performed using a heat-inactivated Influenza-type A virus sample that was also lysed using the same lysis buffer and ensured the specificity of our immunosensor towards SARS-Related Coronavirus 2, Isolate USA-WA1/2020.

To ensure the reliability and robustness of the sensor's surface chemistry, various characterization techniques such as Digital Holographic Microscope (DHM), Fluorescence Microscopy, Scanning Electron Microscopy (SEM), Energy-Dispersive X-ray Spectroscopy (EDX), and Raman Spectroscopy were conducted. These analyses confirmed the effectiveness of the sensor surface coating in detecting the virus. For the first time, DHM imaging was performed to confirm quantitatively and qualitatively the presence of antibody immobilized on a functionalized surface through Sa.

The limit of detection (LoD) of the immunosensor was determined to be 5.33 x 10^3 TCID50/mL (CT value of 23.87), which is similar to the piezoelectric immunosensor for SARS-CoV-2 N detection (Forinová et al., 2021) with a LoD of 9.1 × 10^3 TCID50/mL. A cross-reactivity test using a heat-inactivated Influenza-type A virus sample confirmed the assay's ability to differentiate SARS-CoV-2 from other respiratory viruses, establishing its specificity.

This research presents a highly sensitive and specific assay for the detection of SARS-CoV-2 using a cost-effective label-free piezoelectric quantitative real-time monitoring sensor based on QCM technology, which sets it apart from qualitative antigen tests. The thorough characterization and sensitivity analyses conducted using various techniques validate the reliability and robustness of the sensor, while the specificity test confirms its ability to distinguish SARS-CoV-2 from other viruses.

It is important to note that the assay may exhibit some instability due to the sensitive nature of the QCM environment. Additionally, the surface chemistry process takes approximately 5 hours, and further modifications may be explored to expedite the procedure and develop a fast alternative for point-of-care antigen testing.

Future work may involve studying other SARS-CoV-2 variants and respiratory viruses to ensure specificity. Clinical samples should be tested on the immunosensor and compared with CT values obtained from RT-PCR.

In summary, this work demonstrates the potential of piezoelectric immunosensor in fighting the disease offering a label-free, easy to use, quantitative, affordable real-time monitoring method for SARS-CoV-2 nucleocapsid protein detection.

APPENDIX

APPENDIX 1: LIST OF FDA APPROVED ANTIGEN TEST KITS FOR COMMERCIAL USE (*FDA Advisory No.2021-2094 || List of COVID-19 Test Kits with FDA Special Certification and Performance Validation Conducted and/or Recommended by the Research Institute for Tropical Medicine (RITM) - Food and Drug Administration*, 2021):

Product Name	**Name & Address of Manufacturer**	**Name of Importer/ Distributor**	**Specimen**	**RITM Validated Result Sensitivity**	**RITM Validated Result Specificity**
PanbioTM COVID-19 Ag Rapid Test Device	Abbot Rapid Diagnostics Jena GmbH	Sunfu Solutions Inc.	Nasopharyngeal Swab	CT < 30 (97.83%)	100%
PanbioTM COVID-19 Ag Rapid Test Device	Abbot Diagnostics Korea Inc.	Sunfu Solutions Inc.	Nasopharyngeal Swab	CT < 30 (97.83%)	100%
SOFIA 2 SARS Antigen FIA	Quidel Corporation	LABx CORP.	Nasopharyngeal /Nasal Swab	CT < 30 (92.86%)	100%
PanbioTM COVID-19 Ag Rapid Test Device	Abbott Rapid Diagnostics Jena GmbH	Allied Hospital Supply International Corp	Nasopharyngeal swab	CT < 30 (97.83%)	100%
STANDARD™ Q COVID-19 Ag TEST KIT	SD Biosensor, Inc	Trulaboratories Corporation	Nasopharyngeal swab	CT<30 (93.1%)	100%
PanbioTM COVID-19 Ag Rapid Test Device	Abbott Rapid Diagnostics Jena GmbH	Allied Hospital Supply International Corp.	Nasal swab	CT < 30 (90.5%)	99.20%
NowCheck COVID-19 Antigen Test	BioNote Inc	Biologic Life Sciences Corp.	Nasopharyngeal swab	CT < 30 (91.4%)	97.30%
Novel Coronavirus (2019-nCoV) Antigen Detection Kit (Colloidal Gold Method) // Wondfo 2019-nCoV Antigen	Guangzhou Wondfo Biotech Co., - Guangzhou Wondfo Biotech Co., Ltd.	Tradematchers, Inc.	Nasopharyngeal or Oropharyngeal swabs	CT < 30 (92.2%)	100%

Test (Lateral flow)					
Novel Coronavirus (2019-nCoV) Antigen Detection Kit (Colloidal Gold Method) // Wondfo 2019-nCoV Antigen Test (Lateral flow)	Guangzhou Wondfo Biotech Co., - Guangzhou Wondfo Biotech Co., Ltd.	LabSolution Technologies Inc	Nasopharyngeal or Oropharyngeal swabs	CT < 30 (92.2%)	100%
Novel Coronavirus (2019-nCoV) Antigen Detection Kit (Colloidal Gold Method) // Wondfo 2019-nCoV Antigen Test (Lateral flow)	Guangzhou Wondfo Biotech Co., - Guangzhou Wondfo Biotech Co., Ltd.	Alcheon Medical Corporation	Nasopharyngeal or Oropharyngeal swabs	CT < 30 (92.2%)	100%

APPENDIX 2: 2022 EUA-FDA APPROVED QUALITATIVE ANTIGEN TESTS FDA (SENSITIVITIES, AND LOD) (*In Vitro Diagnostics EUAs - Antigen Diagnostic Tests for SARS-CoV-2 | FDA*, n.d.)

Name of Test	Manufacturer	Sensitivity	Specificity	Specimens needed for the test	Target genes	Limit of detection (LoD)
BD Veritor System for Rapid Detection of SARS-CoV-2	Becton, Dickinson and Company (BD)	84% (symptomatic)	100% (symptomatic)	nasal swabs	Nucleocapsid protein	140 TCID50/mL
VITROS Immunodiagnostic Products SARS-CoV-2 Antigen Reagent Pack	OrthoClinical Diagnostics	80.00%	100%	nasopharyngeal swab	Nucleocapsid protein	500-1500 TCID50/mL
GenBody COVID-19 Ag	GenBody Inc.	91.10%	100%	nasopharyngeal swabs	nucleocapsid protein	1.11 x 10^2 TCID50/mL
InteliSwab COVID-19 Rapid Test Rx	OraSure Technologies, Inc.	84.0%	98.0%	anterior nasal swabs	nucleocapsid protein	2.5 x 10^2 TCID50/mL
InteliSwab COVID-19 Rapid Test	OraSure Technologies, Inc.	84.0%	98.0%	anterior nasal swabs	nucleocapsid protein	2.5 x 10^2 TCID50/mL
InteliSwab COVID-19 Rapid Test Pro	OraSure Technologies, Inc.	84.0%	98.0%	anterior nasal swabs	nucleocapsid protein	2.5 x 10^2 TCID50/mL
Sienna-Clarity COVID-19 Antigen Rapid Test Cassette	Salofa Oy	87.5%	98.9%	nasopharyngeal swab	Nucleocapsid protein	1.25 x 10^3 TCID50/mL
SCoV-2 Ag Detect Rapid Test	InBios International, Inc.	86.6%	100%	anterior nasal swab	Nucleocapsid protein	6.3x10^3 TCID50/mL
Celltrion DiaTrust COVID-19 Ag Rapid Test	Celltrion USA, Inc.	93.3%	99.0%	nasopharyngeal swabs	Nucleocapsid protein and spike RBD	3.2 × 10^1 TCID50/mL
Omnia SARS-CoV-2 Antigen Test	Qorvo Biotechnologies, LLC.	90%	100%	anterior nasal swab	Nucleocapsid protein	125,000 genome equivalents/mL
Sofia SARS Antigen FIA	Quidel Corporation	97%	100%	nasopharyngeal and nasal swabs	Nucleocapsid protein	226 TCID50/mL
QuickVue At-Home OTC COVID-19 Test	Quidel Corporation	83.50%	99.20%	anterior nasal swab	nucleocapsid protein	19100 TCID50/mL
BinaxNOW COVID-19 Antigen Self Test	Abbott Diagnostics Scarborough, Inc.	91.7% (symptomatic)	100% (symptomatic)	anterior nasal swab	nucleocapsid protein	140.6 TCID50/mL
BinaxNOW COVID-19 Ag Card 2 Home Test	Abbott Diagnostics Scarborough, Inc.	91.7% (symptomatic)	100% (symptomatic)	anterior nasal swab	nucleocapsid protein	140.6 TCID50/mL
BinaxNOW COVID-19 Ag Card Home Test	Abbott Diagnostics Scarborough, Inc.	91.7% (symptomatic)	100% (symptomatic)	direct anterior nasal (nares) swab samples	Nucleocapsid protein	140.6 TCID50/mL
BinaxNOW COVID-19 Ag Card	Abbott Diagnostics Scarborough, Inc.	84.6%	98.5%	nasal swabs	Nucleocapsid protein	22.5 TCID50/swab
BinaxNOW COVID-19 Ag 2 Card	Abbott Diagnostics Scarborough, Inc.	84.6% (symptomatic)	98.5% (symptomatic)	anterior nasal swab	nucleocapsid protein	140.6 TCID50/mL
BD Veritor System for Rapid Detection of SARS-CoV-2 & Flu A+B	Becton, Dickinson and Company	87.6% (SARS-CoV-2) 100% (Flu A+B)	99.5% (SARS-CoV-2) 100% (Flu A+B)	anterior nasal swab	nucleocapsid protein	2.8x10^2 TCID50/mL (SARS-CoV-2) 1.0x10^8 TCID50/mL (Flu A) 1.0x10^10 TCID50/mL (Flu B)
QuickVue At-Home COVID-19 Test	Quidel Corporation	84.8%	99.1%	anterior nares swabs	nucleocapsid protein	9.55 x 10^4 TCID50/mL
Status COVID-19/Flu A&B	Princeton BioMeditech Corp.	93.9% (SARS-CoV-2) 100% (Flu A) 100% (Flu B)	100% (SARS-CoV-2) 100% (Flu A) 100% (Flu B)	nasopharyngeal swabs	Nucleocapsid protein	2.7 x 10^3 TCID50/mL (SARS-CoV-2)
QuickVue SARS Antigen Test	Quidel Corporation	96.60%	99.30%	anterior nares swabs	Nucleocapsid protein	7.57 x10^3 TCID50/mL
Sampinute COVID-19 Antigen MIA	Celltrion USA, Inc.	94.4%	100.0%	nasopharyngeal swabs	S protein (RBD)	3.0 × 10^1 TCID50/mL

Sofia 2 Flu + SARS Antigen FIA	Quidel Corporation	95.2% (SARS-CoV-2) 94.8% (Flu A) 78.5-90% (Flu B)	100% (SARS-CoV-2) 97-100% (Flu A) 100% (Flu B)	direct nasopharyngeal (NP) and nasal (NS) swab specimens	Nucleocapsid protein (for SARS-CoV-2, influenza A, and influenza B)	91.7 (SARS-CoV-2), 50 (flu A), 1.8 (Flu B) TCID50/mL
LumiraDx SARS-CoV-2 Ag Test	LumiraDx UK Ltd.	97.6%	96.6%	anterior nasal swab and nasopharyngeal swab samples	Nucleocapsid protein	32 TCID50/mL
INDICAID COVID-19 Rapid Antigen Test	PHASE Scientific International, Ltd.	84.4%	96.3%	anterior nasal swabs	nucleocapsid protein antigen	2.8 x 10^3 TCID50/mL
iHealth COVID-19 Antigen Rapid Test Pro	iHealth Labs, Inc.	94.3%	98.10%	anterior nasal swabs	N protein antigen	20 x 10^3 TCID50/mL
COVID-19 At-Home Test	SD Biosensor, Inc.	95.3% (symptomatic) [Ref. Roche https://www.roche.com/dam/jcr:bd4c0e73-c492-49f1-a4a1-e5ffa7d4fabb/en/24122021-mr-covid-19-at-home-test-en.pdf]	100% (symptomatic) [Ref: Roche https://www.roche.com/dam/jcr:bd4c0e73-c492-49f1-a4a1-e5ffa7d4fabb/en/24122021-mr-covid-19-at-home-test-en.pdf]	anterior nasal (nares) swab	nucleocapsid protein antigen	
CLINITEST Rapid COVID-19 Antigen Self-Test	Siemens Healthineers	86.5% (symptomatic) [Ref: FDA https://www.fda.gov/media/155175/download]	99.3% (symptomatic) [Ref: FDA https://www.fda.gov/media/155175/download]	anterior nasal (nares) swab samples	nucleocapsid protein antigen	7.0 x 103 TCID50/mL. [Ref: FDA https://www.fda.gov/media/155175/download]
Simoa SARS-CoV-2 N Protein Antigen Test	Quanterix Corporation	97.70%	100%	nasopharyngeal swab specimens collected in Huachenyang iClean Viral Transport Medium	Nucleocapsid protein	0.31 TCID50/mL
Nano-Check COVID-19 Antigen Test	Nano-Ditech Corp.	90.32%	100%	nasopharyngeal swabs	N protein antigen	7.0 x 10^2 TCID50/mL
CareStart COVID-19 Antigen test	Access Bio, Inc.	93.8% (NP), 87.2% (nasal)	99.3% (NP), 100% (nasal)	anterior nasal or nasopharyngeal swab specimens directly collected (or collected in BD universal transport media)	Nucleocapsid protein	800 TCID50/mL
CareStart COVID-19 Antigen Home Test	Access Bio, Inc.	87.0%	98.0%	anterior nasal swabs	nucleocapsid protein antigen	2.8 x 10^3 TCID50/mL
BD Veritor At-Home COVID-19 Test	Becton, Dickinson and Company (BD)	84.6%	99.80%	anterior nasal swabs	nucleocapsid protein antigen	1.87 x 10^2 TCID50/mL
SCoV-2 Ag Detect Rapid Self-Test	InBios International, Inc.	85.7%	100.0%	anterior nasal swabs	N protein antigen	6.3 x 10^3 TCID50/mL
Celltrion DiaTrust COVID-19 Ag Home Test	Celltrion USA, Inc.	86.7%	99.80%	mid-turbinate swabs	N protein, receptor binding domain	3.2 x 10^1 TCID50/mL
Flowflex COVID-19 Antigen Home Test	ACON Laboratories, Inc	93.0%	100.00%	anterior nasal swabs	N protein antigen	2.5 x 10^3 TCID50/mL
SPERA COVID-19 Ag Test	Xtrava Health	91.8%	96.90%	anterior nasal swabs	N protein antigen	1.56 x 10^3 TCID50/mL
NIDS COVID-19 Antigen Rapid Test Kit	ANP Technologies, Inc	95.1%	97.00%	mid-turbinate nasal swabs	N protein antigen	311 TCID50/mL
QIAreach SARS-CoV-2 Antigen	QIAGEN GmbH	85.0%	99.05%	anterior nasal and nasopharyngeal swabs	nucleocapsid protein antigen	5.0 x 10^4 TCID50/mL
LIAISON SARS-CoV-2 Ag	DiaSorin, Inc	97.00%	100%	nasopharyngeal swab, anterior nasal swab	nucleocapsid protein	300 TCID50/mL
ellume.lab COVID Antigen Test	Ellume Limited	81.80%	100%	mid-turbinate nasal swabs	N protein antigen	7.16 x 10^3 TCID50/mL
Ellume COVID-19 Home Test	Ellume Limited	96% (symptomatic), 91 % (asymptomatic)	100% (symptomatic), 96 % (asymptomatic)	mid-turbinate nasal swabs	Nucleocapsid antigen protein	103.80 TCID50/mL.
Clip COVID Rapid Antigen Test	Luminostics, Inc.	96.9% (symptomatic	100% (symptomatic)	anterior nasal swab	Nucleocapsid protein	0.88 x102 /mL.
iHealth COVID-19 Antigen Rapid Test	iHealth Labs, Inc.	84.3% (symptomatic	98.1% (symptomatic)	anterior nasal (nares) swab samples	Nucleocapsid protein	20×10^3 TCID50/mL.
MaximBio ClearDetect COVID-19 Antigen Home Test	Maxim Biomedical, Inc.	86.90%	98.90%	anterior nasal (nares) swab samples	Nucleocapsid protein	750 TCID50/mL.

APPENDIX 3: OUR EXPERIMENTAL DATA ON VEHICLE CONTROL (Using only DIW and PBS):

- State 1 is the state that represents the adhered COOH-PEG-SH after wash in both SARS-CoV-2 and Influenza A experiments.
- State 2 is the state that represents the adhered COOH-PEG-SH after being activated using EDC/NHS/MES/NaCl and after the washing step in both SARS-CoV-2 and Influenza A experiments.
- State 3 is the state that represents the adhered SARS-CoV-2 N mAb over our functionalized surface in both SARS-CoV-2 and Influenza A experiments.
- State 4 reflects the state of the surface with the adhered SARS-CoV-2 N antigen on top of the SARS-CoV-2 N monoclonal antibody (mAb) over our functionalized surface in both SARS-CoV-2 and Influenza A experiments.

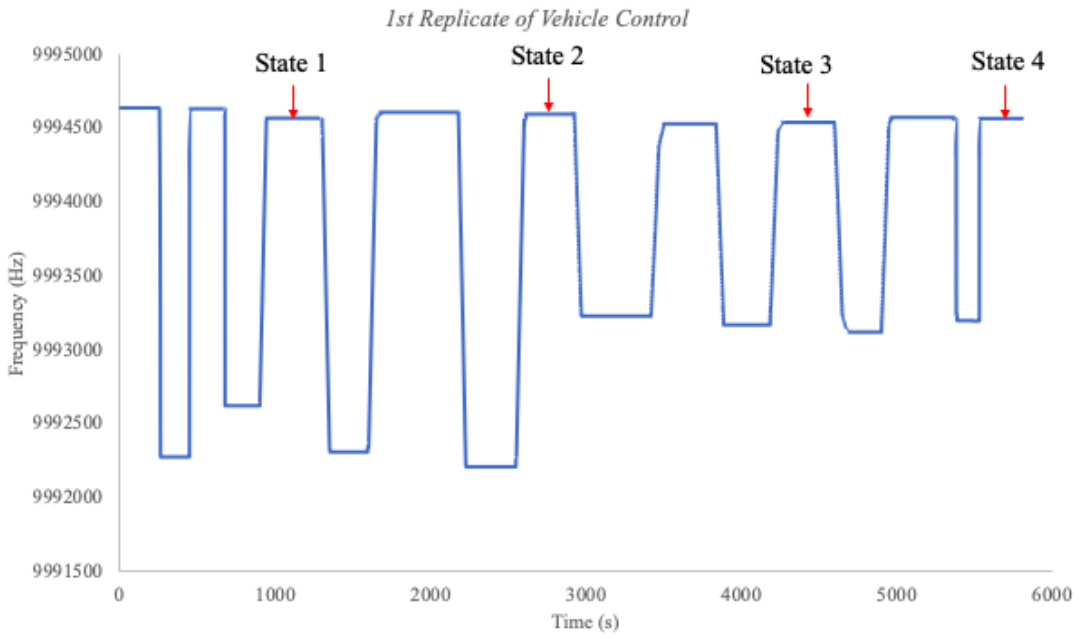

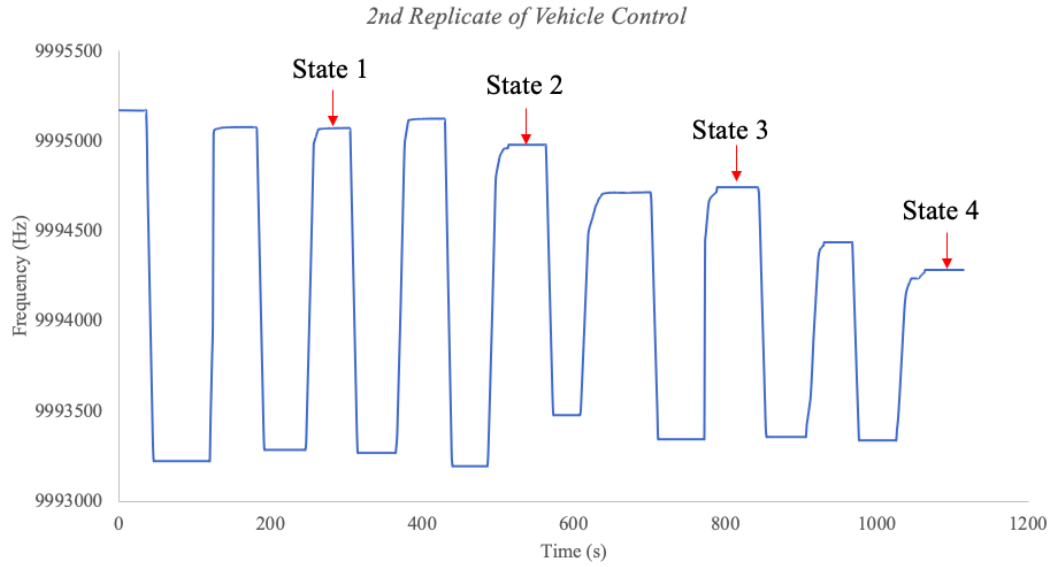
2nd Replicate of Vehicle Control
9995500
9995000
9994500
9994000
9993500
9993000
Frequency (Hz)
State 1
State 2
State 3
State 4
0
200
400
600
800
1000
1200
Time (s)

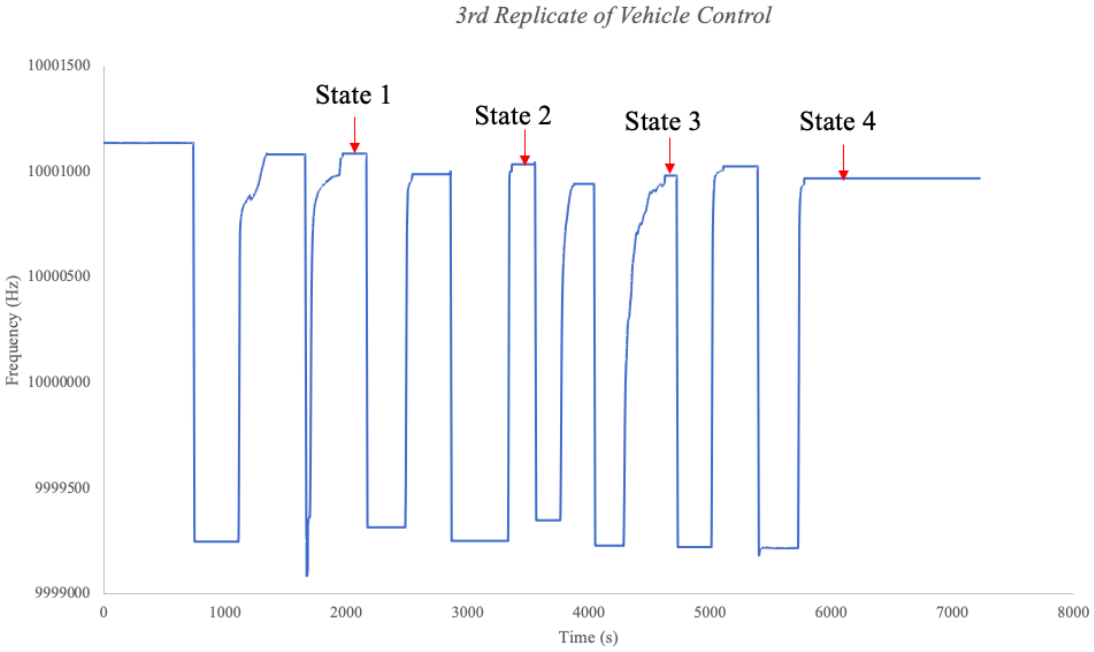
3rd Replicate of Vehicle Control
10001500
10001000
10000500
10000000
9999500
9999000
Frequency (Hz)
State 1
State 2
State 3
State 4
0
1000
2000
3000
4000
5000
6000
7000
8000
Time (s)

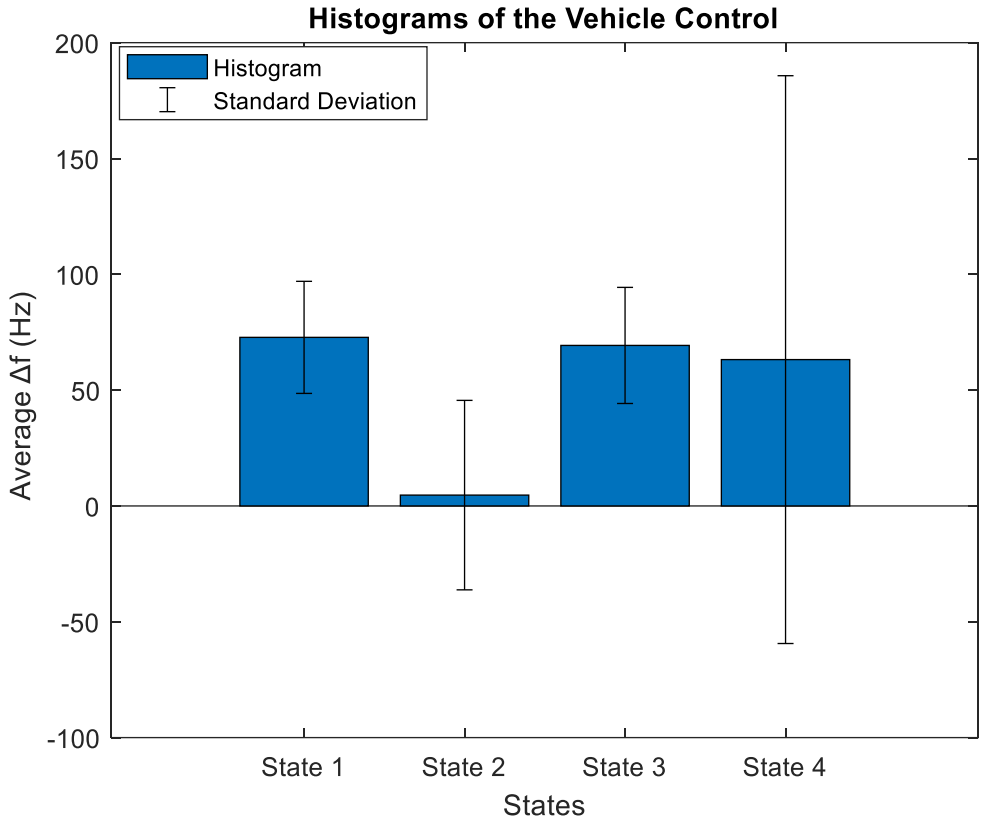

Appendix 4: Statistical Tests - Anova Test and T-Test

One-way Anova for all SARS-CoV-2 measurements with the negative control (Sensitivity):

F = 234.5

P value is <0.0001

P value summary ****

Significant diff. among means (P < 0.05)?

Yes

R squared = 0.9899

- The "F" number is a measure of how much the groups we're comparing (the different concentrations of SARS-CoV-2 and the negative control) are different from each other, compared to how much variation there is within each group.

the "F" value is quite high (234.5) which suggests there are real differences between the groups are real rather than random chance.

- The P-Value is less than 0.0001 which is extremely small. This is good as it suggests that the differences we're seeing are almost certainly not due to chance.
- The R squared value tells us that 98.99% of the variation in our data is due to change in viral concentration, which is a good sign.

Post-hoc Tukey's multiple comparison test:

Tukey's multiple comparisons test	Mean Diff.	95.00% CI of diff.	Significant?	Summary
Negative vs. 5.33x10^1	-17.08	-265.4 to 231.2	No	ns
Negative vs. 2.665x10^2	-73.02	-321.3 to 175.3	No	ns
Negative vs. 5.33x10^2	-95.09	-343.4 to 153.2	No	ns
Negative vs. 5.33x10^3	-1474	-1722 to -1225	Yes	****
Negative vs. 5.33x10^4	-1704	-1952 to -1455	Yes	****
5.33x10^1 vs. 2.665x10^2	-55.94	-304.3 to 192.4	No	ns
5.33x10^1 vs. 5.33x10^2	-78.02	-326.3 to 170.3	No	ns
5.33x10^1 vs. 5.33x10^3	-1457	-1705 to -1208	Yes	****
5.33x10^1 vs. 5.33x10^4	-1686	-1935 to -1438	Yes	****
2.665x10^2 vs. 5.33x10^2	-22.07	-270.4 to 226.2	No	ns

2.665x10^2 vs. 5.33x10^3	-1401	-1649 to -1152	Yes	****
2.665x10^2 vs. 5.33x10^4	-1630	-1879 to -1382	Yes	****
5.33x10^2 vs. 5.33x10^3	-1379	-1627 to -1130	Yes	****
5.33x10^2 vs. 5.33x10^4	-1608	-1857 to -1360	Yes	****
5.33x10^3 vs. 5.33x10^4	-229.8	-478.1 to 18.48	No	ns

This test showed that:

There is a significant difference in means between the negative control and the highest concentrations of SARS-CoV-2, particularly 5.33x10^3, as well as significant differences among different concentrations of the virus.

No significant difference between the negative control and the groups with lower concentrations of the virus (5.33x10^1, 2.665x10^2, and 5.33x10^2), nor between the two highest concentrations (5.33x10^3 vs. 5.33x10^4).

The results suggest that the sensor can differentiate between negative controls and high concentrations of SARS-CoV-2, as well as among different concentrations of SARS-CoV-2.

Mann-Whitney Test for negative and influenza A values:

Mann Whitney test

P value = 0.1000

Exact or approximate P value?

Exact

P value summary

ns

Significantly different (P < 0.05)?

No

One- or two-tailed P value?

Two-tailed

Mann-Whitney U

0

This test showed that:

There is no statistical difference between the negative and influenza A sample.

This suggest that the sensor does not respond significantly to influenza A, even at the high concentration of 2.97 x 10^7 TCID50/ml.

Note: Mann-Whitney test was used here since the sample size is small (n=3 for replicates) and we cannot assume a normal distribution and use unpaired t-test.

Unpaired t-test for 5.33 x 10^4 of SARS-CoV-2 with 2.97x 10^7 influenza A (Specificity):

Unpaired t test

P value is <0.0001

P value summary

****

Significantly different (P < 0.05)? Yes

One- or two-tailed P value? Two-tailed

t, df are as follow t=20.84, df=4

This test showed that:

There is a statistical difference between the two viruses at the specified concentration

This suggest that the sensor selectively respond to SARS-CoV-2 rather than influenza A using the mentioned concentrations.

Note: Mann-Whitney test should have been used here, but the P vale was not significant (data not shown). This is most likely due to the striking difference in readings of the sensor between the two viruses.

APPENDIX 5: OUR EXPERIMENTAL DATA ON SARS-CoV-2:

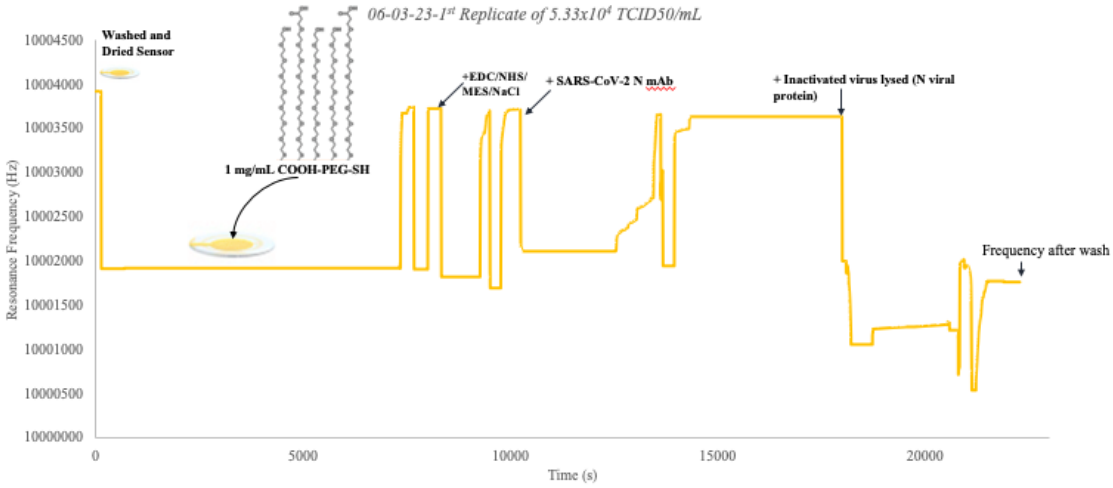

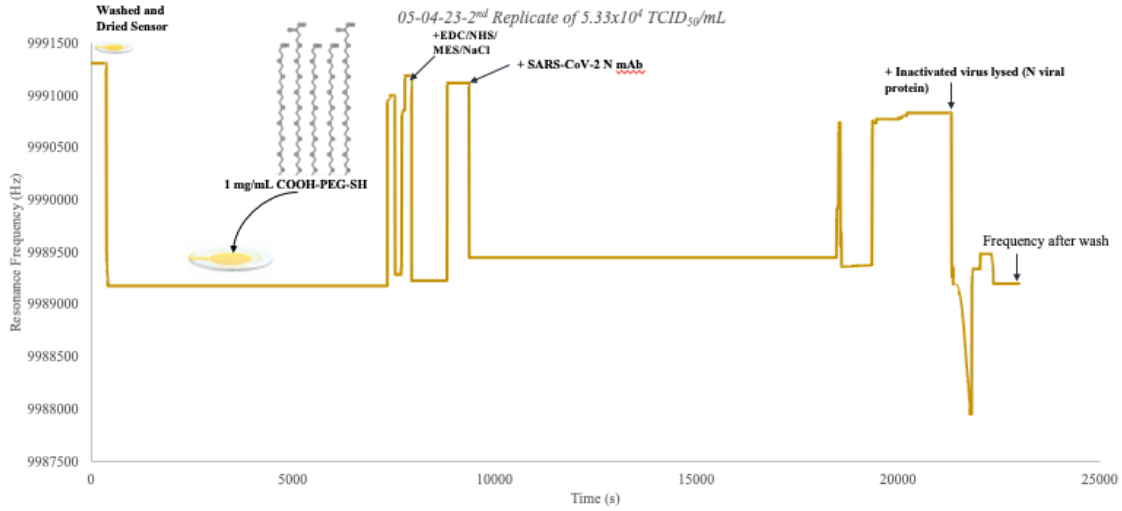
05-04-23-2nd Replicate of 5.33x10⁴ TCID50/mL
Washed and Dried Sensor
+EDC/NHS/ MES/NaCl
+ SARS-CoV-2 N mAb
+ Inactivated virus lysed (N viral protein)
1 mg/mL COOH-PEG-SH
Frequency after wash
Resonance Frequency (Hz)
Time (s)

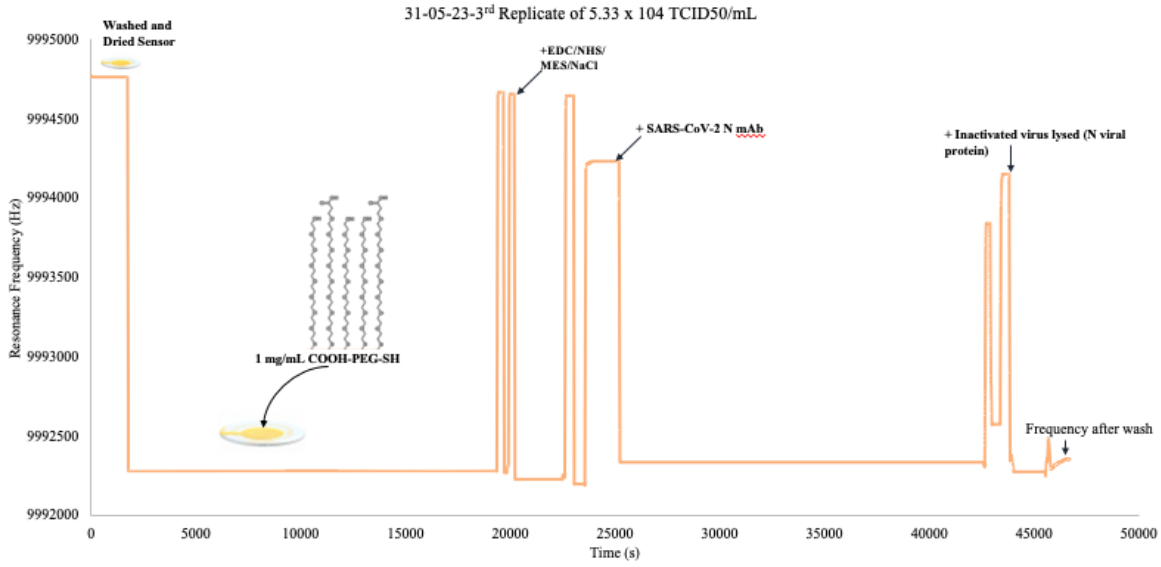
31-05-23-3rd Replicate of 5.33 x 104 TCID50/mL
Washed and Dried Sensor
+EDC/NHS/ MES/NaCl
+ SARS-CoV-2 N mAb
+ Inactivated virus lysed (N viral protein)
1 mg/mL COOH-PEG-SH
Frequency after wash
Resonance Frequency (Hz)
Time (s)

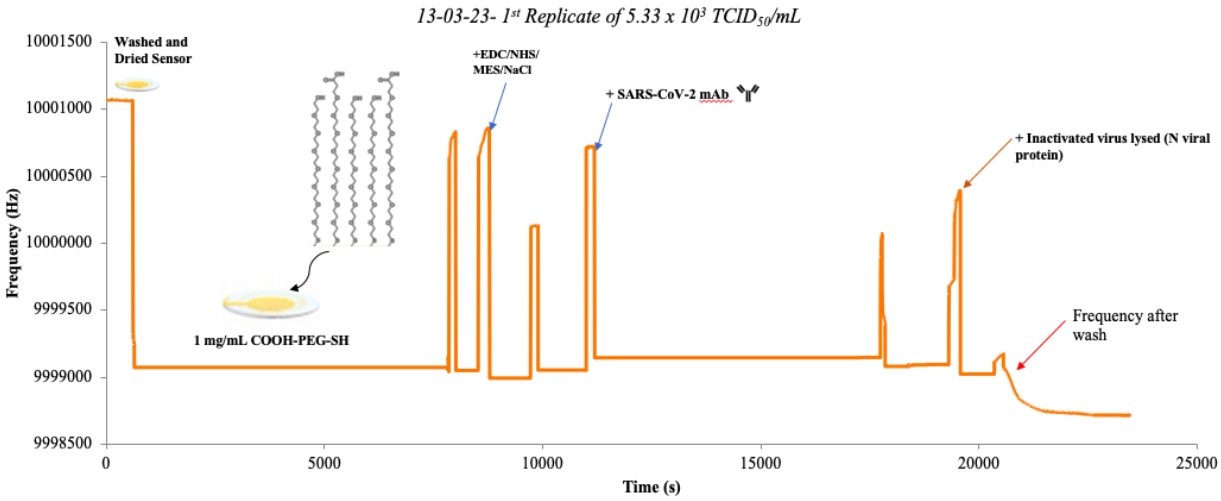
13-03-23- 1st Replicate of 5.33 x 10³ TCID50/mL
Washed and Dried Sensor
+EDC/NHS/ MES/NaCl
+ SARS-CoV-2 mAb
+ Inactivated virus lysed (N viral protein)
1 mg/mL COOH-PEG-SH
Frequency after wash
Frequency (Hz)
Time (s)

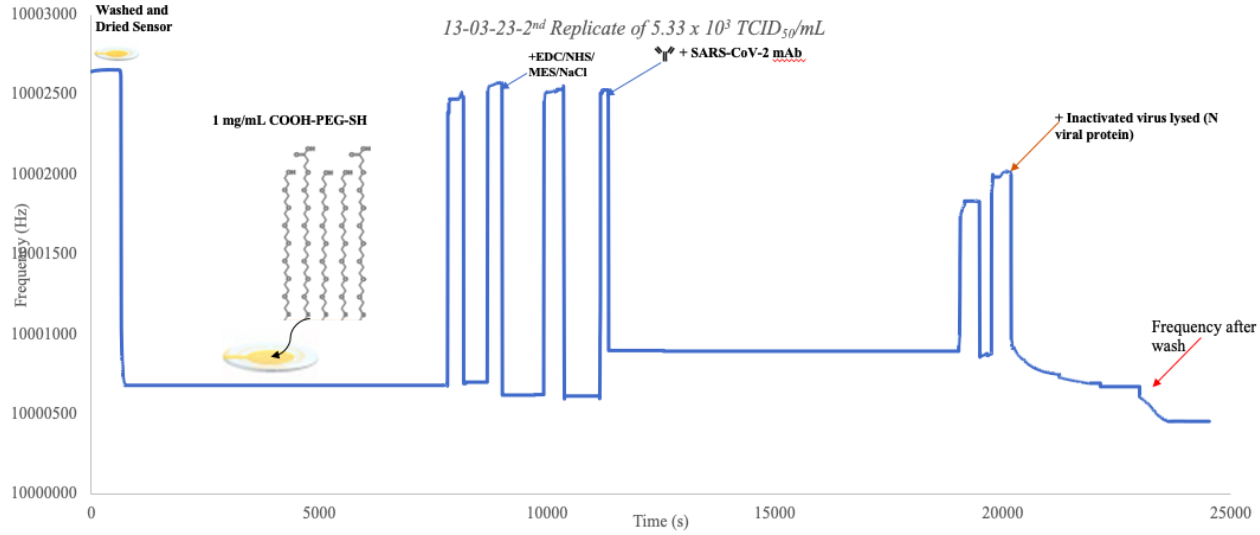
13-03-23-2nd Replicate of 5.33 x 10³ TCID50/mL
Washed and Dried Sensor
+EDC/NHS/ MES/NaCl
+ SARS-CoV-2 mAb
1 mg/mL COOH-PEG-SH
+ Inactivated virus lysed (N viral protein)
Frequency after wash
Frequency (Hz)
Time (s)

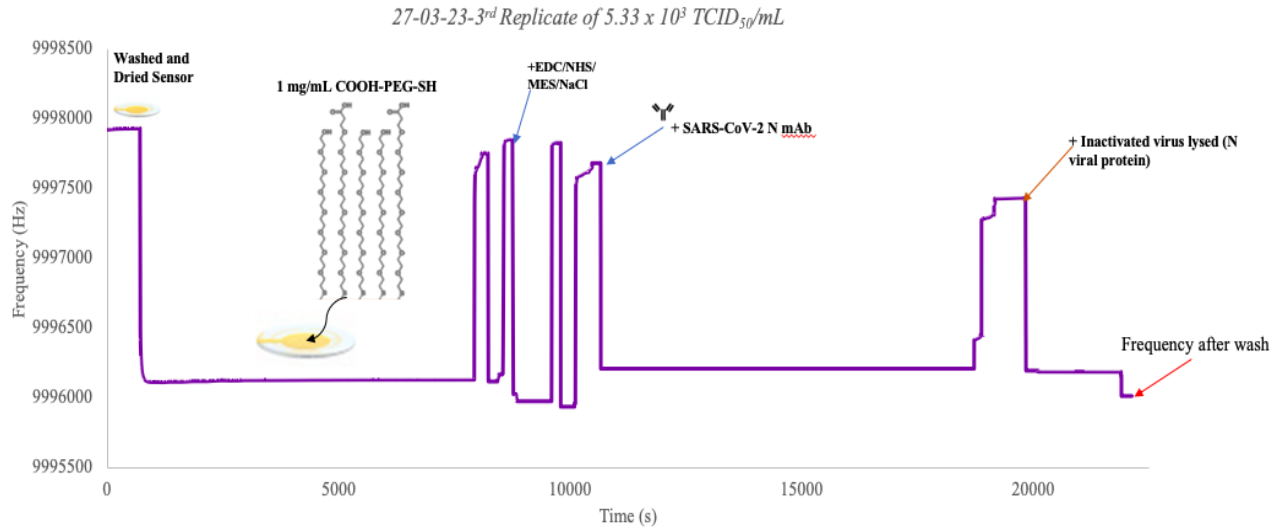
27-03-23-3rd Replicate of 5.33 x 10³ TCID50/mL
Washed and Dried Sensor
1 mg/mL COOH-PEG-SH
+EDC/NHS/ MES/NaCl
+ SARS-CoV-2 N mAb
+ Inactivated virus lysed (N viral protein)
Frequency after wash
Frequency (Hz)
Time (s)

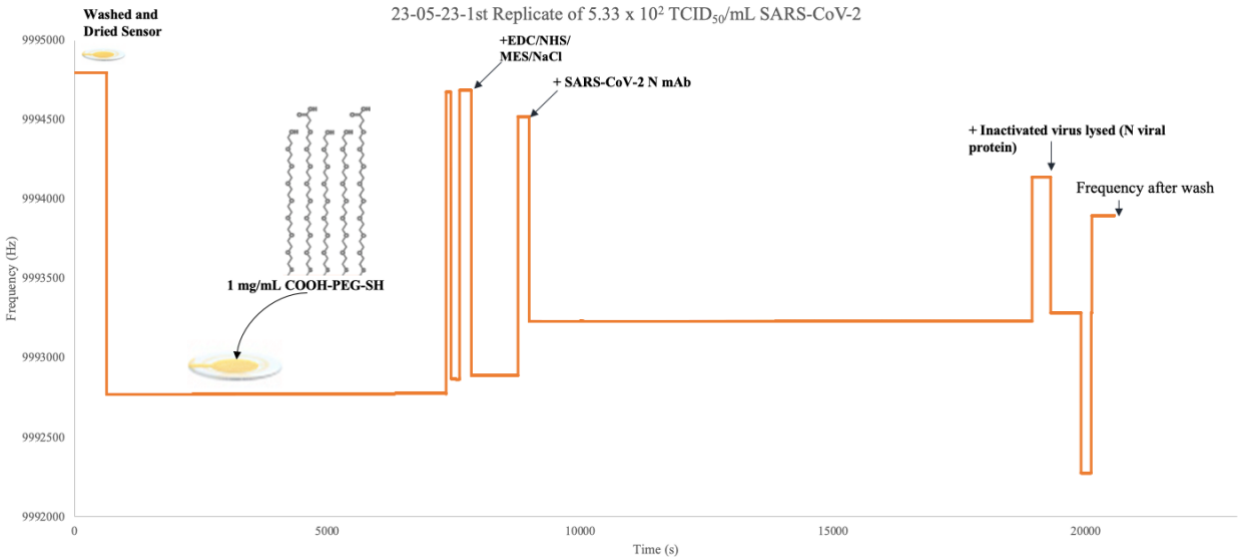
23-05-23-1st Replicate of 5.33 x 10² TCID50/mL SARS-CoV-2
Washed and Dried Sensor
+EDC/NHS/ MES/NaCl
+ SARS-CoV-2 N mAb
+ Inactivated virus lysed (N viral protein)
Frequency after wash
1 mg/mL COOH-PEG-SH
Frequency (Hz)
Time (s)

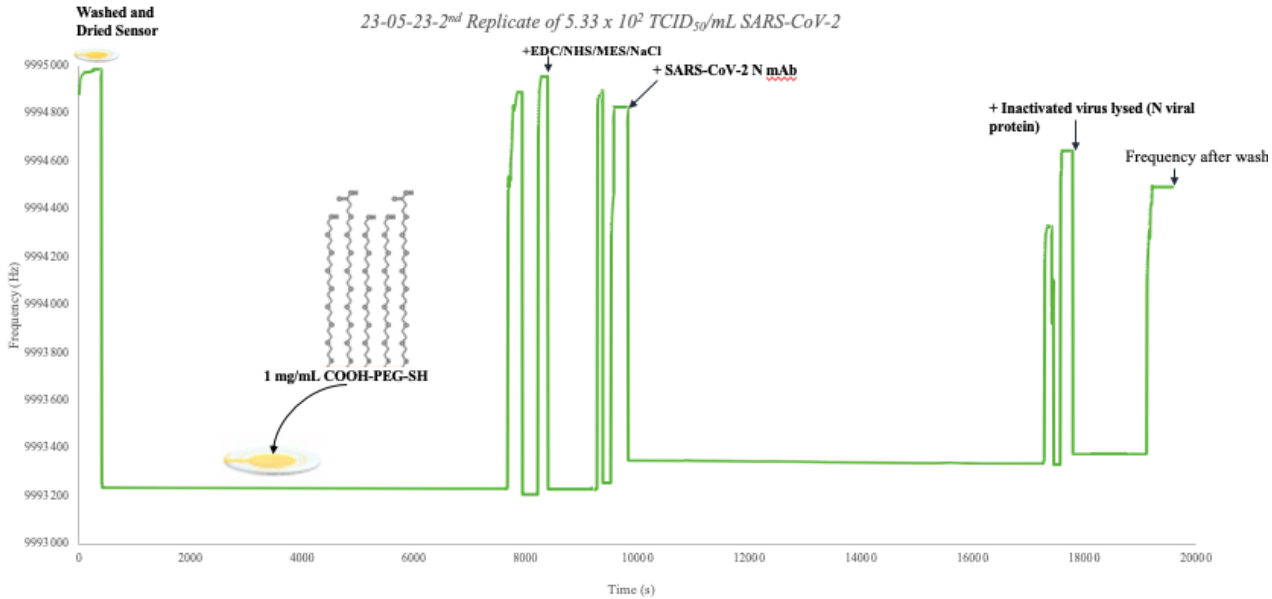
23-05-23-2nd Replicate of 5.33 x 10² TCID50/mL SARS-CoV-2
Washed and Dried Sensor
+EDC/NHS/MES/NaCl
+ SARS-CoV-2 N mAb
+ Inactivated virus lysed (N viral protein)
Frequency after wash
1 mg/mL COOH-PEG-SH
Frequency (Hz)
Time (s)

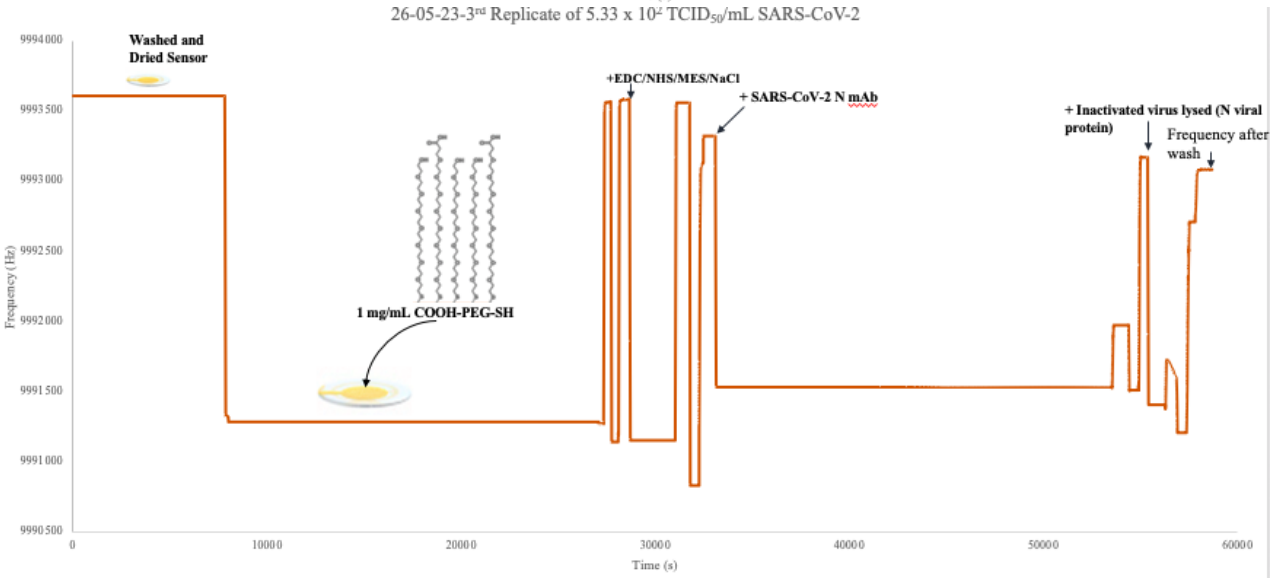
26-05-23-3rd Replicate of 5.33 x 10² TCID50/mL SARS-CoV-2
Washed and Dried Sensor
+EDC/NHS/MES/NaCl
+ SARS-CoV-2 N mAb
+ Inactivated virus lysed (N viral protein)
Frequency after wash
1 mg/mL COOH-PEG-SH
Frequency (Hz)
Time (s)

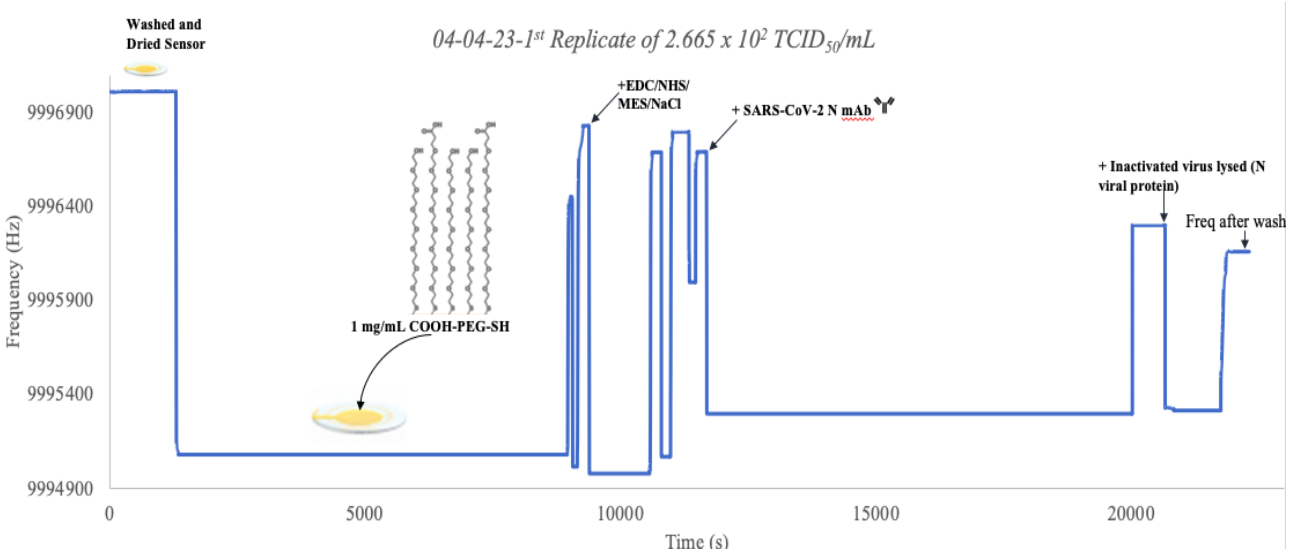
04-04-23-1st Replicate of 2.665 x 10² TCID50/mL
Washed and Dried Sensor
+EDC/NHS/ MES/NaCl
+ SARS-CoV-2 N mAb
+ Inactivated virus lysed (N viral protein)
Freq after wash
1 mg/mL COOH-PEG-SH
Frequency (Hz)
9996900
9996400
9995900
9995400
9994900
0
5000
10000
15000
20000
Time (s)

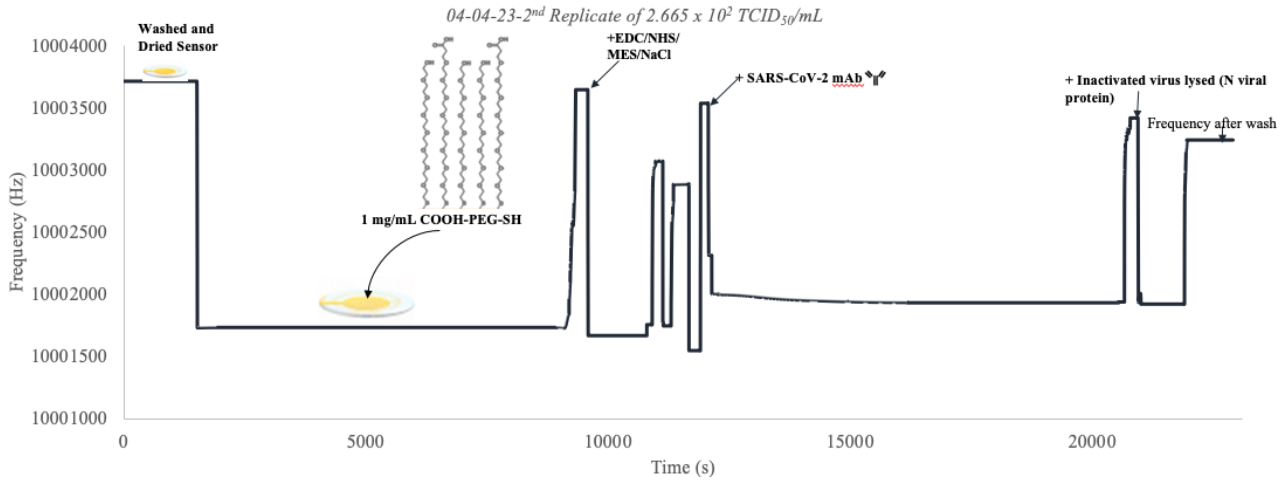
04-04-23-2nd Replicate of 2.665 x 10² TCID50/mL
Washed and Dried Sensor
+EDC/NHS/ MES/NaCl
+ SARS-CoV-2 mAb
+ Inactivated virus lysed (N viral protein)
Frequency after wash
1 mg/mL COOH-PEG-SH
Frequency (Hz)
10004000
10003500
10003000
10002500
10002000
10001500
10001000
0
5000
10000
15000
20000
Time (s)

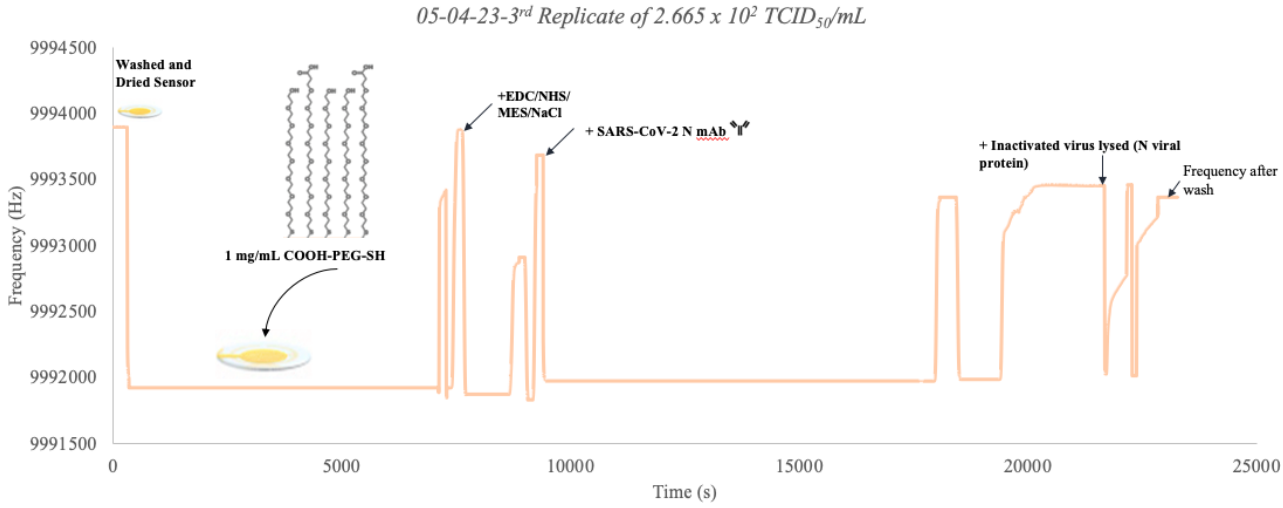
05-04-23-3rd Replicate of 2.665 x 10² TCID50/mL
Washed and Dried Sensor
+EDC/NHS/ MES/NaCl
+ SARS-CoV-2 N mAb
+ Inactivated virus lysed (N viral protein)
Frequency after wash
1 mg/mL COOH-PEG-SH
Frequency (Hz)
9994500
9994000
9993500
9993000
9992500
9992000
9991500
0
5000
10000
15000
20000
25000
Time (s)

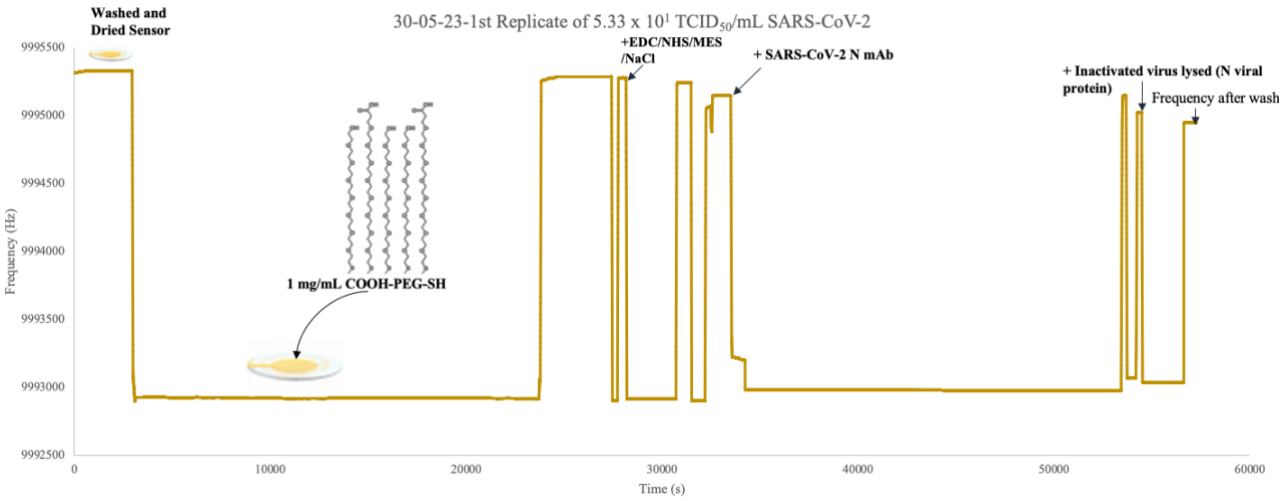
30-05-23-1st Replicate of 5.33 x 10¹ TCID50/mL SARS-CoV-2
Washed and Dried Sensor
+EDC/NHS/MES /NaCl
+ SARS-CoV-2 N mAb
+ Inactivated virus lysed (N viral protein)
Frequency after wash
1 mg/mL COOH-PEG-SH
Frequency (Hz)
Time (s)

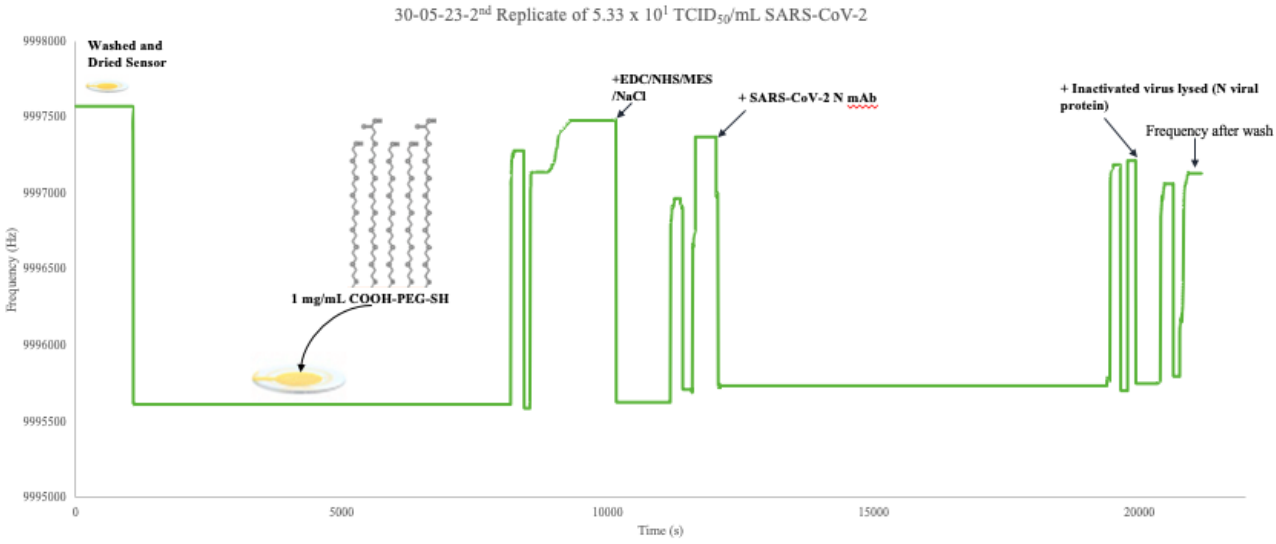
30-05-23-2nd Replicate of 5.33 x 10¹ TCID50/mL SARS-CoV-2
Washed and Dried Sensor
+EDC/NHS/MES /NaCl
+ SARS-CoV-2 N mAb
+ Inactivated virus lysed (N viral protein)
Frequency after wash
1 mg/mL COOH-PEG-SH
Frequency (Hz)
Time (s)

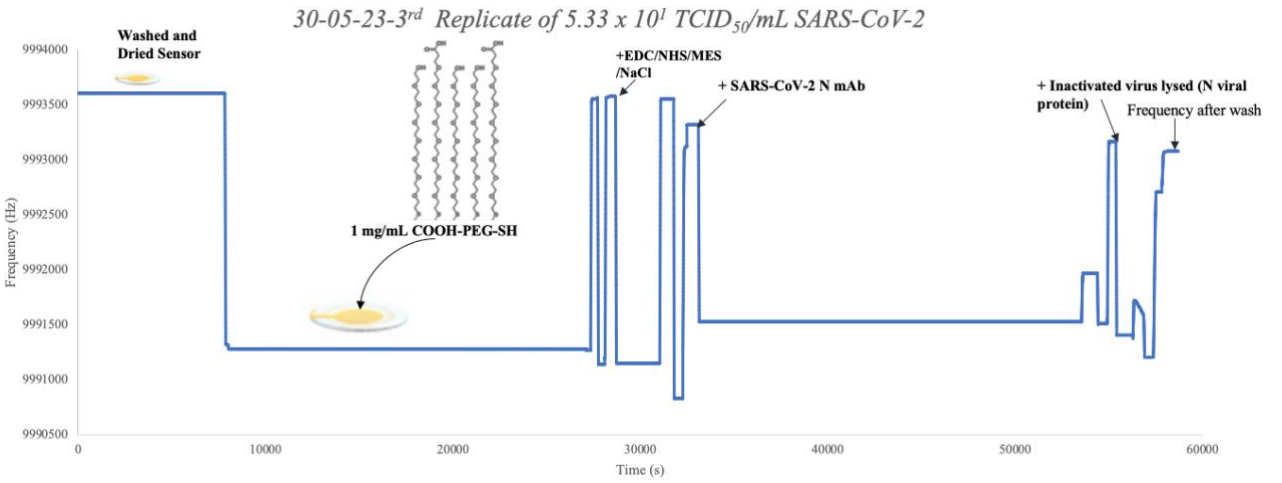
30-05-23-3rd Replicate of 5.33 x 10¹ TCID50/mL SARS-CoV-2
Washed and Dried Sensor
+EDC/NHS/MES /NaCl
+ SARS-CoV-2 N mAb
+ Inactivated virus lysed (N viral protein)
Frequency after wash
1 mg/mL COOH-PEG-SH
Frequency (Hz)
Time (s)

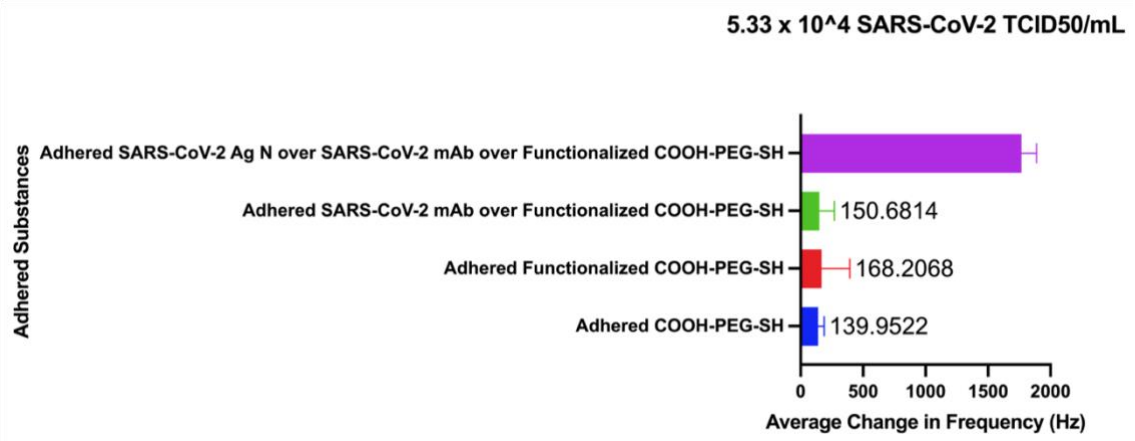
5.33 x 10^4 SARS-CoV-2 TCID50/mL
Adhered Substances
Adhered SARS-CoV-2 Ag N over SARS-CoV-2 mAb over Functionalized COOH-PEG-SH
Adhered SARS-CoV-2 mAb over Functionalized COOH-PEG-SH
150.6814
Adhered Functionalized COOH-PEG-SH
168.2068
Adhered COOH-PEG-SH
139.9522
0
500
1000
1500
2000
Average Change in Frequency (Hz)

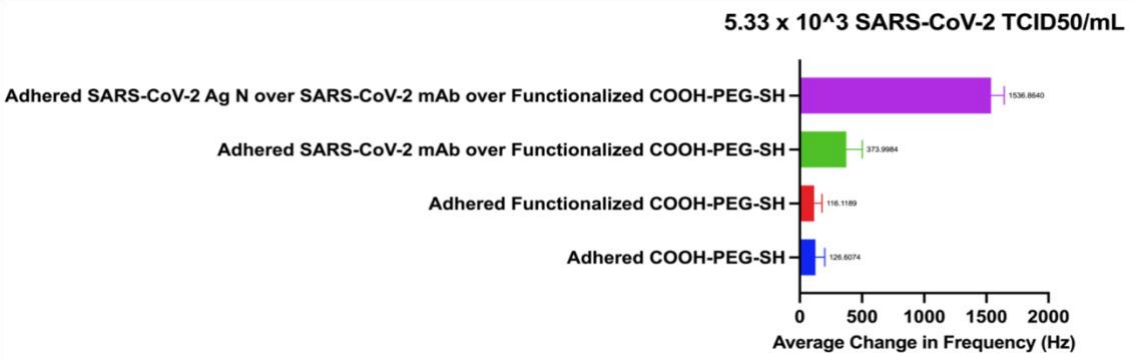
5.33 x 10^3 SARS-CoV-2 TCID50/mL
Adhered SARS-CoV-2 Ag N over SARS-CoV-2 mAb over Functionalized COOH-PEG-SH
1536.8640
Adhered SARS-CoV-2 mAb over Functionalized COOH-PEG-SH
373.9984
Adhered Functionalized COOH-PEG-SH
116.1189
Adhered COOH-PEG-SH
126.6074
0
500
1000
1500
2000
Average Change in Frequency (Hz)

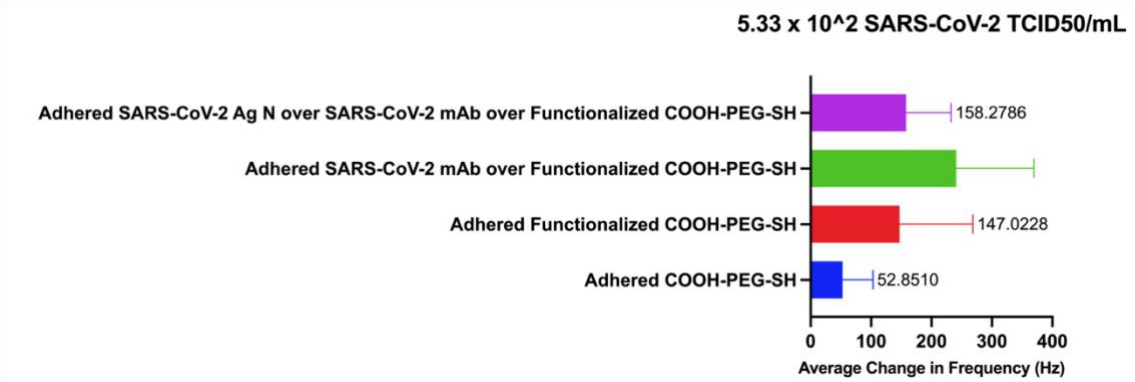
5.33 x 10^2 SARS-CoV-2 TCID50/mL
Adhered SARS-CoV-2 Ag N over SARS-CoV-2 mAb over Functionalized COOH-PEG-SH
158.2786
Adhered SARS-CoV-2 mAb over Functionalized COOH-PEG-SH
Adhered Functionalized COOH-PEG-SH
147.0228
Adhered COOH-PEG-SH
52.8510
0
100
200
300
400
Average Change in Frequency (Hz)

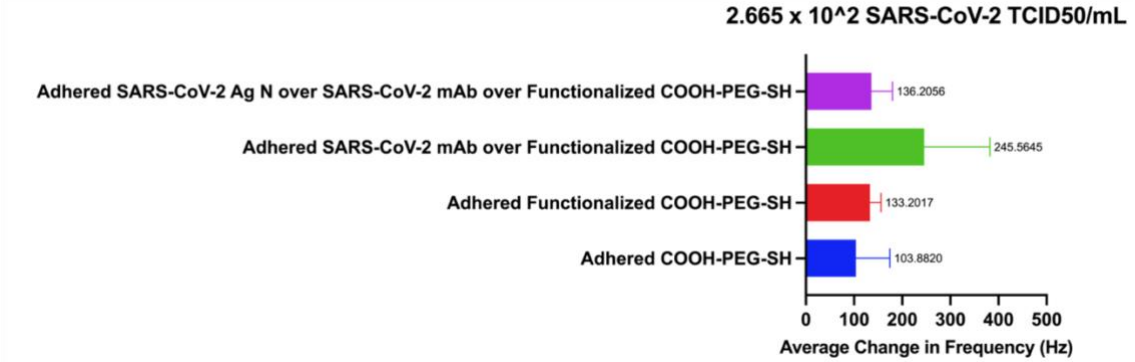
2.665 x 10^2 SARS-CoV-2 TCID50/mL
Adhered SARS-CoV-2 Ag N over SARS-CoV-2 mAb over Functionalized COOH-PEG-SH
136.2056
Adhered SARS-CoV-2 mAb over Functionalized COOH-PEG-SH
245.5645
Adhered Functionalized COOH-PEG-SH
133.2017
Adhered COOH-PEG-SH
103.8820
0
100
200
300
400
500
Average Change in Frequency (Hz)

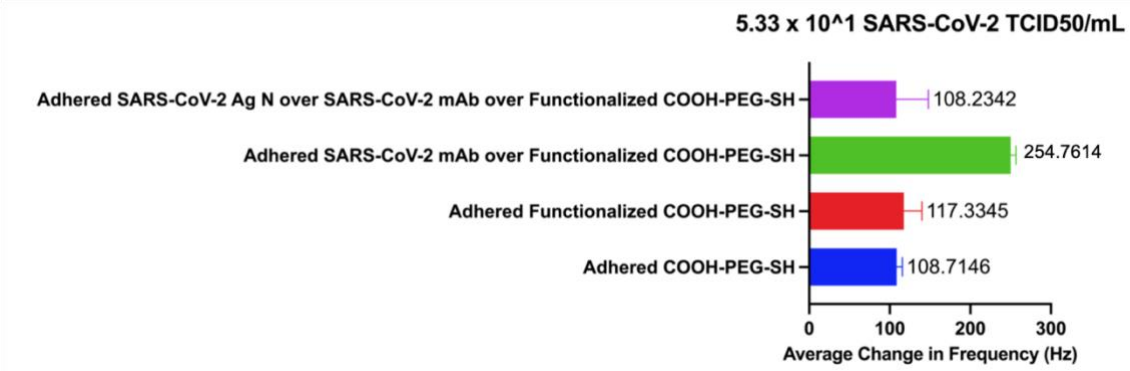
5.33 x 10^1 SARS-CoV-2 TCID50/mL
Adhered SARS-CoV-2 Ag N over SARS-CoV-2 mAb over Functionalized COOH-PEG-SH
108.2342
Adhered SARS-CoV-2 mAb over Functionalized COOH-PEG-SH
254.7614
Adhered Functionalized COOH-PEG-SH
117.3345
Adhered COOH-PEG-SH
108.7146
0
100
200
300
Average Change in Frequency (Hz)

6. APPENDIX 6: OUR EXPERIMENTAL DATA ON INFLUENZA A TRIALS:

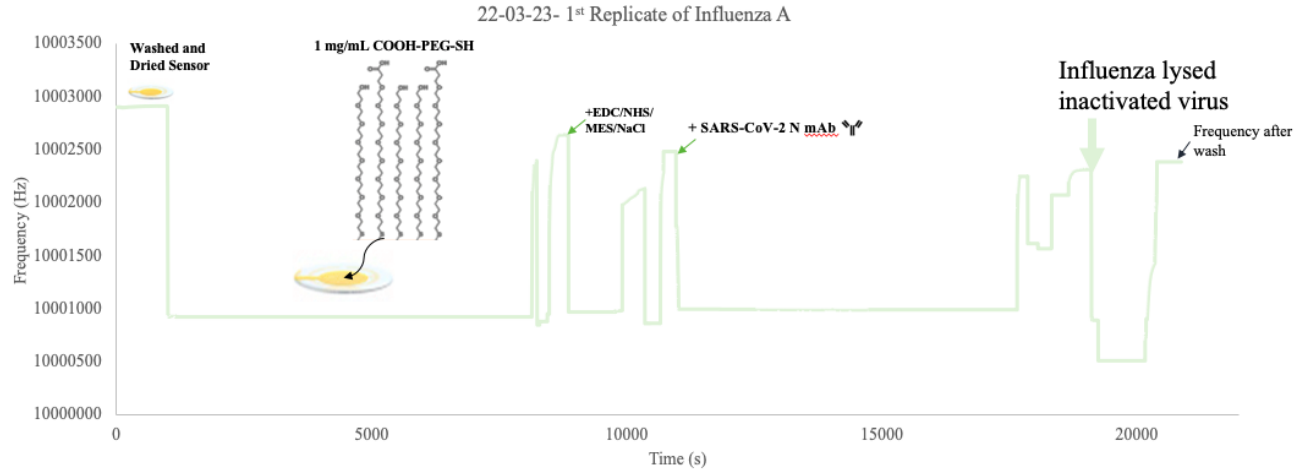

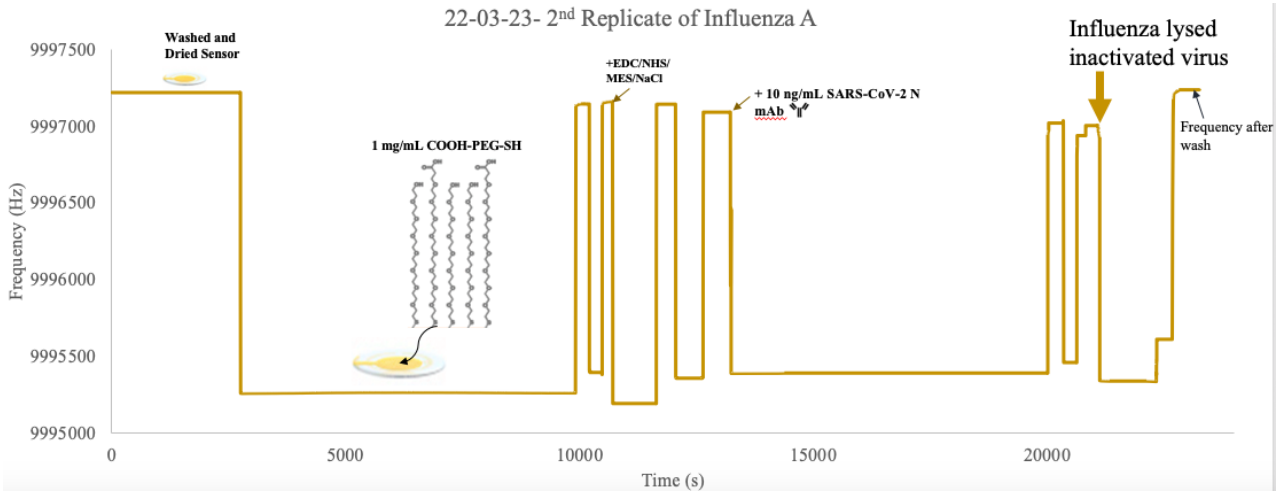

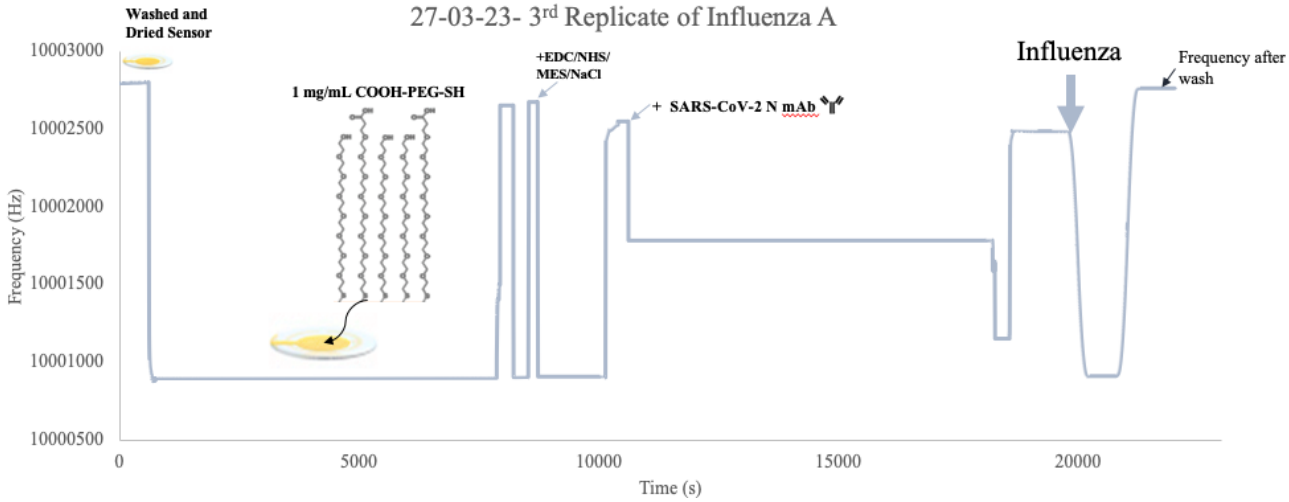

APPENDIX 7: OUR EXPERIMENTAL DATA ON 5 ng/mL Ab:

5 ng/mL mAb Experiment

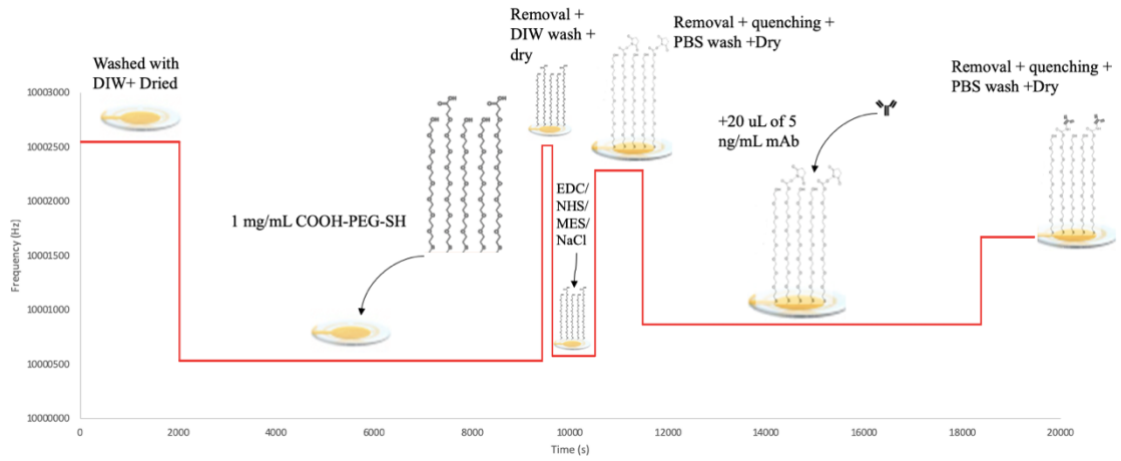

5 ng/mL mAb Experimental Trial

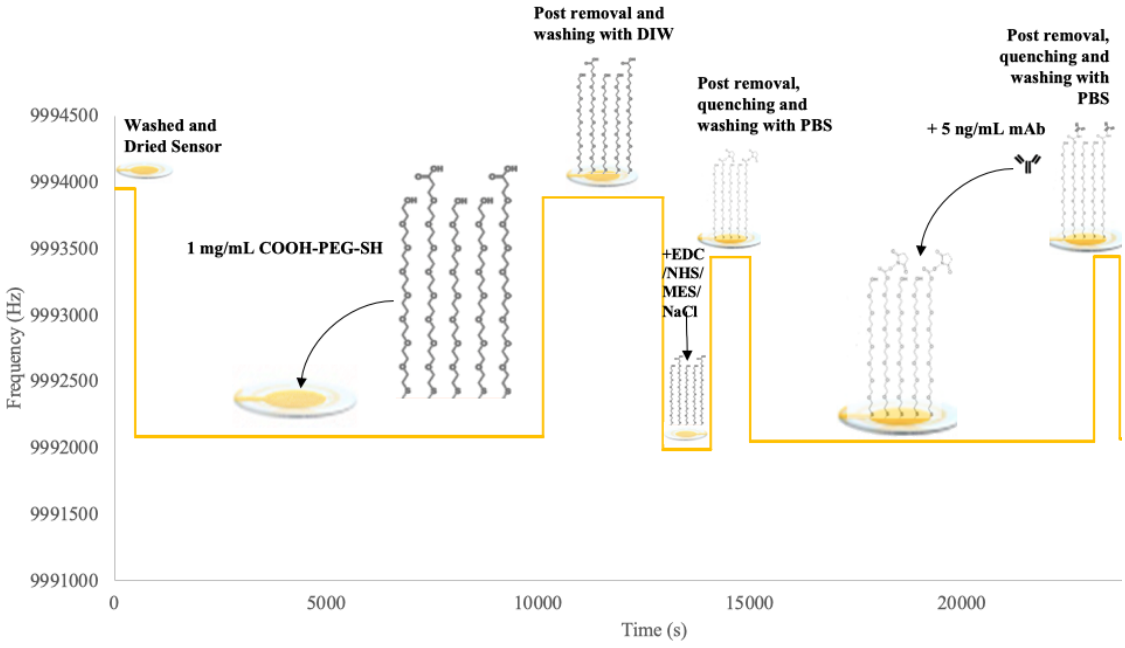

APPENDIX 8: RESULTS OF FLUORESENCE MICROSCOPY:

Bare Gold Result:

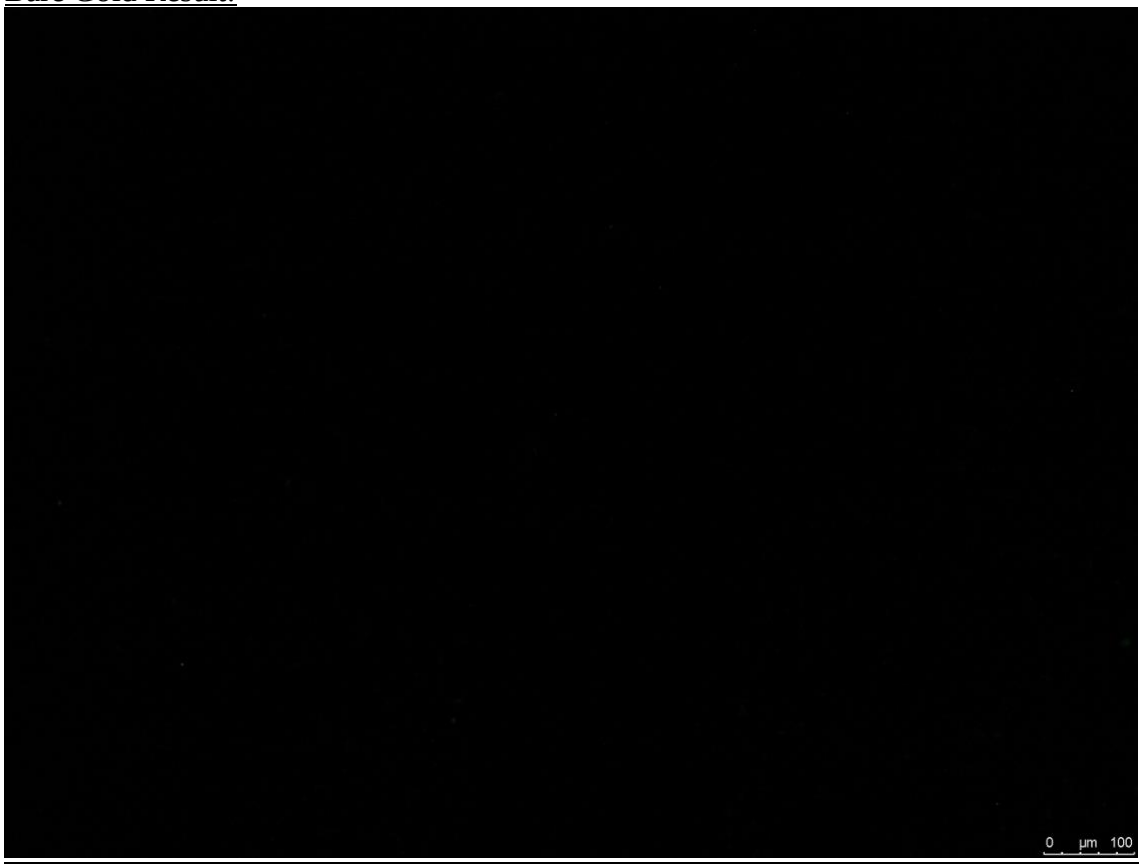

- COOH-PEG-SH only Sensor Result:

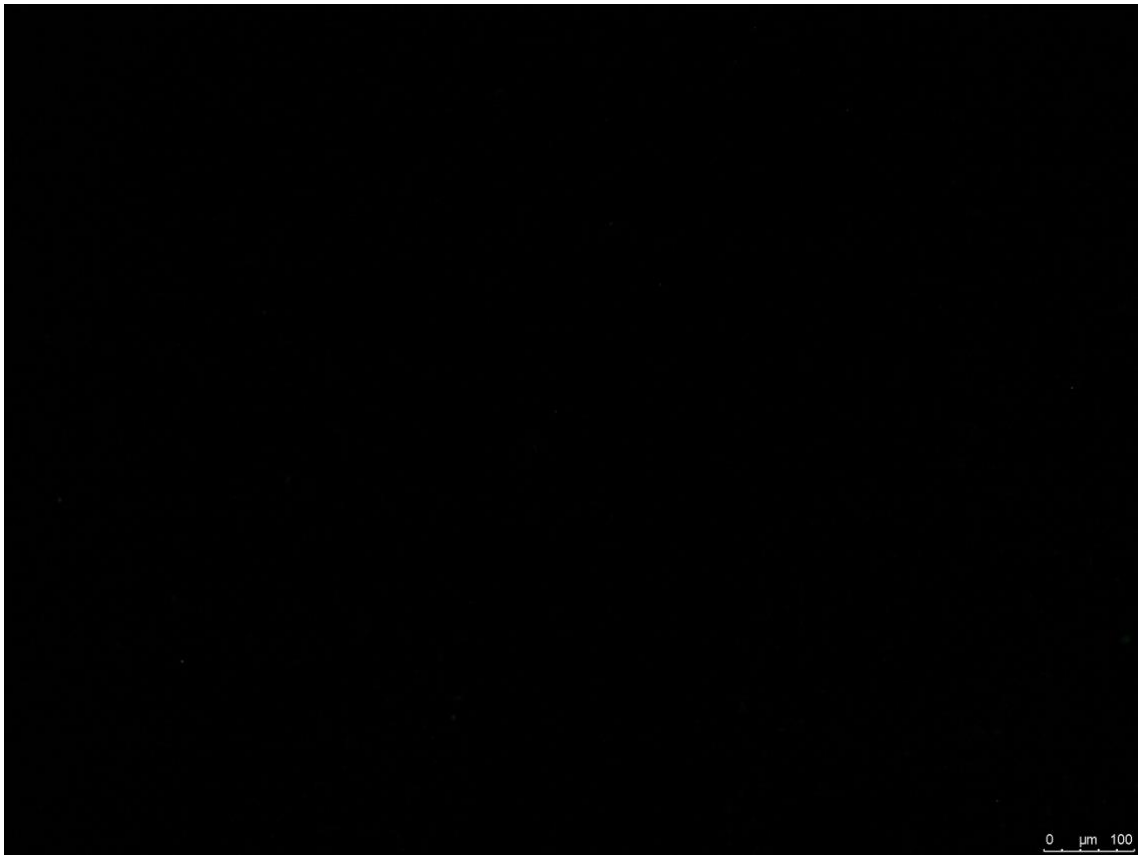

- Sensor with having 2ry Ab added on top of 1ry Ab immobilized on functionalized COOH-PEG-SH layer:

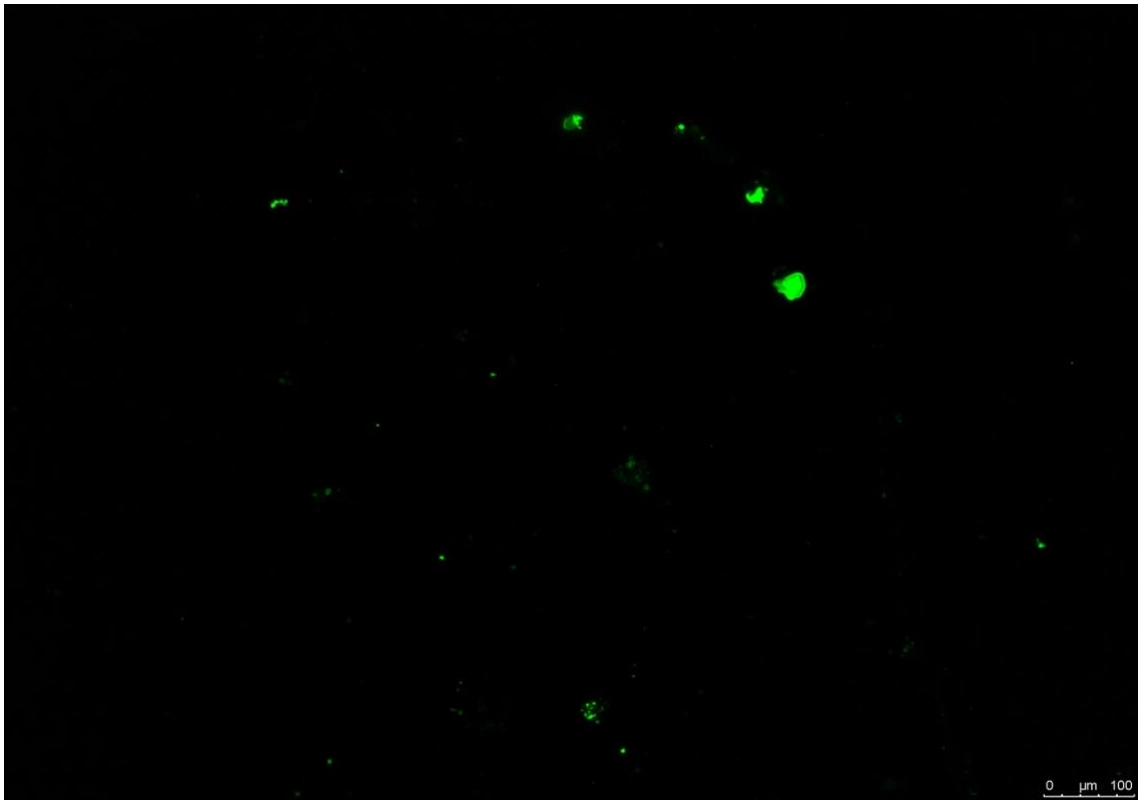

- Washed and Dried Sensor with having 2ry Ab added on top of 1ry Ab immobilized on functionalized COOH-PEG-SH layer:

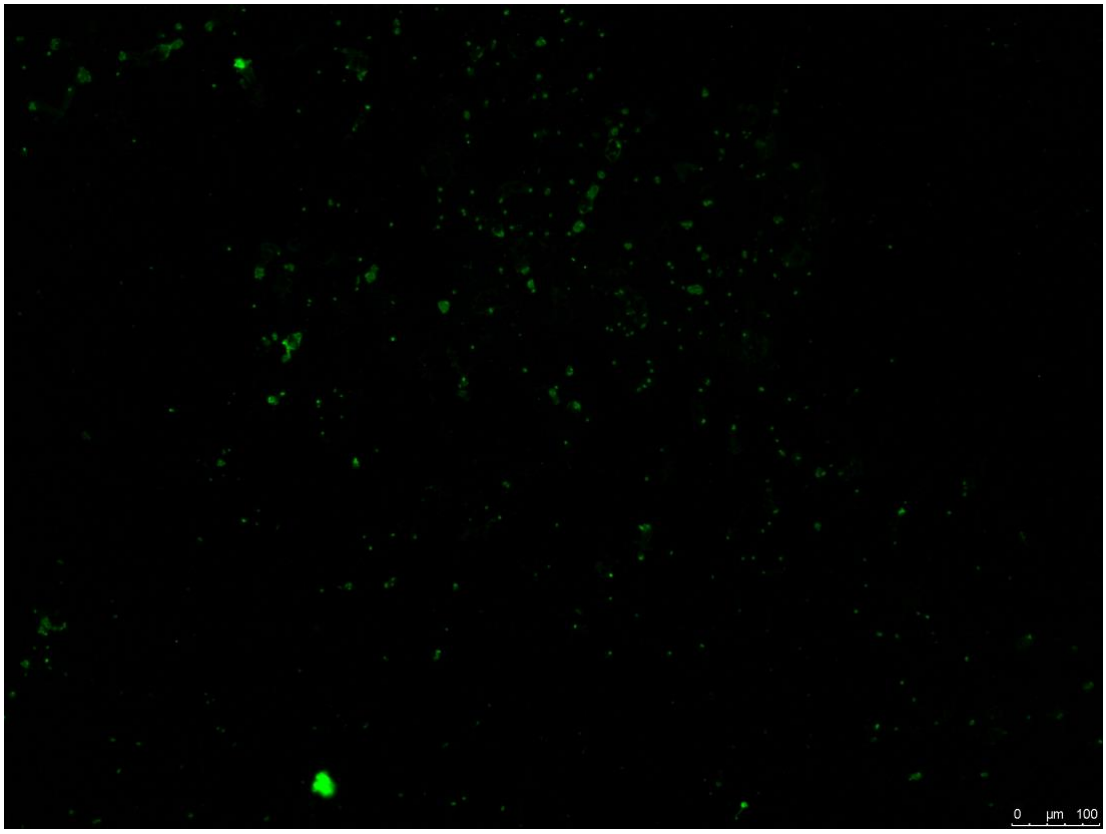
0 µm 100

BIBLIOGRAPHY

10 MHZ QUARTZ SENSORS BOX FOR LIQUID BIOSENSING- 10 PIECES. (n.d.). Retrieved June 3, 2023, from https://store.openqcm.com/10-mhz-quartz-sensors-box-for-liquid-biosensing-10-pieces/

Al Bayat, S., Mundodan, J., Hasnain, S., Sallam, M., Khogali, H., Ali, D., Alateeg, S., Osama, M., Elberdiny, A., Al-Romaihi, H., & Al-Thani, M. H. J. (2021). Can the cycle threshold (Ct) value of RT-PCR test for SARS CoV2 predict infectivity among close contacts? *Journal of Infection and Public Health*, *14*(9), 1201–1205. https://doi.org/10.1016/j.jiph.2021.08.013

Al-Alawi, S., Al-Hinai, H., Al-Kindi, N., Al-Rashidi, M., Al-Kindi, H., Al-Shukri, I., Al-Rashdi, A., Jose, S., & Al-Jardani, A. (2021). Evaluation of Four Rapid Antigen Tests for Detection of SARS-CoV-2 virus. *Oman Medical Journal*, *36*(5), e297. https://doi.org/10.5001/omj.2021.106

Alawieh, H., Chemaly, T. E., Alam, S., & Khraiche, M. (2019). Towards Point-of-Care Heart Failure Diagnostic Platforms: BNP and NT-proBNP Biosensors. *Sensors (Basel, Switzerland)*, *19*(22). https://doi.org/10.3390/s19225003

AlChamaa, W., & Khraiche, M. (2022). High Performance Fully Inkjet-Printed Organic Electrochemical Transistor (OECT) Biosensor. *Journal of The Electrochemical Society*, *169*(8), 087518. https://doi.org/10.1149/1945-7111/ac88fa

Antigen Tests | COVID-19 Testing Toolkit. (n.d.). Retrieved June 3, 2023, from https://covid19testingtoolkit.centerforhealthsecurity.org/basics/types-of-covid-19-tests/diagnostic-tests/antigen-tests

Antiochia, R. (2021). Developments in biosensors for CoV detection and future trends. *Biosensors & Bioelectronics*, *173*, 112777. https://doi.org/10.1016/j.bios.2020.112777

Bala, T., Prasad, B. L. V., Sastry, M., Kahaly, M. U., & Waghmare, U. V. (2007). Interaction of Different Metal Ions with Carboxylic Acid Group: A Quantitative Study. *The Journal of Physical Chemistry A*, *111*(28), 6183–6190. https://doi.org/10.1021/jp067906x

Batool, R., Soler, M., Colavita, F., Fabeni, L., Matusali, G., & Lechugaa, L. M. (2023). *Biomimetic nanoplasmonic sensor for rapid evaluation of neutralizing SARS-CoV-2 monoclonal antibodies as antiviral therapy—PMC*. https://www.ncbi.nlm.nih.gov/pmc/articles/PMC9904857/

Benevides Lima, L., Mesquita, F. P., Brasil de Oliveira, L. L., Andréa da Silva Oliveira, F., Elisabete Amaral de Moraes, M., Souza, P. F. N., & Montenegro, R. C. (n.d.). True or false: What are the factors that influence COVID-19 diagnosis by RT-qPCR? *Expert Review of Molecular Diagnostics*, 1–11. https://doi.org/10.1080/14737159.2022.2037425

Bentzen, E. L., Tomlinson, I. D., Mason, J., Gresch, P., Warnement, M. R., Wright, D., Sanders-Bush, E., Blakely, R., & Rosenthal, S. J. (2005). Surface Modification To Reduce Nonspecific Binding of Quantum Dots in Live Cell Assays. *Bioconjugate Chemistry*, *16*(6), 1488–1494. https://doi.org/10.1021/bc0502006

Bhatt, M., Einstein, C., Kiran, Fayaz, A., Rai, V., Karki, M., Kumar, A., Yadav, A. K., & Rajak, K. K. (2022). Methods for Quantification of Viruses. In R. Deb, A. K. Yadav, S. Rajkhowa, & Y. S. Malik (Eds.), *Protocols for the Diagnosis of Pig*

Viral Diseases (pp. 31–47). Springer US. https://doi.org/10.1007/978-1-0716-2043-4_3

Boehm, E., Kronig, I., Neher, R. A., Eckerle, I., Vetter, P., & Kaiser, L. (2021). Novel SARS-CoV-2 variants: The pandemics within the pandemic. *Clinical Microbiology and Infection*, *27*(8), 1109–1117. https://doi.org/10.1016/j.cmi.2021.05.022

Brümmer, L. E., Katzenschlager, S., Gaeddert, M., Erdmann, C., Schmitz, S., Bota, M., Grilli, M., Larmann, J., Weigand, M. A., Pollock, N. R., Macé, A., Carmona, S., Ongarello, S., Sacks, J. A., & Denkinger, C. M. (2021). Accuracy of novel antigen rapid diagnostics for SARS-CoV-2: A living systematic review and meta-analysis. *PLOS Medicine*, *18*(8), e1003735. https://doi.org/10.1371/journal.pmed.1003735

Cañamares, M. V., Garcia-Ramos, J. V., Gómez-Varga, J. D., Domingo, C., & Sanchez-Cortes, S. (2005). Comparative Study of the Morphology, Aggregation, Adherence to Glass, and Surface-Enhanced Raman Scattering Activity of Silver Nanoparticles Prepared by Chemical Reduction of Ag^{+} Using Citrate and Hydroxylamine. *Langmuir*, *21*(18), 8546–8553. https://doi.org/10.1021/la050030l

Choi, M., Kwok, S. J. J., & Yun, S. H. (2015). In Vivo Fluorescence Microscopy: Lessons From Observing Cell Behavior in Their Native Environment. *Physiology*, *30*(1), 40–49. https://doi.org/10.1152/physiol.00019.2014

Coarsey, C. T., Esiobu, N., Narayanan, R., Pavlovic, M., Shafiee, H., & Asghar, W. (2017). Strategies in Ebola virus disease (EVD) diagnostics at the point of care.

Critical Reviews in Microbiology, *43*(6), 779–798. https://doi.org/10.1080/1040841X.2017.1313814

Croudace, I. W., & Rothwell, R. G. (2015). *Future Developments and Innovations in High-Resolution Core Scanning | SpringerLink.* https://link.springer.com/chapter/10.1007/978-94-017-9849-5_27

Dahal, Y. R., & Schmit, J. D. (2018). Ion Specificity and Nonmonotonic Protein Solubility from Salt Entropy. *Biophysical Journal*, *114*(1), 76–87. https://doi.org/10.1016/j.bpj.2017.10.040

Ding, X., Clifton, D., Ji, N., Lovell, N. H., Bonato, P., Chen, W., Yu, X., Xue, Z., Xiang, T., Long, X., Xu, K., Jiang, X., Wang, Q., Yin, B., Feng, G., & Zhang, Y.-T. (2021). Wearable Sensing and Telehealth Technology with Potential Applications in the Coronavirus Pandemic. *IEEE Reviews in Biomedical Engineering*, *14*, 48–70. https://doi.org/10.1109/RBME.2020.2992838

Du, W. W., Zhang, C., Yang, W., Yong, T., Awan, F. M., & Yang, B. B. (2017). Identifying and Characterizing circRNA-Protein Interaction. *Theranostics*, *7*(17), 4183–4191. https://doi.org/10.7150/thno.21299

Elveborg, S., Monteil, V. M., & Mirazimi, A. (2022). Methods of Inactivation of Highly Pathogenic Viruses for Molecular, Serology or Vaccine Development Purposes. *Pathogens*, *11*(2), 271. https://doi.org/10.3390/pathogens11020271

Etienne, E. E., Nunna, B. B., Talukder, N., Wang, Y., & Lee, E. S. (2021). *COVID-19 Biomarkers and Advanced Sensing Technologies for Point-of-Care (POC) Diagnosis*. *7*. https://www.mdpi.com/2306-5354/8/7/98

FDA Advisory No.2021-2094 || List of COVID-19 Test Kits with FDA Special Certification and Performance Validation Conducted and/or Recommended by

the Research Institute for Tropical Medicine (RITM)—Food and Drug Administration. (n.d.). Retrieved June 5, 2023, from https://www.fda.gov.ph/fda-advisory-no-2021-2094-list-of-covid-19-test-kits-with-fda-special-certification-and-performance-validation-conducted-and-or-recommended-by-the-research-institute-for-tropical-medicine-ritm/

Fernandez-Montero, A., Argemi, J., Rodríguez, J. A., Ariño, A. H., & Moreno-Galarraga, L. (2021). Validation of a rapid antigen test as a screening tool for SARS-CoV-2 infection in asymptomatic populations. Sensitivity, specificity and predictive values. *EClinicalMedicine*, *37*, 100954. https://doi.org/10.1016/j.eclinm.2021.100954

Ferré, V. M., Peiffer-Smadja, N., Visseaux, B., Descamps, D., Ghosn, J., & Charpentier, C. (2022). Omicron SARS-CoV-2 variant: What we know and what we don't. *Anaesthesia, Critical Care & Pain Medicine*, *41*(1), 100998. https://doi.org/10.1016/j.accpm.2021.100998

Forinová, M., Pilipenco, A., Víšová, I., Kunčák, J., Lynn, N. S., Yudin, P., Dostálek, J., Hönig, V., Palus, M., Mašková, H., Dyčka, F., Štěrba, J., Vrabcová, M., Arnoštová, J., Spasovová, M., Tung, C.-P., Yang, A.-S., Dejneka, A., & Vaisocherová-Lísalová, H. (2021). Functionalized Terpolymer-Brush-Based Biointerface with Improved Antifouling Properties for Ultra-Sensitive Direct Detection of Virus in Crude Clinical Samples. *ACS Publications*, 1–4.

Furuya, H. (2020). *Prediction of Potential Respiratory Tract Infection from SARS-CoV-2 Through Hand-to-face Contact Transmission*.

Geddes, N. J., Paschinger, E. M., Furlong, D. N., Caruso, F., Hoffmann, C. L., & Rabolt, J. F. (1995). Surface chemical activation of quartz crystal microbalance

gold electrodes—Analysis by frequency changes, contact angle measurements and grazing angle FTIR. *Thin Solid Films*, *260*(2), 192–199. https://doi.org/10.1016/0040-6090(94)06474-1

GOV UK. (2023). *Chapter 1: Understanding the pathogen*. GOV.UK. https://www.gov.uk/government/publications/technical-report-on-the-covid-19-pandemic-in-the-uk/chapter-1-understanding-the-pathogen

Greenhawt, M., Abrams, E. M., Shaker, M., Chu, D. K., Khan, D., Akin, C., Alqurashi, W., Arkwright, P., Baldwin, J. L., Ben-Shoshan, M., Bernstein, J., Bingemann, T., Blumchen, K., Byrne, A., Bognanni, A., Campbell, D., Campbell, R., Chagla, Z., Chan, E. S., … Golden, D. B. K. (2021). The Risk of Allergic Reaction to SARS-CoV-2 Vaccines and Recommended Evaluation and Management: A Systematic Review, Meta-Analysis, GRADE Assessment, and International Consensus Approach. *The Journal of Allergy and Clinical Immunology: In Practice*, *9*(10), 3546–3567. https://doi.org/10.1016/j.jaip.2021.06.006

Günter, S. (1959). *Verwendung von Schwingquarzen zur Wägung dünner Schichten und zur Mikrowägung | SpringerLink*. https://link.springer.com/article/10.1007/BF01337937

Guzman-Santiago, G., Villanueva-Luna, A. E., Licea-Rodriguez, J., & Rocha-Mendoza, I. (2021). Tutorial for analyzing coherent Raman spectra excited with chirped femtosecond sources. *OSA Continuum*, *4*(2), 464. https://doi.org/10.1364/OSAC.412667

Habli, Z., Kobeissy, F., & Khraiche, M. L. (2022). Advances in point-of-care platforms for traumatic brain injury: Recent developments in diagnostics. *Reviews in the Neurosciences*, *33*(3), 327–345. https://doi.org/10.1515/revneuro-2021-0103

Habli, Z., Saleh, S., Zaraket, H., & Khraiche, M. L. (2019). *Frontiers | COVID-19 in-vitro Diagnostics: State-of-the-Art and Challenges for Rapid, Scalable, and High-Accuracy Screening*. https://www.frontiersin.org/articles/10.3389/fbioe.2020.605702/full

Harpaldas, H., Arumugam, S., Campillo Rodriguez, C., Kumar, B. A., Shi, V., & Sia, S. K. (2021). Point-of-care diagnostics: Recent developments in a pandemic age. *Lab on a Chip*, *21*(23), 4517–4548. https://doi.org/10.1039/D1LC00627D

Hodoroaba, V.-D. (2020). Chapter 4.4—Energy-dispersive X-ray spectroscopy (EDS). In V.-D. Hodoroaba, W. E. S. Unger, & A. G. Shard (Eds.), *Characterization of Nanoparticles* (pp. 397–417). Elsevier. https://doi.org/10.1016/B978-0-12-814182-3.00021-3

In Vitro Diagnostics EUAs—Antigen Diagnostic Tests for SARS-CoV-2 | FDA. (n.d.). Retrieved June 5, 2023, from https://www.fda.gov/medical-devices/covid-19-emergency-use-authorizations-medical-devices/in-vitro-diagnostics-euas-antigen-diagnostic-tests-sars-cov-2

Ishii, T., Yamada, M., Hirase, T., & Nagasaki, Y. (2005). New Synthesis of Heterobifunctional Poly(ethylene glycol) Possessing a Pyridyl Disulfide at One End and a Carboxylic Acid at the Other End. *Polymer Journal*, *37*(3), 221–228. https://doi.org/10.1295/polymj.37.221

Ji, T., Liu, Z., Wang, G., Guo, X., Akbar khan, S., Lai, C., Chen, H., Huang, S., Xia, S., Chen, B., Jia, H., Chen, Y., & Zhou, Q. (2020). Detection of COVID-19: A

review of the current literature and future perspectives. *Biosensors and Bioelectronics*, *166*, 112455. https://doi.org/10.1016/j.bios.2020.112455

Joshi, M., Bhattacharyya, A., & Ali, S. W. (2008). Characterization techniques for nanotechnology applications in textiles. *INDIAN J FIBRE TEXT. RES.*

Kannan, M. (2018). *Scanning Electron Microscopy: Principle, Components and Applications* (pp. 81–92).

Khalid, M. F., Selvam, K., Jeffry, A. J. N., Salmi, M. F., Najib, M. A., Norhayati, M. N., & Aziah, I. (2022). Performance of Rapid Antigen Tests for COVID-19 Diagnosis: A Systematic Review and Meta-Analysis. *Diagnostics*, *12*(1), 110. https://doi.org/10.3390/diagnostics12010110

Khraiche, M. L., Rogul, J., & Muthuswamy, J. (2019). Design and Development of Microscale Thickness Shear Mode (TSM) Resonators for Sensing Neuronal Adhesion. *Frontiers in Neuroscience*, *13*. https://www.frontiersin.org/articles/10.3389/fnins.2019.00518

Khraiche, M. L., Zhou, A., & Muthuswamy, J. (2003). Acoustic sensors for monitoring neuronal adhesion in real-time. *Proceedings of the 25th Annual International Conference of the IEEE Engineering in Medicine and Biology Society (IEEE Cat. No.03CH37439)*, *3*, 2186-2188 Vol.3. https://doi.org/10.1109/IEMBS.2003.1280175

Khraiche, M. L., Zhou, A., & Muthuswamy, J. (2005). Acoustic sensor for monitoring adhesion of Neuro-2A cells in real-time. *Journal of Neuroscience Methods*, *144*(1), 1–10. https://doi.org/10.1016/j.jneumeth.2004.09.029

Khraiche, M., & Muthuswamy, J. (2012). Multi-modal biochip for simultaneous, real-time measurement of adhesion and electrical activity of neurons in culture. *Lab on a Chip*, *12*(16), 2930–2941. https://doi.org/10.1039/C2LC40190H

Labs. (2020, February 11). Centers for Disease Control and Prevention. https://www.cdc.gov/coronavirus/2019-ncov/lab/resources/antigen-tests-guidelines.html

Lei, C., Yang, J., Hu, J., & Sun, X. (2021). On the Calculation of TCID50 for Quantitation of Virus Infectivity. *Virologica Sinica*, *36*(1), 141. https://doi.org/10.1007/s12250-020-00230-5

Lewis, S. M., Naik, S. H., Asselin--Labat, M.-L., Nguyen, Q., Berthelet, J., Tan, X., Wimmer, V. C., Merino, D., Rogers, K. L., & Naik, S. H. (2021). *Spatial omics and multiplexed imaging to explore cancer biology | Nature Methods*. https://www.nature.com/articles/s41592-021-01203-6

Lichtman, J. W., & Conchello, J.-A. (2005). Fluorescence microscopy. *Nature Methods*, *2*(12), 910–919. https://doi.org/10.1038/nmeth817

Luitjohan, K. (2018). *Boron Segregation and its Effects in Advanced High Strength Steel*.

Maiti, N. C., Apetri, M. M., Zagorski, M. G., Carey, P. R., & Anderson, V. E. (2004). Raman Spectroscopic Characterization of Secondary Structure in Natively Unfolded Proteins: α-Synuclein. *Journal of the American Chemical Society*, *126*(8), 2399–2408. https://doi.org/10.1021/ja0356176

MAN0011309_NHS_SulfoNHS_UG.pdf. (n.d.). Retrieved May 16, 2023, from https://tools.thermofisher.com/content/sfs/manuals/MAN0011309_NHS_SulfoNHS_UG.pdf

Manjate, N. J., Sitoe, N., Sambo, J., Guimarães, E., Canana, N., Chilaúle, J., Viegas, S., Nguenha, N., Jani, I., & Russo, G. (2023). Testing for SARS-CoV-2 in resource-limited settings: A cost analysis study of diagnostic tests using different Ag-RDTs and RT-PCR technologies in Mozambique. *PLOS Global Public Health*, *3*(6), e0001999. https://doi.org/10.1371/journal.pgph.0001999

Marquet, P., Rappaz, B., Magistretti, P. J., Cuche, E., Emery, Y., Colomb, T., & Depeursinge, C. (2005). Digital holographic microscopy: A noninvasive contrast imaging technique allowing quantitative visualization of living cells with subwavelength axial accuracy. *Optics Letters*, *30*(5), 468. https://doi.org/10.1364/OL.30.000468

Michel, R., Pasche, S., Textor, M., & Castner, D. G. (2005). The Influence of PEG Architecture on Protein Adsorption and Conformation. *Langmuir : The ACS Journal of Surfaces and Colloids*, *21*(26), 12327–12332. https://doi.org/10.1021/la051726h

Muthuswamy, J., Sridharan, A., & KHRAICHE, M. (2022). *Sensor for detecting biomarkers in a fluid sample and methods of use* (World Intellectual Property Organization Patent WO2022256741A1). https://patents.google.com/patent/WO2022256741A1/en?q=(Khraiche+QCM)&oq=Khraiche+QCM

Narita, F., Wang, Z., Kurita, H., Li, Z., Shi, Y., Jia, Y., & Soutis, C. (2021). A Review of Piezoelectric and Magnetostrictive Biosensor Materials for Detection of COVID-19 and Other Viruses. *Advanced Materials*, *33*(1), 2005448. https://doi.org/10.1002/adma.202005448

OPENQCM Q-1 USER MANUAL Pdf Download | ManualsLib. (n.d.). Retrieved June 3, 2023, from https://www.manualslib.com/manual/1512745/Openqcm-Q-1.html

OPENQCM Q-1 WITH DISSIPATION MODULE. (n.d.). OpenQCM Store. Retrieved June 3, 2023, from https://store.openqcm.com/openqcm-q-1-with-dissipation-module/

OpenQCM_Wi2-userguide-v2.0.pdf. (n.d.). Retrieved June 3, 2023, from https://openqcm.com/shared/wi2/openQCM_Wi2-userguide-v2.0.pdf

Panpradist, N., Wang, Q., Ruth, P. S., Kotnik, J. H., Oreskovic, A. K., Miller, A., Stewart, S. W. A., Vrana, J., Han, P. D., Beck, I. A., Starita, L. M., Frenkel, L. M., & Lutz, B. R. (2021). Simpler and faster Covid-19 testing: Strategies to streamline SARS-CoV-2 molecular assays. *EBioMedicine*, *64*, 103236. https://doi.org/10.1016/j.ebiom.2021.103236

Parupudi, T., Panchagnula, N., Muthukumar, S., & Prasad, S. (n.d.). Evidence-based point-of-care technology development during the COVID-19 pandemic. *Biotechniques*, 10.2144/btn-2020–0096. https://doi.org/10.2144/btn-2020-0096

Patil, R. M., Deshpande, P. P., Aalhate, M., Gananadhamu, S., & Singh, P. K. (2022). An Update on Sophisticated and Advanced Analytical Tools for Surface Characterization of Nanoparticles. *Surfaces and Interfaces*, *33*, 102165. https://doi.org/10.1016/j.surfin.2022.102165

Perumal, N., Jain, R. K., Shrivastava, R., Lalwani, J., & Chaurasia, D. (2020). Stability of SARS-CoV-2 RNA in Viral Lysis Buffer Stored at Different Temperatures. *Journal of Laboratory Physicians*, *12*(4), 268–270. https://doi.org/10.1055/s-0040-1722551

Peterson, S. W., Lidder, R., Daigle, J., Wonitowy, Q., Dueck, C., Nagasawa, A., Mulvey, M. R., & Mangat, C. S. (2022). RT-qPCR detection of SARS-CoV-2 mutations S 69–70 del, S N501Y and N D3L associated with variants of concern in Canadian wastewater samples. *The Science of the Total Environment*, *810*, 151283. https://doi.org/10.1016/j.scitotenv.2021.151283

Peto, T., Affron, D., Afrough, B., Agasu, A., Ainsworth, M., Allanson, A., Allen, K., Allen, C., Archer, L., Ashbridge, N., Aurfan, I., Avery, M., Badenoch, E., Bagga, P., Balaji, R., Baldwin, E., Barraclough, S., Beane, C., Bell, J., … Zinyama, R. (2021). COVID-19: Rapid antigen detection for SARS-CoV-2 by lateral flow assay: A national systematic evaluation of sensitivity and specificity for mass-testing. *EClinicalMedicine*, *36*, 100924. https://doi.org/10.1016/j.eclinm.2021.100924

Po-Chiao, L., Po-Hung Chou, S.-H. C., & Hsin-Kai Liao, K.-Y. W. (2006). *Ethylene Glycol-Protected Magnetic Nanoparticles for a Multiplexed Immunoassay in Human Plasma—Lin—2006—Small—Wiley Online Library*. https://onlinelibrary.wiley.com/doi/epdf/10.1002/smll.200500387

Pollock, N. R., Jacobs, J. R., Tran, K., & Cranston, A. E. (2021). *Performance and Implementation Evaluation of the Abbott BinaxNOW Rapid Antigen Test in a High-Throughput Drive-Through Community Testing Site in Massachusetts*. https://doi.org/10.1128/jcm.00083-21

Polymerase-Chain-Reaction-Protocol.pdf. (n.d.). Retrieved June 21, 2023, from https://asm.org/ASM/media/Protocol-Images/Polymerase-Chain-Reaction-Protocol.pdf?ext=.pdf

Prime, K. L., & Whitesides, G. M. (1991). Self-Assembled Organic Monolayers: Model Systems for Studying Adsorption of Proteins at Surfaces. *Science, New Series*, *252*(5009), 1164–1167.

Raman correlations.pdf. (n.d.). Retrieved June 5, 2023, from https://www.chem.uci.edu/~dmitryf/manuals/Raman%20correlations.pdf

Rasmi, Y., Li, X., Khan, J., Ozer, T., & Choi, J. R. (2021). Emerging point-of-care biosensors for rapid diagnosis of COVID-19: Current progress, challenges, and future prospects. *Analytical and Bioanalytical Chemistry*, *413*(16), 4137–4159. https://doi.org/10.1007/s00216-021-03377-6

Raziq, A., Kidakova, A., Boroznjak, R., Reut, J., Öpik, A., & Syritski, V. (2021). Development of a portable MIP-based electrochemical sensor for detection of SARS-CoV-2 antigen. *Biosensors & Bioelectronics*, *178*, 113029. https://doi.org/10.1016/j.bios.2021.113029

Reflection DHM[r]—LyncéeTec. (n.d.). Retrieved June 3, 2023, from https://www.lynceetec.com/reflection-dhm/

Renate Petry Dr., M. S. Dr., & Popp, J. (2002). *Raman Spectroscopy—A Prospective Tool in the Life Sciences—Petry—2003—ChemPhysChem—Wiley Online Library*. https://chemistry-europe.onlinelibrary.wiley.com/doi/abs/10.1002/cphc.200390004

Rostron, P., & Gerber, D. (2016). Raman Spectroscopy, a review. *International Journal of Engineering and Technical Research*, *6*, 50–64.

SARS-CoV-2 Intact Virus Purification—LB. (n.d.). Retrieved June 3, 2023, from https://www.thermofisher.com/sa/en/home/life-science/cell-analysis/exosomes/manual-automated-sars-cov-2-enrichment-products.html

Sebestyén, Z., Nagy, P., Horváth, G., György Vámosi, Debets, R., Gratama, J. W., Alexander, D. R., & Szöllősi, J. (2002). Long wavelength fluorophores and cell-by-cell correction for autofluorescence significantly improves the accuracy of flow cytometric energy transfer measurements on a dual-laser benchtop flow cytometer. *Cytometry*, *48*(3), 124–135. https://doi.org/10.1002/cyto.10121

Shafie, M. H., Antony Dass, M., Ahmad Shaberi, H. S., & Zafarina, Z. (2023). Screening and confirmation tests for SARS-CoV-2: Benefits and drawbacks. *Beni-Suef University Journal of Basic and Applied Sciences*, *12*(1), 6. https://doi.org/10.1186/s43088-023-00342-3

Shoaib, M. H., Ahmed, F. R., Sikandar, M., Yousuf, R. I., & Saleem, M. T. (2021). A Journey From SARS-CoV-2 to COVID-19 and Beyond: A Comprehensive Insight of Epidemiology, Diagnosis, Pathogenesis, and Overview of the Progress into Its Therapeutic Management. *Frontiers in Pharmacology*, *12*, 576448. https://doi.org/10.3389/fphar.2021.576448

Siddiqui, Z. K., Chaudhary, M., Robinson, M. L., McCall, A. B., Peralta, R., Esteve, R., Callahan, C. W., Manabe, Y. C., Campbell, J. D., Johnson, J. K., Elhabashy, M., Kantsiper, M., & Ficke, J. R. (2021). Implementation and Accuracy of BinaxNOW Rapid Antigen COVID-19 Test in Asymptomatic and Symptomatic Populations in a High-Volume Self-Referred Testing Site. *Microbiology Spectrum*, *9*(3), e01008-21. https://doi.org/10.1128/Spectrum.01008-21

Singh, V., Garg, S., Raj, N., Lukose, A., Jamwal, D., Perween, R., Dhyani, S., Parray, H. A., Sharma, C., & Kumar, R. (2022). Protocol for High Throughput Screening of Antibody Phage Libraries. *Bio-Protocol*, *12*(12), e4450. https://doi.org/10.21769/BioProtoc.4450

Smith, R. D., Johnson, J. K., Clay, C., Girio-Herrera, L., Stevens, D., Abraham, M., Zimand, P., Ahlman, M., Gimigliano, S., Zhao, R., Hildenbrand, C., Barrueto, F., & Leekha, S. (2021). Clinical evaluation of Sofia Rapid Antigen Assay for detection of severe acute respiratory syndrome coronavirus 2 (SARS-CoV-2) among emergency department to hospital admissions. *Infection Control and Hospital Epidemiology*, 1–6. https://doi.org/10.1017/ice.2021.281

Srivatsan Kidambi, Christina Chan, and, & Lee*, I. (2004). Selective Depositions on Polyelectrolyte Multilayers: Self-Assembled Monolayers of m-dPEG Acid as Molecular Template. *ACS Publications*. https://doi.org/10.1021/ja039359o

Tarhini, A., Alchamaa, M. W., Khraiche, M., Kazan, M., & Tehrani-Bagha, A. (2022). The effect of temperature on the electrical and thermal conductivity of graphene-based polymer composite films. *Journal of Applied Polymer Science*, *139*(14), 51896. https://doi.org/10.1002/app.51896

Thomas, E., Delabat, S., Carattini, Y. L., & Andrews, D. M. (2021). SARS-CoV-2 and Variant Diagnostic Testing Approaches in the United States. *Viruses*, *13*(12), Article 12. https://doi.org/10.3390/v13122492

Titus, D., James Jebaseelan Samuel, E., & Roopan, S. M. (2019). Chapter 12—Nanoparticle characterization techniques. In A. K. Shukla & S. Iravani (Eds.), *Green Synthesis, Characterization and Applications of Nanoparticles* (pp. 303–319). Elsevier. https://doi.org/10.1016/B978-0-08-102579-6.00012-5

Torretta, S., Zuccotti, G., Cristofaro, V., Ettori, J., Solimeno, L., Battilocchi, L., D'Onghia, A., Bonsembiante, A., Pignataro, L., Marchisio, P., & Capaccio, P. (2021). Diagnosis of SARS-CoV-2 by RT-PCR Using Different Sample

Sources: Review of the Literature. *Ear, Nose, & Throat Journal*, *100*(2 Suppl), 131S-138S. https://doi.org/10.1177/0145561320953231

Understanding cycle threshold (Ct) in SARS-CoV-2 RT-PCR. (2020).

Verma, A., & Rotello, V. M. (2005). *Surface recognition of biomacromolecules using nanoparticle receptors—Chemical Communications (RSC Publishing)*. https://pubs.rsc.org/en/content/articlelanding/2005/cc/b410889b/unauth

Verna, R., Alallon, W., Murakami, M., Hayward, C. P. M., Harrath, A. H., Alwasel, S. H., Sumita, N. M., Alatas, O., Fedeli, V., Sharma, P., Fuso, A., Capuano, D. M., Capalbo, M., Angeloni, A., & Bizzarri, M. (2021). Analytical Performance of COVID-19 Detection Methods (RT-PCR): Scientific and Societal Concerns. *Life*, *11*(7), 660. https://doi.org/10.3390/life11070660

Wang, Q., Zhang, Y., Wu, L., Niu, S., Song, C., Zhang, Z., Lu, G., Qiao, C., Hu, Y., Yuen, K.-Y., Wang, Q., Zhou, H., Yan, J., & Qi, J. (2020). Structural and Functional Basis of SARS-CoV-2 Entry by Using Human ACE2. *Cell*, *181*(4), 894-904.e9. https://doi.org/10.1016/j.cell.2020.03.045

Wang, W., Wei, Q.-Q., Wang, J., Wang, B.-C., Zhang, S., & Yuan, Z. (2013). Role of thiol-containing polyethylene glycol (thiol-PEG) in the modification process of gold nanoparticles (AuNPs): Stabilizer or coagulant? *Journal of Colloid and Interface Science*, *404*, 223–229. https://doi.org/10.1016/j.jcis.2013.04.020

Webster, S., Smith, D. A., & Batchelder, D. N. (1998). Raman microscopy using a scanning near-field optical probe. *Vibrational Spectroscopy*, *18*(1), 51–59. https://doi.org/10.1016/S0924-2031(98)00037-X

WHO-2019-nCoV-Antigen-Detection-2021.1-eng.pdf. (n.d.). Retrieved June 3, 2023, from https://apps.who.int/iris/bitstream/handle/10665/345948/WHO-2019-nCoV-Antigen-Detection-2021.1-eng.pdf?sequence=1&isAllowed=y

Xue, Y., Li, X., Li, H., & Zhang, W. (2014). Quantifying thiol–gold interactions towards the efficient strength control. *Nature Communications*, *5*(1), Article 1. https://doi.org/10.1038/ncomms5348

Ye, Q., Lu, D., Zhang, T., Mao, J., & Shang, S. (2022). *Recent advances and clinical application in point-of-care testing of SARS-CoV-2—Ye—2022—Journal of Medical Virology—Wiley Online Library*. *94*(5). https://onlinelibrary.wiley.com/doi/epdf/10.1002/jmv.27617

Zheng, M., Davidson, F., & Huang, X. (2003). *Ethylene Glycol Monolayer Protected Nanoparticles for Eliminating Nonspecific Binding with Biological Molecules | Journal of the American Chemical Society*. https://pubs.acs.org/doi/pdf/10.1021/ja0350278